Nanoscale

REVIEW

View Article Online
View Journal | View Issue

Cite this: *Nanoscale*, 2021, **13**, 9908

A review on vertical and lateral heterostructures of semiconducting 2D-MoS_2 with other 2D materials: a feasible perspective for energy conversion

Gayatri Swain, Sabiha Sultana and Kulamani Parida *

Fossil fuels as a double-edged sword are essential to daily life. However, the depletion of fossil fuel reservoirs has increased the search for alternative renewable energy sources to procure a more sustainable society. Accordingly, energy production through water splitting, CO_2 reduction and N_2 reduction *via* photocatalytic and electrocatalytic pathways is being contemplated as a greener methodology with zero environmental pollution. Owing to their atomic-level thickness, two-dimensional (2D) semiconductor catalysts have triggered the reawakening of interest in the field of energy and environmental applications. Among them, following the unconventional properties of graphene, 2D MoS_2 has been widely investigated due to its outstanding optical and electronic properties. However, the photo/electrocatalytic performance of 2D-MoS_2 is still unsatisfactory due to its low charge carrier density. Recently, the development of 2D/2D heterojunctions has evoked interdisciplinary research fascination in the scientific community, which can mitigate the shortcomings associated with 2D-MoS_2. Following the recent research trends, the present review covers the recent findings and key aspects on the synthetic methods, fundamental properties and practical applications of semiconducting 2D-MoS_2 and its heterostructures with other 2D materials such as g-C_3N_4, graphene, CdS, TiO_2, MXene, black phosphorous, and boron nitride. Besides, this review details the viable application of these materials in the area of hydrogen energy production *via* the H_2O splitting reaction, N_2 fixation to NH_3 formation and CO_2 reduction to different value-added hydrocarbons and alcohol products through both photocatalysis and electrocatalysis. The crucial role of the interface together with the charge separation principle between two individual 2D structures towards achieving satisfactory activity for various applications is presented. Overall, the current studies provide a snapshot of the recent breakthroughs in the development of various 2D/2D-based catalysts in the field of energy production, delivering opportunities for future research.

Received 10th February 2021,
Accepted 10th May 2021

DOI: 10.1039/d1nr00931a

rsc.li/nanoscale

1. Introduction

The exacerbation of global warming, the energy crisis and environmental pollution in the 21st century is highly related to the depletion of fossil fuels, which is becoming one of the biggest challenges with the rapid industrial and population growth.[1–3] Additionally, the consumption of fossil fuels significantly contributes to the greenhouse effect by emitting CO_2.[1,4] Therefore, to alleviate these problems and achieve a greener world, photocatalysis and electrocatalysis have emerged as the Holy Grails of green and sustainable technology towards the conversion of solar energy and electric energy into chemical energy through water splitting, N_2 reduction, and CO_2 reduction.[5–8] However, for the efficient utilization of solar energy together with the extensive use of electrocatalysis, the choice of catalyst is essential.[9–11]

In recent decades, nanostructured materials have become one of the main influencers in the field of photo/electrocatalysis mainly due to their large surface area, quantum confinement effect and dominant interfacial phenomena.[12–15] In contrast to conventional 0D and 1D catalysts with restricted dimensions, catalysts based on 2D materials have attracted a great deal of attention in the field of catalysis due to their remarkable physical and chemical properties together with controllable optical and electronic properties. Due to their planar structure and abundant exposed surface atoms, 2D materials provide a large number of active sites for photo/electrocatalytic reactions. In addition, they possess sufficient space for the integration of various catalysts, thus enhancing the flexibility of catalytic activity and formation of new active sites.[9,16–20] The design of 2D materials has been inspired by one particular two-dimensional material, graphene, which is considered the tip of the iceberg, where the first real and

Centre for Nanoscience and Nanotechnology, Siksha 'O' Anusandhan (Deemed to be University), Jagamohan Nagar, Jagamara, Bhubaneswar-751030, Odisha, India. E-mail: kulamaniparida@soa.ac.in, paridakulamani@yahoo.com

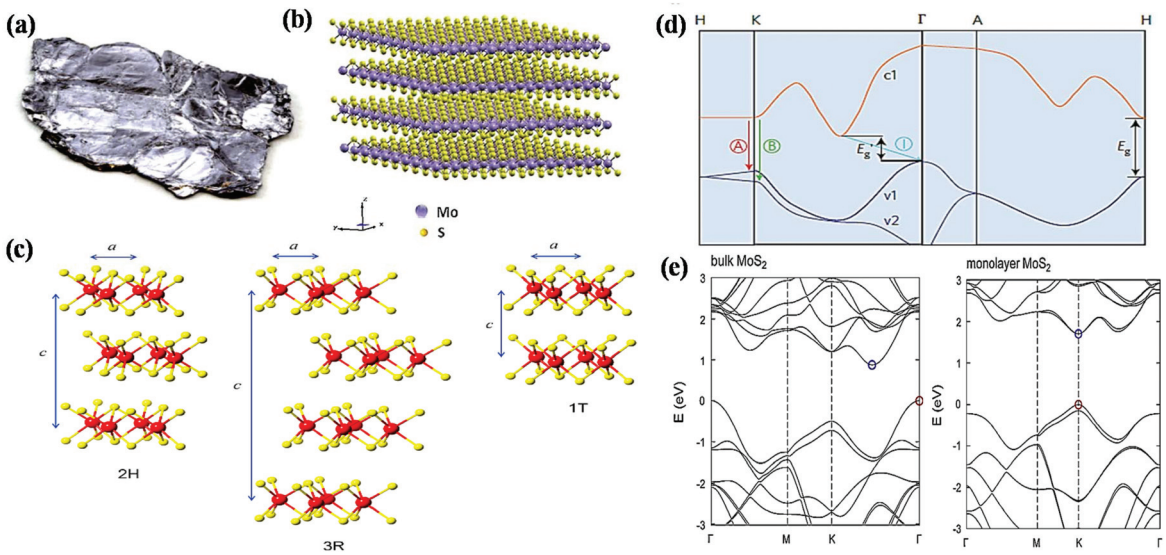

Fig. 1 (a) Picture of bulk MoS_2 crystal. Reproduced from ref. 29. (b) Three-dimensional model of the crystal structure of MoS_2. Reproduced from ref. 33. (c) Schematic illustration of the various crystal structure polytypes: 2H, 3R and 1T. Reproduced from ref. 36. (d) Typical band structure of MoS_2, where c1 represents the conduction band and v1 and v2 the valence bands. A and B show the direct band-gap transitions and I stands for the indirect band-gap transition. E_g and E'_g represent the direct and indirect band-gap for the monolayer and bulk, respectively. Reproduced from ref. 28. (e) Illustration of the electronic band structures of bulk and monolayer MoS_2. Reproduced from ref. 29.

thermodynamic stable single 2D sheet of graphite was reported by Novoselov and Geim in 2004.[19,21] After the first seminal isolation of graphite, graphene and its derivatives have been employed as significant catalysts in a variety of catalytic applications, triggering the search for other 'beyond graphene' materials. Therefore, a wide range of 2D materials, especially those similar to graphene have been applied in a wide range of fields such as photocatalysis, electrocatalysis, energy storage, and biosensors. To date, for instance, numerous 2D materials (single and 2D-based composites) such as hexagonal boron nitride, graphitic carbon nitride, transition metal chalcogenides, MXenes, layered double hydroxides, and boron phosphides have been developed.[22–25]

However, the development of the research interest in the photo/electrocatalysis field has diverted attention toward transition metal dichalcogenides especially 2D-MoS_2, a chalcogenide derivative of molybdenum and a rising star in the graphene analogous family.[26–29] MoS_2 is an inorganic silvery black solid (Fig. 1a), which mainly occurs in nature as the mineral molybdenite, the principal ore of Mo.[29–31] As depicted in Fig. 1b, the

Gayatri Swain

Dr Gayatri Swain completed her Master of Science (M.Sc.) in Chemistry from Berhampur University, Odisha, India in 2014 and then completed her PhD in 2020 at Siksha 'O' Anusandhan (Deemed to be University), Bhubaneswar, India under the supervision of Prof. Kulamani Parida. At present she is working as a Research Associate at the Centre for Nanoscience and Nanotechnology, Siksha 'O' Anusandhan (Deemed to be University), Bhubaneswar, India. She is the author of 10 international journal articles with one book chapter. Her current research interests are mainly focused on the synthesis of two-dimensional transition metal dichalcogenides and their application towards energy and environmental benefits.

Sabiha Sultana

Dr Sabiha Sultana received her Bachelor's Degree from Utkal University, Bhubaneswar in 2012 and M.Sc. Chemistry from Ravenshaw University, Cuttack in 2014. Then, she joined as a PhD student under the supervision of Prof. K. M. Parida the Centre for Nanoscience and Nanotechnology, ITER, SOA Deemed to be University and recently completed her PhD Degree. Her research area focuses on the development of nanostructured materials including metal oxides, metal sulphides, and phosphides and their application towards water splitting, N_2, CO_2 reduction, and pollutant abatement. She has published 12 research articles in various international journals.

structural units of MoS_2 arrange themselves in a way that the transition-metal atom exhibits six-fold coordination and is covalently bonded in between two chalcogen atomic layers in an S–Mo–S fashion, forming a sandwich layer, and each sandwich layer connects to the other by means of weak interlayer van der Waals forces.[31–33] According to the atomic co-ordination of the surrounding S atoms with respect to the central Mo atom and stacking sequence of each MoS_2 layer, the crystal structure of MoS_2 has been classified into 3 types of polymorphs, among which two configurations occur naturally (2H and 3R), whereas the other polytype (1T) is synthetically available (Fig. 1c). The terms H, R and T represent hexagonal, rhombohedral and tetragonal, and hence their naming depends on their symmetry. The 2H and 3R phase of MoS_2 is semiconducting, while the 1T phase of MoS_2 is metallic.[31,34–36] In particular, the crystal structure of 2H-MoS_2 mainly consists of an Mo central atom surrounded by 6 sulfide (S^{2-}) ligands, which occupy a trigonal prismatic coordination sphere, where each sulfur center is connected to 3 Mo centres to form a pyramidal structure. Accordingly, several trigonal prisms are intertwined to construct a layered structure in which one layer of Mo atoms is sandwiched between two sheets of S atoms, resulting in the formation of a hexagonal sheet-like structure of MoS_2.[37] The basic difference between the two naturally occurring forms of MoS_2, *i.e.*, 2H-MoS_2 and 3R-MoS_2, is the stacking order of the S–Mo–S sheets in their unit cell. Moreover, the stacking order of 2H-MoS_2 is AbA BaB, *i.e.*, 2 S–Mo–S units per primitive unit cell with hexagonal symmetry in the space group *P*63/*mmc*, whereas 3R-MoS_2 exhibits rhombohedral symmetry with the stacking order of AbA CaC BcB, *i.e.*, 3 S–Mo–S units per unit cell in the space group *R*3*m*. In the stacking order model, the upper and lower cases represent the relative position of the S and Mo atoms, respectively. 1T-MoS_2 is a one-layer crystal cell that has tetragonal polytype symmetry, in which the Mo atoms are octahedrally coordinated by six S atoms in the AbC AbC... stacking order.[34,38,39] Most experimental studies reveal that 1T-MoS_2 is a metastable structure that can be completely transformed to 2H-MoS_2 upon annealing over a particular temperature range.[34,40] However, according to the current research, the most widely studied phase of MoS_2 is semiconducting, *i.e.*, 2H-MoS_2, which is attributed to its excellent stability, unique structural arrangement, suitable band gap for various catalytic reactions, *etc*. Therefore, in the current review, we extensively focus on two-dimensional semiconducting 2H-MoS_2.

The electronic structure of semiconducting 2H-MoS_2 includes its band structure and change in band structure, which are controlled by the number of layers and change in hybridization between the d orbital and P_z orbital of Mo and S, respectively.[31,37] The band structure and change in band gap with respect to layer number is illustrated in Fig. 1d and e, respectively.[28,29] According to the literature, bulk MoS_2 possess an indirect bandgap with an energy gap of 1.2 eV, while its bandgap becomes direct for few or single-layer MoS_2 with an energy gap of about 1.9 eV, which varies with the tuning of the layer of MoS_2.[39] From an experimental view, it has been found that few-layer MoS_2 exhibits four weak humped absorption peaks in the wavelength range of 250–700 nm. Among them, the characteristic peaks observed in the range of 250–450 nm are mainly attributed to the higher excited states or bands, whereas the doublet located in the range of 600–700 nm originates from the direct excitonic transition occurring at the Brillouin zone *K* point between the VBM and CBM due to the spin–orbit dissociation of transition at that point.[37,39] Moreover, the change in bandgap energy, *i.e.*, from indirect to direct with a change in layer number also greatly affects the photoluminescence spectrum (PL), absorption spectrum and photoconductivity of MoS_2. It has been shown that the intensity of the PL spectrum is inversely proportional to the layer number, where few-layer or thin layer MoS_2 exhibits the strongest PL intensity with a large quantum efficiency. Experimentally, the two excitonic peaks in the PL spectrum of MoS_2 are observed at ~1.9 eV and ~2.08 eV at the *K* point, which may be due to the spin–orbit band splitting near the valence band. It has been shown that monolayer MoS_2 exhibits a main peak at 1.9 eV due to its direct gap luminescence, whereas few layer MoS_2 show additional peaks together with the main peak originating from the direct gap hot luminescence and indirect-gap luminescence.[37,41] Further, the valence band is derived from the overlapping of the filled d_{z^2} orbital of Mo-4d with the filled sp orbital of the S atoms. Conversely, the conduction band is determined by the degenerate Mo-3d orbitals, *i.e.*, $d_{x^2-y^2}$, d_{z^2}, which overlap with the empty antibonding orbitals of the S atom.[39]

MoS_2 has two distinctive orientations in its structure, namely basal planes with surface inertness and edge planes with high surface energy, and each orientation is terminated by chalcogen atoms. The electrical conductivity along the layer is very high, while it is low across the van der Waals gaps

Kulamani Parida

Prof. Kulamani Parida currently works as a Distinguished Professor in Chemistry and Director of the Centre for Nanoscience and Nanotechnology, Siksha O Anusandhan, Deemed to be University, Odisha, India. He received his PhD degree and DSc from Utkal University in 1981 and 2002, respectively, on solid-state chemistry and catalysis. In 1981, he joined the Regional Research Laboratory, Bhubaneswar and worked there for 37 years and retired as a Chief Scientist and Head of Colloids and Materials Chemistry Department. His area of interest covers extensive research on narrow and wide band gap semiconductors, metal oxides, metal phosphides, metal sulphides, metal carbides and nitrides exhibiting efficient electro and photocatalytic water splitting and pollutant degradation activity.

between the layers, which indicates that compared to the basal planes, the edge sites exhibit the fast transportation of electrons.[30,42,43] Hence, in recent decades, ultrathin MoS_2 has been demonstrated to be an excellent electrocatalyst towards the hydrogen evolution reaction.[43,44] Moreover, its properties such as high chemical stability, superior charge carrier mobility, good surface to volume ratio and visible light absorbing property makes it an ideal candidate catalyst for photocatalytic reactions.[39,45–48] More importantly, MoS_2 is considered to be a good substitute for noble metals (such as Pt, Rh, Ru, and Pd) and a low-cost catalyst for both photocatalytic and electrocatalytic reactions. Although the absorbance edge of MoS_2 extends from the UV-Vis to IR region, which seems ideal as a solar light harvester, single MoS_2 has negligible photocatalytic activity towards energy production. This poor photocatalytic activity is attributed to the insufficient charge separation and low conductivity power between the adjacent S–Mo–S layers, which lead to poor charge mobility.[49–51] Accordingly, the abovementioned difficulties have been overcome using various techniques such as sulfur edge activation, phase transition, heteroatom doping, and fabrication of heterojunction or composite with other materials. Among the various strategies, many studies reveal that the formation of hierarchical composites of MoS_2 with other 2D-layered materials such as 2D-metal, 2D-semiconductor and 2D-insulator provides abundant active sites and immense surface area, which greatly enhance the effectiveness of the reaction.[52–55]

Although several excellent reviews summarizing the advantages, synthetic techniques, different physicochemical properties and potential application of 2D/2D heterostructures have been published, there is no comprehensive review on 2D-MoS_2-based 2D/2D heterostructure materials. Therefore, herein we present an in-depth overview on the recent progress in the development of 2D MoS_2-based 2D/2D heterostructure catalysts towards energy production. It includes various emerging strategies and fundamental aspects on the recent development of 2D MoS_2 and its synthetic methods, photocatalytic and electrocatalytic activity, and on-demand modification of its photo/electrocatalytic activity *via* the introduction of other 2D materials. Subsequently, the various applications summarized in this review mainly include photocatalytic and electrocatalytic hydrogen evolution, CO_2 reduction and nitrogen reduction. Therefore, in this review, we offer the latest progress in the 2D-MoS_2 based 2D/2D heterostructure catalyst towards energy benefits along with various catalytic mechanisms.

2. Basis for 2D/2D heterostructures and types of interfacial coupling

2D/2D material-based composites possess a solid structure, which provides a large intimate contact interface between the individual materials, resulting in excellent photo/electro stability in the catalyst.[17,56,57] Moreover, in 2D/2D heterostructures, interfacial charge migration and separation is more efficient due to the formation of a large contact area, which provides trapping channels by the large lateral size of the combined 2D materials. In the case of photocatalytic reactions, besides the formation of a high surface contact, the type and nature of the intimate interface are crucial parameters to accelerate charge carrier migration, thus suppressing the formation of photogenerated electron–hole pairs.[58–63]

Generally, there are two directions, *i.e.*, vertical and lateral, for the engineering of 2D/2D heterostructures with a different contact interface (Scheme 1). In the lateral direction, 2D/2D heterostructures are successfully achieved through the cross-section interface contact *via* the epitaxial growth method, which can be considered to be both a patterned and paralleled contact surface. In contrast, 2D/2D heterostructures in the vertical direction are realized *via* face-to-face contact and acquired by stacking two or multiple monolayer sheets of different nanomaterials. This method proceeds through atomic precision by regulating the relative orientation between the single 2D components.[54,64–67] However, Wang *et al.* demonstrated a

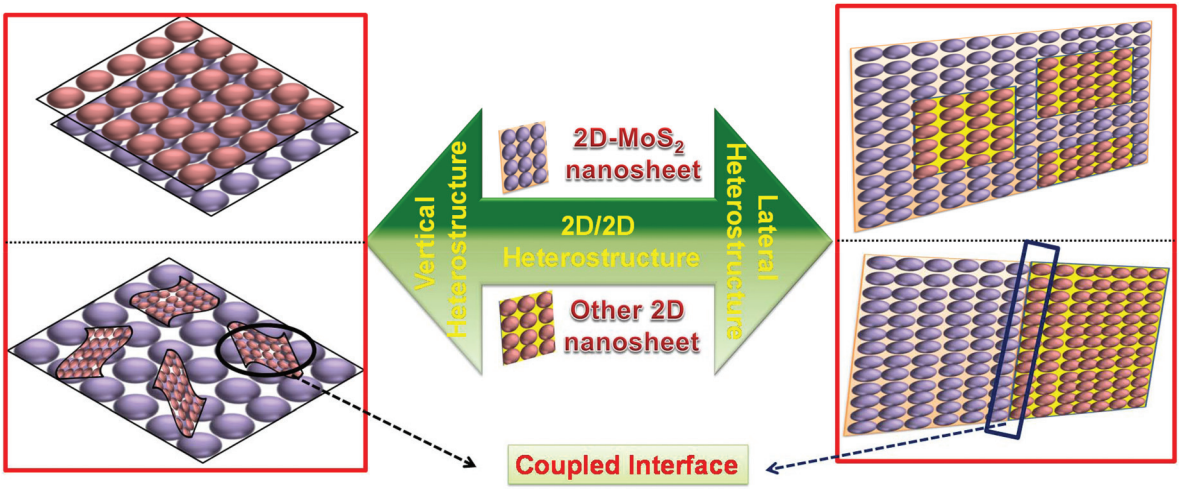

Scheme 1 Schematic representation of the 2D/2D vertical (left) and lateral (right) heterostructures with a coupled interface.

high-quality MoS_2 : h-BN vertical heterostructure *via* a stacking process of two 2D crystals on top of each other, which provided better interlayer interaction at the interface.[68] Behranginia *et al.* synthesized a lateral MoS_2/graphene 2D/2D heterostructure, which provided a high quality lateral interface between MoS_2 and graphene.[69] Moreover, Yoo and coworkers reported both a lateral and vertical heteroepitaxy interface between WS_2 and MoS_2 monolayers by carefully controlling the contamination and defects in each 2D crystal. The as fabricated lateral and vertical 2D/2D heterostructure provides a building block for an abrupt and patterned junction in 2D materials.[70]

In terms of bonding, 2D/2D heterostructure including covalently bonded and van der Waals interacted heterostructures fall in a category. Considering that the layers of 2D materials are connected by *via* both covalent bonding (strong) and van der Waals forces (weak), during the formation of a well-defined 2D/2D heterostructure with a covalent bonding interface, it is necessary to maintain both the lattice constant matching and valence matching on each side of the interface. However, in terms of van der Waals integration, although the van der Waals forces between the layers are weak, it does not rely on either lattice matching or valence matching, but facilitates the formation of a broader heterostructure phase space, which mediates various catalytic reaction across the interface.[64,66,71,72] Thus, it has been concluded that to successfully construct a 2D/2D interface, it is necessary to achieve strong interfacial bonding by optimizing the interaction forces in the composite structure. Generally, in the case of MoS_2-based 2D/2D heterostructures, the strength of the interfacial bonding is regulated through various factors such as chemical bonding, Coulomb force, van der Waals force, and electrostatic interaction. For example, Yu and his group designed an MoS_2/graphene 2D/2D van der Waals heterostructure with face-to-face contact through the alternating arrangement of monolayer MoS_2 nanosheets and graphene. It was observed that the obtained coupled interface improved the electronic conductivity of the heterostructure material by providing more edge active sites and defects.[73] Further, Shi *et al.* employed a simple electrostatic self-assembly process followed by the hydrothermal method to design MoS_2/g-C_3N_4 nanosheets, which provided abundant available reaction sites for enhanced photocatalytic activities. In this case, the positively charged g-C_3N_4 obtained *via* the protonation method interacts electrostatically with the negatively charged MoS_4^{2-} under hydrothermal treatment.[74] In addition, each atom, *i.e.*, Mo and S, present in MoS_2 also contributed to the formation of chemical bonds during the construction of 2D/2D heterostructures. For example, Zhao *et al.* reported an *in situ* pyrolysis strategy to achieve 2D/2D MoS_2/C_3N_4-based electrodes through Mo–N coordination between 2D-MoS_2 and 2D-C_3N_4, which act as the main active sites for catalyzing the NRR by promoting electron transfer, thus improving the catalytic activity across the MoS_2/C_3N_4 interface.[75] In another study, Swain *et al.* fabricated strong interface coupling between 2D-MoS_2 and 2D-$CaIn_2S_4$ through an S–S linkage, which facilitated the channelization of photogenerated charge carriers throughout the interface of both 2D materials.[76] Furthermore, Wan *et al.* developed an Au-coupled Bi_2WO_6–MoS_2 heterojunction photocatalyst in which the charge transfer process occurred from the surface of Bi_2WO_6 to MoS_2 *via* the interfacial S–O bonds. It was observed that the interfacial S–O bond is derived from the outer sulfur atoms and vertex oxygen atoms present in the MoS_2 layer and WO_6 octahedron of Bi_2WO_6, respectively.[77]

3. Procedures for the synthesis of 2D-MoS_2 and MoS_2-based 2D/2D heterojunction composites

The practical application of various 2D nanomaterials is mainly governed by their exposed active sites, and thus it is an essential requirement to design nanomaterials with properties having large area uniformity and layer controllability. Accordingly, considerable efforts have been devoted to the construction of 2D MoS_2 and MoS_2-based 2D/2D heterostructures with satisfactory yields, controllable thickness, unique size, and controllable morphologies by engineering synthetic techniques. The detailed procedures employed for the synthesis of 2D-MoS_2 together with its 2D/2D heterostructures are depicted in Scheme 2.

3.1 Synthesis of 2D-MoS_2

To date, numerous synthetic procedures have been developed for the synthesis of various nanostructured 2D MoS_2, which can be divided into two routes, *i.e.*, (a) top-down routes including mechanical exfoliation and chemical exfoliation and (b) bottom-up routes including hydrothermal and solvothermal method, chemical and physical vapour deposition, and decomposition method.[32,39]

3.1.1 Top-down routes. The top-down approach mainly relies on the preparation of nanostructured 2D-MoS_2 from its respective bulk counterparts. It is mainly based on the exfoliation of layered bulk structured materials into few or single layers by breaking the van der Waals interaction between the layer *via* various driving forces as follows.

3.1.1.1 Mechanical exfoliation. Similar to the Scotch tape method for the preparation of graphene from graphite, bulk MoS_2 is attached on an adhesive tape and subjected to repeated exfoliation on the support of a substrate to produce a high-quality monolayer phase of MoS_2. Consequently, its pristine crystal structure is the same as that of its bulk. Li and co-workers constructed MoS_2 nanosheets through the mechanical exfoliation method using Al_2O_3 ceramic substrates.[78] As illustrated in Fig. 2a, thin MoS_2 flakes were obtained when the attached Scotch tape was removed from the bulk MoS_2 crystals by repeatedly folding and separating the Scotch tape-adhered MoS_2 flakes. Subsequently, the Scotch tape attached to the MoS_2 thin flakes was tightly pasted onto a clean Al_2O_3 ceramic substrate on the support of Ag–Pd interdigital electrodes and left for about 6 h to maintain the adhesion state. To remove the adhesive

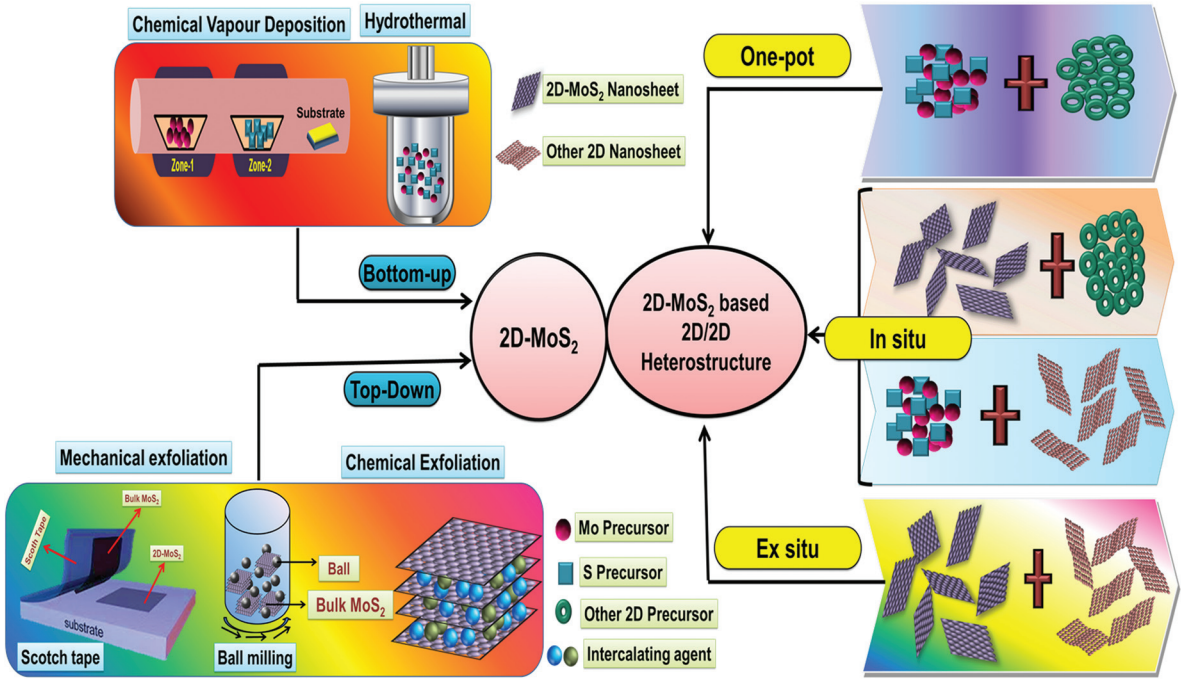

Scheme 2 Schematic illustration of the various techniques used for the synthesis of 2D-MoS_2 and its 2D/2D-heterostructures.

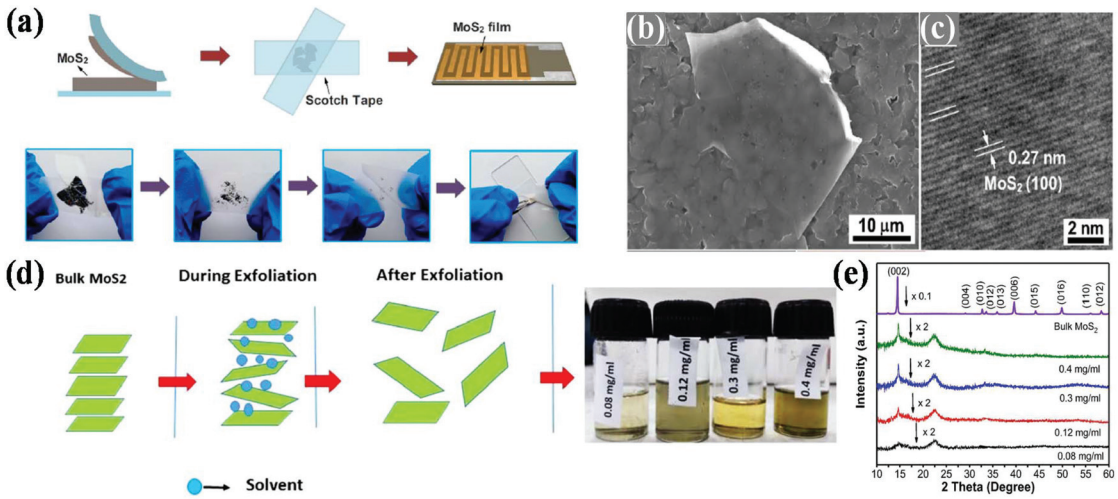

Fig. 2 (a) Schematic diagram showing the mechanical exfoliation technique for the synthesis of MoS_2 nanosheets, and (b) SEM and (c) HRTEM images of MoS_2 nanosheets. Reproduced from ref. 78 (d) Scheme of the synthesis process *via* the liquid-phase exfoliation of MoS_2 nanosheets and (e) X-ray diffraction patterns of bulk MoS_2 powder and MoS_2 nanosheets synthesized using different initial concentrations of bulk MoS_2. Reproduced from ref. 81.

residue from the Scotch tape, acetone was used as the solvent. The as-obtained few-layer microstructure of MoS_2 exhibited a smooth surface on the substrate together with the same pattern as the substrate and it possesses the good crystallinity of MoS_2 nanosheets with an ordered arrangement of lattice fringes, as presented in Fig. 2b and c. However, this process requires a substrate for sample preparation, which gives a very low product yield, and it is very difficult to control the size, shape and thickness of the resulting material. Consequently, this method is not suitable for the large-scale production of the materials. Besides the Scotch tape method, ball milling is another strategy that is also responsible for the synthesis of high-quality 2D MoS_2 nanosheets. Krishnamoorthy *et al.* mechanically delaminated bulk MoS_2 into few-layered MoS_2 nanosheets using the ball milling method. The ball milling method is performed in a ball and bowl made up of tungsten carbide, and *N*-methyl-2-pyrrolidine (NMP) is used as the solvent throughout the reaction. After ball milling at a speed of 300 rpm, the final MoS_2 product is

obtained after washing with ethanol followed by drying.[79] Besides the Scotch tape and ball milling techniques, in 2012, Gacem's group reported an anodic bonding technique, in which high-quality nanosheets with high yield, good optical properties and excellent purity were obtained.[80]

3.1.1.2 Liquid-phase exfoliation. In this method, few-layered materials are prepared directly under the influence of various solvents followed by the joint action of sonication and centrifugation. Here, sonication breaks the weak van der Waals interaction present between the stacking layers without destroying the covalent bonding in each layer.[38] This technique includes ion intercalation, ion exchange and ultrasonic cleavage, which generates a large amount of 2D-MoS_2 with good quality single and few-layered nanosheets. The choice of solvent is a key parameter in liquid exfoliation, where there should be a good match between the solvent and surface tension present between the layers, which minimizes the energy required for exfoliation, thus increasing the exfoliation efficiency. Here, the number of layers in the resulting 2D materials is governed by the choice of solvent together with the concentration of the precursor solute. Gupta and co-workers prepared MoS_2 nanosheets through the liquid-phase exfoliation method using NMP as the exfoliating solvent. From experimental studies, it has been deduced that the presence of a small mole fraction of water in NMP stabilizes the MoS_2 nanosheets in the dispersion during sonication. Particularly, the stability of the MoS_2 nanosheets in the NMP dispersion solution is due to the water molecules confined at the Mo edges of MoS_2, which prevent chemical erosion of the edges. This, enhances the interaction between the NMP solvent and MoS_2, leading to a stable dispersion.[82] Therefore, it has been concluded that the use of solvent during the exfoliation method is not only responsible for the synthesis of two-dimensional nanosheets, but also plays a big role in stabilizing the nanosheets. In the literature on studies regarding liquid-phase exfoliation, it has also been observed that solvents with a low volatile rate hamper the rate of exfoliation and yield of 2D catalysts. Thus, the choice of solvent with a high volatility rate is another crucial factor that should be considered. Accordingly, Sahoo *et al.* employed a cost-effective liquid-phase exfoliation route for the scalable production of high-quality MoS_2 nanosheets using acetone as the solvent. The use of acetone as a solvent overcomes the drawbacks of low-volatility solvents. In this method, the bulk MoS_2 is exfoliated into 2D-MoS_2 nanosheets *via* sonication followed by centrifugation. The synthetic method involves several steps as follows: (i) grinding of bulk MoS_2 using a mortar and pestle followed by drying to evaporate the water and impurities, (ii) addition of acetone to a particular concentration of dried MoS_2 in a glass vial, (iii) treatment in a sonication bath to interrupt the weak van der Waals force present between the adjacent layers, and (iv) finally the supernatant is collected using a micropipette after centrifugation followed by filtration. Fig. 2d depicts the procedure for the synthesis of MoS_2 nanosheets *via* the weakening of van der Waals forces, which helps in thinning the layers, where the exfoliation procedure proceeds with different initial concentrations. As shown in Fig. 2e, the strong diffraction peak observed at the (002) plane decreases gradually with a change in the initial concentration of bulk MoS_2 in a given concentration of solvent, indicating that the bulk MoS_2 is exfoliated to few layers. Moreover, in the case of the ion intercalation mechanism, cations are intercalated into the interlayer spacing of the bulk materials to destroy the van der Waals interaction present between the layers.[81] However, the use of harmful toxic organic solvents, low quantum yield, and small lateral size of the as-obtained sheets limit its large scale utilization by many researchers.

3.1.2 Bottom-up approach. The bottom-up approach is the most compatible method used to fabricate the target substance with certain precursors followed by chemical reactions mainly in the solution phase. In some cases, surfactants are often used, which mainly help to stabilize the products and control their shape, size and morphology.

3.1.2.1 Chemical vapour deposition. The chemical vapour deposition (CVD) approach involves the growth mechanism of the products *via* chemical reactions and has been proven to be a beneficial method to synthesize high-quality substances that are thin and highly conductive, especially MoS_2 films. The CVD method requires a two-furnace approach to control the temperature of both Mo and S precursors separately. In a typical process, the desired product is obtained due to the redox reaction between the reactant precursors on the support or surface of a substrate whenever one or more volatile precursors decompose and react with each other at high temperature and high vacuum conditions. Typically, the growth temperature is maintained about 700–1000 °C and for the growth of 2D-MoS_2 thin layers, various substrates are employed as insulating supports. Initially, the MoS_2 precursors such as Mo, MoO_3, $(NH_4)_2MoS_4$ are deposited on the supporting surface and then subjected to thermal decomposition or sulfurization at an elevated temperature to generate MoS_2 layers with controlled structures.[37,46,83]

In addition, by customizing the essential parameters (growth temperature and time, flow rate of the carrier gas, mass amount, and the position of both the reactant and substrate), a high-quality MoS_2 monolayer can be achieved together with tunable film thickness and large active sites, which are beneficial for interplanar charge transport. Wan and his group demonstrated fractal-shaped single-layer MoS_2 to engineer the active sites of MoS_2 through the CVD method on a fused silica substrate. It was observed that water-soluble polymer-assisted method prevented the formation of the fractal-shaped morphology during the transformation process.[84] Li and co-workers employed a single-step CVD approach (Fig. 3a) for the development of an edge-enriched 2D-MoS_2 thin film with high catalytic efficiency towards the HER. The CVD process was carried out on a wide range of substrates including a silicon wafer, graphite, and glassy carbon. During the synthesis, the total number of edge sites on MoS_2 and its surface area increased when smaller layered MoS_2 grew on large MoS_2 platelets in a perpendicular direction (Fig. 3b). The TEM images in Fig. 3c and d demonstrate the formation of vertically orientated layers, in which vertically aligned nanoflakes are grown on the petal site of MoS_2.[85]

In terms of wafer-scale production with low manufacturing cost and highly crystalline MoS_2, the atmospheric pressure

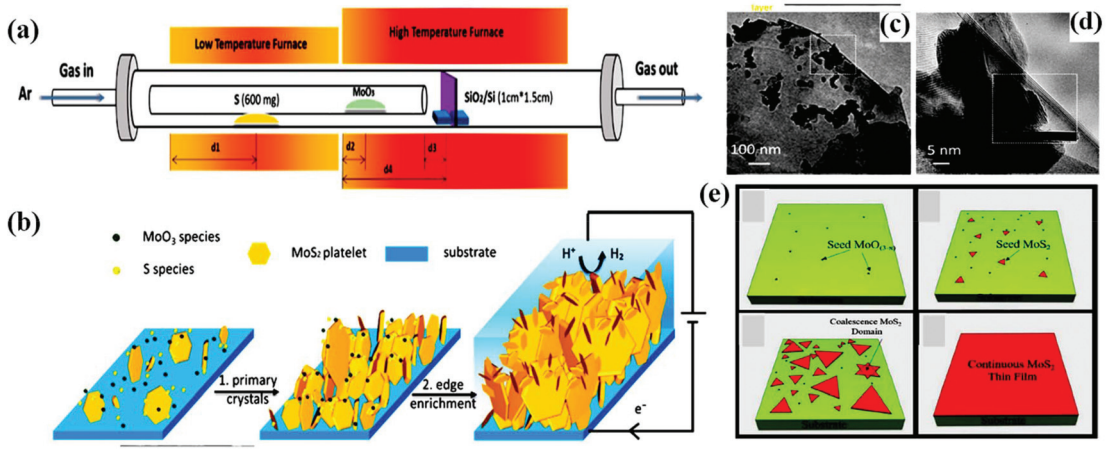

Fig. 3 (a) Schematic representation showing the experimental CVD setup, (b) mechanistic demonstration of the edge enrichment of MoS_2, (c) and (d) TEM images of the petal site showing the nucleation of vertically aligned nanoflakes on the top-layer crystals. Reproduced from ref. 85. (e) Schematic illustration of monolayer MoS_2 growth on a Piranha-treated substrate. Reproduced from ref. 86.

chemical vapour deposition (APCVD) method has emerged as an excellent approach. Gnanasekar and his group developed a high-quality MoS_2 monolayer for the electrochemical hydrogen evolution reaction using a seed promoter-free APCVD method directly on an SiO_2 substrate. The CVD method mainly involves the transport and adsorption of the final growth species on a given substrate followed by the nucleation and future growth of new MoS_2. Initially, at a particular high temperature, the Mo precursors are reduced and are adsorbed on the arbitrary position of the substrate with the flow of carrier gas, which is further subjected to a sulfurization process, resulting in nucleated species. The as-obtained MoS_2 acts as a seed, which allows further growth of another MoS_2 thin film. The overall reaction procedure is depicted in Fig. 3e. From the experiment, the large scale high-quality MoS_2 possessed excellent HER properties.[86] However, using this method, it is very challenging to prepare MoS_2 crystals by controlling the number of layers due to the use of non-crystalline precursors, where it is difficult to control the number of layers of the product material during the reaction.

3.1.2.2 Hydrothermal or solvothermal method. Among the various synthetic methods, the hydrothermal process is preferred by many researchers because it can achieve high surface area, good-quality crystals and controlled morphological composition of the products. It is a growth method in which water and organic and inorganic solvents are used as the reaction medium dissolve the commonly used Mo and S precursor substances. The reaction generally involves the crystallization of a material under high pressure (1 MPa to 1 GPa) and high temperature (100–250 °C) conditions from an aqueous and organic solvent. This technique is very promising due to its safe and simple operation, mild conditions, high purity, low pollution, low cost and easy hybrid dispersion nature. The solvothermal synthesis technique of 2D-MoS_2 basically requires the use of an organic/inorganic sulfur source such as thioacetamide, thiourea and KSCN, and sodium molybdate, ammonium molybdate, and molybdenum trioxide as the Mo source. By controlling the reaction temperature and time, the size, crystallinity and morphology of the resultant 2D-MoS_2 can be modulated to some extent.[34,37,87] Muralikrishna and co-workers synthesized 2D MoS_2 nanosheets with high catalytic activity *via* a facile hydrothermal approach, which exhibited superior electrocatalytic HER activity.[88] The sulfur source used was thiourea, which acts as both a reducing agent and stabilizer, which stabilizes the defect-rich MoS_2 nanosheets. Under hydrothermal conditions, *i.e.*, high temperature and high pressure, firstly Mo(VI) present in MoO_3 is reduced to Mo(IV) under the influence of excess thiourea. Finally, the reduced Mo(IV) couples with the excess thiourea and undergoes a nucleation process and is converted to MoS_2 nanoparticles, which then grow into defect-rich nanosheets. The use of ammonia during the reaction procedure has a great advantage over the stacking of MoS_2 nanosheets and facilitates the production of thin nanosheets very easily. In another study, Swain *et al.* prepared crumpled-type exfoliated MoS_2 nanosheets under simple one-step hydrothermal conditions. It was also observed that without the inclusion of any surfactants, the hydrothermal technique is also responsible for the production of highly efficient morphological-oriented structured MoS_2 nanosheets.[89] In this regard, Swain *et al.* designed rose-like MoS_2 nanoflowers by employing a facile hydrothermal technique using only water as the solvent. The as-obtained MoS_2 exhibited like a rose-like nanoflower structure with a diameter of 500–800 nm. During hydrothermal treatment from the precursor salt solutions of Mo and S, firstly the MoS_2 nanoparticles self-aggregate and undergo a reduction in surface energy and get converted into partially monodispersed isolated MoS_2 microspheres. Under a prolonged hydrothermal process with an increase in temperature, petal-like nanosheets of MoS_2 are grown on the surface of the MoS_2 spheres, thus displaying a hierarchical rose-like MoS_2 nanoflower morphology.[90] Several studies have also reported that the introduction of the combined effect of both defects and S-vacancy results in superior catalytic activity. Li *et al.* employed a facile hydrothermal

method for the synthesis of multilayered MoS_2 nanosheets in *N*,*N*-DMF using $(NH_4)_2MoS_4$ as both the Mo and S precursors. The as-obtained MoS_2 consisted of point-defect S-vacancies together with coordinated Mo regions, which reduced the free energy of hydrogen adsorption during the HER.[91]

3.2 Techniques for the synthesis of MoS_2-based 2D/2D heterostructures

The fabrication of MoS_2-based 2D/2D heterostructure composites with controllable nanostructured properties is a great challenge in the current research scenario. The techniques for the synthesis of MoS_2-based 2D/2D heterostructures are broadly categorized into two classes: (a) *ex situ* synthesis method and (b) *in situ* and one-pot synthesis method.[53,65] Among the various reports in the literature, only a few are discussed in the following section.

3.2.1 *Ex situ* synthesis method. The *ex situ* synthesis method is also known as the "self-assembly method", which plays a great role in the fabrication of MoS_2-based 2D/2D heterostructure composites. In this technique, two individual pre-synthesized 2D layered materials undergo the *ex situ* assembly method. The pre-synthesized components are synthesized through (i) exfoliation from their bulk samples through mechanical or chemical methods, (ii) solid-phase grinding, (iii) liquid-phase ultrasonic adsorption, (iv) hydrothermal treatment, and (v) calcination. Subsequently, each pre-synthesized 2D material is manually stacked through weak van der Waals interlayer interaction *via* the self-assembly process give rise to 2D/2D layered heterostructures. In *ex situ*-mediated 2D/2D heterostructure composites, the photo/electrocatalytic activity is mainly attributed to their interlayer distance and orientation of the superposition lattice of each 2D–2D material.[53,62,65]

It should be noted that in some cases, a single 2D material can be directly exfoliated from its bulk under the action of some solvent and exfoliation treatment, whereas in some cases, the neat material can be prepared from its molecular precursors directly. For example, Xiong *et al.* fabricated a 2D/2D MoS_2/CdS heterojunction by employing an adsorption–calcination process, as shown in Fig. 4a. This method involved the preparation of neat 2D-MoS_2 from its commercial bulk counterpart through exfoliation, whereas neat CdS was prepared through the solvothermal–precipitation route followed by exfoliation to get an ultrathin nanosheet structure. Then, the two above-prepared neat materials were mixed through the adsorption process *via* sonication, and then further subjected to a calcination process (Ar atmosphere), which facilitates the close contact between the two components.[92] Similarly, Jeong *et al.* fabricated a black phosphorus (BP)@MoS_2 2D/2D nanocomposite by mixing as-exfoliated BP and MoS_2 through the ball milling method followed by high energy ultrasonication.[93] Meanwhile, another type of 2D/2D nanojunction was constructed through the direct assembly strategy followed by the reflux method, in which MoS_2 nanosheets with 6 to 8 layers were prepared through a simple solvothermal method followed by exfoliation strategy, whereas Bi_2WO_6 nanosheets were prepared through a hydrothermal method, which were then dispersed in NMP (*N*-methyl-2-pyrrolidone) solvent *via* sonication followed by reflux. The large and close 2D/2D contact surface of the Bi_2WO_6/MoS_2 heterojunction is favorable for interfacial charge transfer. In heterojunction materials, the abundant reductive active sites and high electron conductivity are mainly dependent on the controlled S–Mo–S layer of MoS_2 nanosheets, which look like curled edges. It was observed that the controlled curled edges of MoS_2 possess a larger interlayer spacing (0.702 nm and 0.685 nm) compared to that of bulk MoS_2 (0.61 nm).[77]

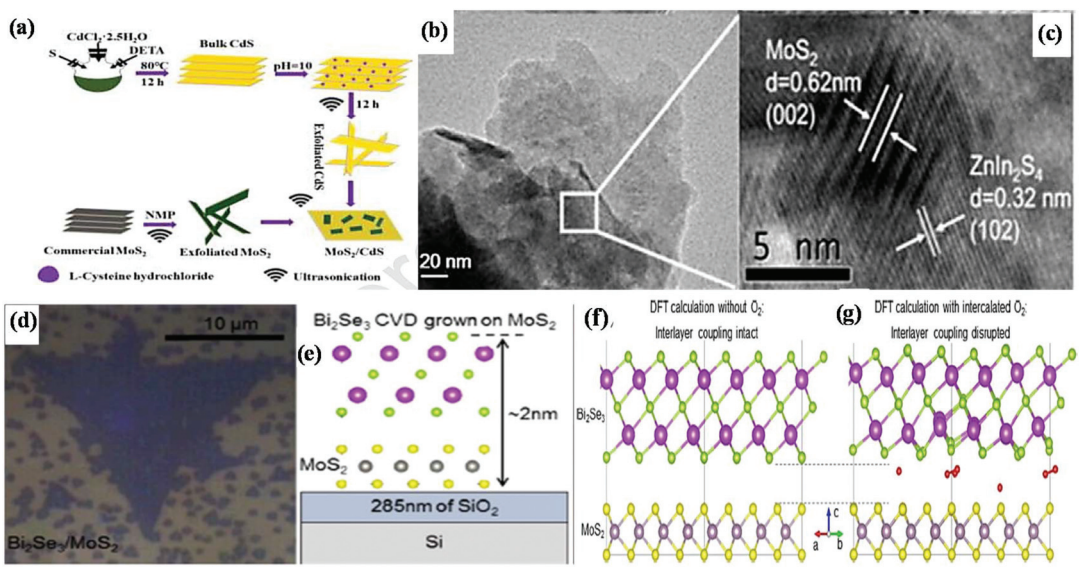

Fig. 4 (a) Strategy for the fabrication of MoS_2/CdS heterojunctions. Reproduced with permission.[92] (b) SEM and (c) HRTEM images of $ZnIn_2S_4$/MoS_2 composite. Reproduced with permission.[95] (d) Optical image and (e) side-view diagram of Bi_2Se_3/MoS_2 heterostructure, (f) charge redistribution representation of the interlayer region and the interlayer coupling and (g) interlayer coupling with interlayer separation by O_2 molecule of Bi_2Se_3/MoS_2. Reproduced with permission.[96]

In addition, *ex situ* strategies are also regulated through ball milling and the mechanical grinding method. Li *et al.* developed a 2D/2D C_3N_4/MoS_2 heterojunction photocatalyst with a stable intrinsic crystal structure *via* a simple mechanical grinding method. They mixed an appropriate amount of commercial MoS_2 and g-C_3N_4 and put it on ball grinder for mechanical operation.[94] However, good interfacial contact was also achieved through the electrostatic self-assembly approach, considering the zeta potential value of each neat material. By following this strategy, Huang *et al.* designed a sheet-on-sheet 2D/2D $ZnIn_2S_4/MoS_2$ heterostructure, in which MoS_2 nanosheets were well connected with ultrathin sheets of $ZnIn_2S_4$. Briefly, initially, both pristine materials have negatively charged surfaces with a zeta potential value of −23.8 mV and −45.7 mV for the MoS_2 and $ZnIn_2S_4$ nanosheets, respectively. However, after treatment with poly(diallyldimethylammonium chloride) (PDDA), the negative surface of the MoS_2 nanosheets in the aqueous dispersion changed became positive with a zeta potential value of +36.5 mV. After the modification, strong electrostatic attraction occurred between the negatively charged $ZnIn_2S_4$ and positively charged PDDA-MoS_2, which provided the necessary condition for the development of a 2D/2D heterostructure with an intimate contact interface for efficient charge separation and migration. The sheet-on-sheet structure with large contact interface and individual clear fringes for neat MoS_2 and neat $ZnIn_2S_4$ in the 2D/2D $ZnIn_2S_4/MoS_2$ heterostructure is presented in Fig. 4b and c, respectively.[95]

Besides the above-mentioned methods, the transfer process in which a single 2D material originates from the CVD method is also treated as an *ex situ* method for the direct configuration of 2D/2D van der Waals heterostructures. Wang *et al.* developed a method for the direct growth of MoS_2 on h-BN by employing an *ex situ* path. The MoS_2/h-BN van der Waals heterostructure was prepared through a two-step poly(methyl methacrylate) (PMMA)-assisted transfer approach. The method involved the direct transfer of CVD-grown MoS_2 to a new SiO_2/Si substrate containing h-BN to achieve a 2D/2D heterostructure.[68] It was noted that for the synthesis of more active 2D/2D van der Waals heterostructures, parameters such as the interlayer separation distance and stacking lattice orientation should be optimized. Therefore, Hennighausen *et al.* tuned the interlayer through the intercalation and deintercalation of diffusive atmospheric oxygen molecules. By regulating the atmospheric oxygen, the interlayer coupling in the 2D/2D Bi_2Se_3 heterostructure could be reduced under laser or thermal energy. The synthetic method involved the initial growth of an MoS_2 monolayer followed by the growth of Bi_2Se_3 on top of it through vapour phase chalcogenization and vapour phase deposition, respectively. The successful uniform and regular growth of one layer of Bi_2Se_3 on one layer of MoS_2 crystal on SiO_2 and the strong van der Waals epitaxial structure were clearly observed from the optical image (Fig. 4d) and side-view diagram (Fig. 4e), respectively. The DFT calculation, as shown in Fig. 4f and g, predicted the uniform charge redistribution in the interlayer region. The relatively small-sized O_2 molecules are easily intercalated in the interlayer region, as predicted by DFT calculation (Fig. 4g), which facilitates charge separation by tuning the interlayer coupling, thus making the material electronically independent.[96] Subsequently, Biroju and coworkers accomplished the synthesis of sequentially stacked atomic layers throughout the development of an MoS_2/graphene van der Waals solid through the wet transfer CVD method. In this case, a single layer of graphene was grown on three-four atomic layers of MoS_2 by mixing and matching various layers, resulting in a transparent flexible electrode, and its efficacy in the HER was demonstrated.[97]

3.2.2 *In situ* synthesis method. In addition to the *ex situ* approach, an alternative technique has been implemented, which is commonly known as the "*in situ* growth method", for the fabrication of MoS_2-based 2D/2D heterostructures. The methods for the *in situ* growth of MoS_2-based 2D/2D heterostructure may be (i) a one-step growth method or multistep transformation approach, in which the direct growth of one 2D layered material occurs on the surface of primarily synthesized 2D-MoS_2 substrates or *vice versa* through various techniques such as wet chemical synthesis, chemical vapor deposition method (CVD), and nanoconfinement methods. (ii) Direct growth of MoS_2-based 2D/2D heterostructure composites. The experimental studies indicate that in some cases, during the synthesis of 2D-MoS_2-based 2D/2D heterostructure, firstly, anions from the Mo source, *i.e.*, MoS_4^{2-} and MoO_4^{2-}, are generated and adsorbed on the other 2D material, and then reduced to MoS_2 upon the addition of the S source under heat treatment. Generally, epitaxial growth and direct growth are the two approaches employed for the *in situ* growth of 2D/2D heterostructures. From a number of experimental surveys, it has been deduced that among the various synthetic techniques, the CVD and wet chemical synthesis methods are the commonly used methods, resulting in distinct types of contagious interfaces together with potential catalytic application depending on the interface.[53,62,65]

For the CVD technique, a substrate and a volatile substance are required, in which one pre-synthesized 2D material is employed as the 2D substrate on which the volatile substances are exposed so that the other 2D materials can easily react or decompose for the growth of 2D/2D heterostructures. When the reaction is complete, volatile byproducts are produced, which are removed from the reaction system with the help of a gas flow. This is the most promising technique for the synthesis of hybrid materials based on the 2D/2D architecture.[53,65] Moreover, it has been observed that during the growth process, given that the precursors of both 2D materials coexist in the vapor phase, there may be a cross-contamination issue with the various elements present in the as-fabricated 2D/2D heterostructure. However, this issue can be mitigated through the two-step CVD growth strategy, in which two 2D composite layers are synthesized in two separate steps and the growth process on a metal substrate is found to be more effective. This method offers high-quality 2D/2D TMD heterostructures together with a pure phase, resulting in versatile applications in various fields.

Zhai *et al.* developed 2D-van der Waals heterostructures using $NiTe_2/MoS_2$ through a two-step *in situ* CVD growth

method. The as-fabricated heterostructure possessed a better heterointerface and enhanced electronic and optoelectronic performances, which were found to be three orders greater compared to that of single 2D-MoS_2. The epitaxial growth of the van der Waals heterostructure is mainly attributed to the similar hexagonal symmetry of both 2D layered materials. In this case, firstly, by using the low-pressure chemical vapour deposition (LPCVD) strategy, MoS_2 monolayers are grown on SiO_2/Si substrates. It should be noted that the LPCVD method is easier and much more beneficial for designing high crystalline monolayer MoS_2 with a clean and triangular surface. After the formation of triangular MoS_2, it is employed as a substrate for the growth of an $NiTe_2$ layer, resulting in an $NiTe_2/MoS_2$ van der Waals heterostructure, in which the bottom MoS_2 layer and upper $NiTe_2$ thin film layer are vertically stacked with each other through weak van der Waals forces (Fig. 5a). Fig. 5b depicts the two-step CVD growth procedure for the synthesis of the $MoS_2/MoTe_2$ heterostructure. The vertical heterostructure of $NiTe_2$ on the monolayer of MoS_2 is depicted in the SEM image in Fig. 5c. According to the AFM image (Fig. 5d), the thickness of the upper $NiTe_2$ and bottom MoS_2 is 5.20 nm and 0.85 nm, suggesting the formation of five and single triple-layers comprised of $NiTe_2$ and MoS_2, respectively.[98]

Furthermore, it has been demonstrated that vertical bilayers with the strongest interlayer coupling and shortest interlayer spacing can be obtained based on the twisted stacking angles with equivalent crystallographic alignment in van der Waals heterostructures, such as A–A or A–B-type stacking. Due to this type of modulation in the interlayer coupling, the heterostructure exhibits superior optical and electrical properties, *i.e.*, it facilitates the interlayer transfer and migration of charge pairs, thus reducing the charge recombination more efficiently. Zhang *et al.* reported the epitaxial growth of an MoS_2/WS_2 heterostructure, in which MoS_2 films were grown on top of WS_2 through a two-step CVD growth approach in the A–A and A–B stacking fashion. The top and side atomistic views of the heterostructure are presented in Fig. 5e. In this case, MoS_2 is nucleated at the edges of WS_2 in a triangular shape with only 0° and 60° orientations with respect to the bottom WS_2 layer, maintaining the most stable A–A and A–B stacking configurations, respectively. According to the Raman spectra study, the A–B stacked bilayers had a strong lower breathing frequency mode than the A–A stacked bilayers, which possessed a shorter interlayer distance and stronger interlayer coupling.[99]

Further, Shi and co-workers designed a vertically stacked van der Waals heterostructure *via* the temperature-mediated selective growth of 2D-MoS_2 on 2D-WS_2 and *vice versa* using Au foil as the substrate material in the two-step CVD method.[100] Briefly, as shown in Fig. 5f, in the first step, the individual monolayer MoS_2 or WS_2 was grown on Au foil from its precursor element (MoO_3 or WO_3, respectively) under a low-pressure CVD method. In the second step, the as-prepared MoS_2/Au or WS_2/Au samples were subjected to further heat treatment in a furnace in the presence of the corresponding metal precursors for the subsequent preparation of the 2D/2D MoS_2/WS_2 heterostructure. The uniform distribution and vertical growth of MoS_2 or WS_2 (triangular domain) on WS_2/Au or MoS_2/Au were clearly observed from the SEM images (Fig. 5g and h), respectively. In contrast, Lee *et al.* proposed a novel method for the direct growth of MoS_2/graphene using the CVD technique in the presence of a UV/ozone-treated solid C-source, as illustrated in Fig. 5i. MoO_3 and sulfur powder were used as the MoS_2 precursors, while for the growth of graphene, 1,2,3,4-tetraphenylnaphthalene (TPN) was used as the precursor. Firstly, an MoS_2 monolayer was prepared using the molten-salt-assisted CVD method, resulting in the formation of an MoS_2/SiO_2/Si substrate, on which the graphene layer was grown. However, UV/ozone treatment of the spin-coated TPN

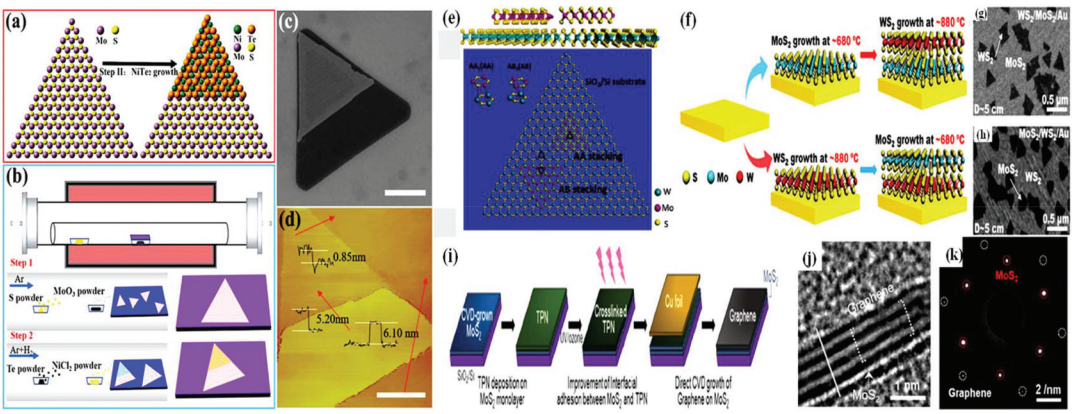

Fig. 5 (a) Schematic illustration of the vertical stack and (b) two-step CVD growth process for $NiTe_2/MoS_2$ heterostructure. (c) SEM image depicting the vertical heterostructure of $NiTe_2/MoS_2$ on an SiO_2/Si substrate. (d) AFM images of vertical stacking region and interfacial region. Reproduced with permission.[98] (e) Atomic representation of vertically assembled A–A and A–B stacked (top and side views) MoS_2/WS_2 bilayers. Reproduced with permission.[99] (f) Schematic diagram representing the two-step CVD growth process. (g) and (h) SEM images of WS_2/MoS_2/Au and MoS_2/WS_2/Au, respectively. Reproduced with permission.[100] (i) Schematic representation showing the direct growth of graphene/MoS_2 heterostructure on SiO_2/Si substrate, (j) HRTEM image of graphene/MoS_2 heterostructure and (k) SAED image of MoS_2 monolayer (red circle) and graphene (white circle). Reproduced with permission.[101]

on $MoS_2/SiO_2/Si$ substrate increased the interfacial adhesion between the two layers, and the final growth of graphene occurred under Cu vapor when Cu foil was placed on the TPN-coated $MoS_2/SiO_2/Si$ substrate, resulting in the formation of the graphene/MoS_2 heterostructure. The successful growth of graphene layers on the monolayer MoS_2 and sharp interface between graphene and MoS_2 were confirmed from the cross-sectional TEM image (Fig. 5j). Furthermore, the SAED pattern (Fig. 5k) confirmed the clean diffraction spots for both MoS_2 and graphene in the graphene/MoS_2 heterostructure, suggesting that the 2D/2D heterostructure is suitable for application in an ultrathin electronic device with high surface-sensitive properties.[101]

Besides the CVD method, the *in situ* process for the synthesis of 2D/2D heterostructures can also be mediated through the hydrothermal technique. Ji *et al.* modified 2D-CeO_2 on 2D-MoS_2 nanosheets through an *in situ* facile hydrothermal technique to design a new 2D/2D MoS_2/CeO_2 heterojunction, which possessed abundant reactive centers for degradation reactions.[102] Throughout the reaction, the Ce^{4+} ions from 2D-CeO_2 generated sufficient oxygen vacancies by utilizing photoexcited charge carriers and acted as redox centers. In this case, firstly, 2D CeO_2 nanosheets were prepared *via* the hydrothermal method followed by calcination, and then introduced to the Mo and S precursors through the hydrothermal process, resulting in the formation of 2D/2D MoS_2/CeO_2. The morphological characterization *via* TEM and HRTEM of 2D/2D MoS_2/CeO_2 indicated that both 2D nanosheets were uniformly combined, in which the 2D-CeO_2 nanosheets were located on the 2D-MoS_2 nanosheets in a vertical and lateral fashion. Furthermore, Yuan *et al.* developed face-to-face 2D/2D black phosphorus (BP)/MoS_2 through the solvothermal method, in which MoS_2 nanosheets were homogeneously dispersed on the surface of BP nanosheets. It was observed that the interaction occurred between the precursors of MoS_2 and the oxygen present in the exfoliated BP nanosheets, which exhibited a large intimate contact interface and abundant exposed edges for superior catalytic activity.[103]

Besides the face-to-face heterostructure, the *in situ* synthesis method is also responsible for the formation of highly efficient 2D/2D heterostructure materials with electrostatic interaction between them. By combining electrostatic self-assembly chemistry with the *in situ* hydrothermal strategy, Nayak *et al.* constructed an MoS_2/Ni–Fe LDH nanocomposite.[104] Particularly, 2D-MoS_2 nanosheets underwent a nucleation and growth process on the edge-shared MO_6 octahedron site (positively charged surface) provided by 2D-LDH, resulting in the formation of 2D/2D MoS_2/Ni–Fe LDH. The overall growth process is governed through the electrostatic self-assembly and O_2 vacancies in the LDH nanosheets, which effectively co-ordinate with the Mo^{4+} and S^{2-} ions during the *in situ* hydrothermal reaction. Interestingly, both the exfoliation of strongly bonded positive layers of LDH and the growth of MoS_2 nanosheets on the positively charged surface of the exfoliated LDH take place in one step during the hydrothermal reaction. Swain *et al.* developed a hierarchical structure with a 2D/2D contact heterojunction in which the crumpled sheets of $MgIn_2S_4$ flowers were covered with petal-like MoS_2 nanosheets through S–S linkages at the interface.[90] As illustrated in Fig. 6a, under hydrothermal treatment, the MoS_2 nanopetals derived from the MoS_2 nanoflowers under ultrasonication mixed with the precursor salt solution (Mg, In, and S) of $MgIn_2S_4$, resulting in the formation of an $MoS_2/MgIn_2S_4$ marigold flower-like morphology. The resulting 2D/2D heterojunction is constructed in

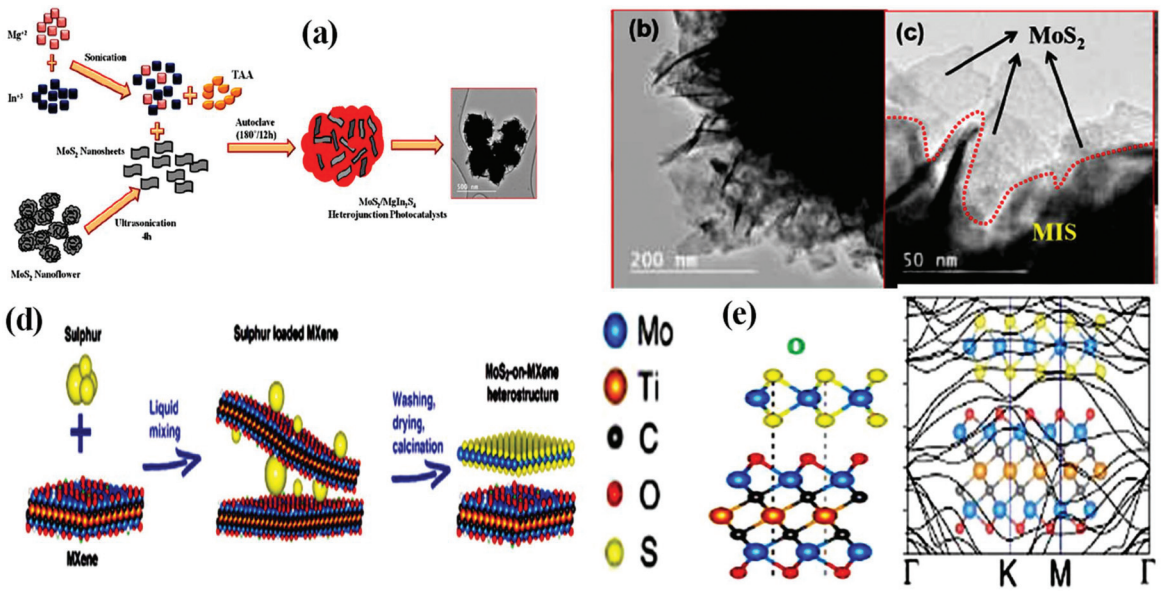

Fig. 6 (a) Schematic diagram showing the growth mechanism and (b) and (c) corresponding HRTEM images of $MoS_2/MgIn_2S_4$ heterojunction photocatalyst. Reproduced with permission.[90] (d) Schematic representation of the fabrication of MoS_2/MXene hybrids and (e) structural stacking patterns and electronic band structure of $MoS_2/Mo_2TiC_2O_2$. Reproduced with permission.[105]

such a way that both neat counterparts are tightly joined with each other in a zigzag face-to-face and face-to-edge contact, providing a large number of exposed unsaturated S active sites for the photocatalytic reaction. The TEM images (Fig. 6b and c) of the $MoS_2/MgIn_2S_4$ heterojunction indicate the wrapping of MoS_2 nanosheets around the micro-sized petals of the $MgIn_2S_4$ flowers.

Furthermore, highly active MoS_2-based 2D/2D heterostructures can also be achieved *via* the partial replacement of S in 2D-MoS_2 with another anion such as phosphide and carbide having a similar atomic radius or the addition of S to another non-MoS_2-based material.[105] 2D MoP/MoS_2 heterostructure nanosheets were constructed by Wu and coworkers, in which the S present in MoS_2 underwent rational substitution with P. Typically, MoS_2 nanosheets were evenly distributed and grown on CC cloth under hydrothermal treatment, and then MoP was obtained on the MoS_2 nanosheet template under phosphorization treatment. However, the partial replacement of S with P should be controllable so that a part of the MoS_2 phase remains in the final product to maintain the 2D/2D MoP/MoS_2 sheet-like heterostructure. It was demonstrated that the as-fabricated 2D/2D heterostructure possessed rich active sites and good conductivity.[106] In another study, Chen *et al.* designed a 2D MoS_2-on-MXene heterostructure *via* the *in situ* sulfidation of a molybdenum-containing 2D-Mxene ($Mo_2TiC_2T_x$) material (Fig. 6d). In the $Mo_2TiC_2T_x$ structure, one layer of Mo atoms is present on the surface of the $Mo_2TiC_2T_x$ MXene, and thus a part of the surface Mo–O pattern can be controllably transformed into an Mo–S motif on the MXene surface under *in situ* sulfidation, resulting in the formation of an $MoS_2/Mo_2TiC_2T_x$ heterostructure with intimate interfacial interactions. The schematic mechanism suggests that under the liquid mixing process, sulfur-incorporated MXene layers are initially derived, which are further subjected to heating in an inert atmosphere, producing the final product followed by the transformation of Mo–O to Mo–S and removal of residual S simultaneously. The stable structural and electronic properties of the resulting heterostructure were depicted from the computational investigation, as shown in Fig. 6e. According to the position of the Mo and S atoms in MoS_2 with respect to O and Ti in $Mo_2TiC_2O_2$, respectively, it was deduced that the integration between MoS_2 and $Mo_2TiC_2O_2$ resulted in enhanced conductivity, which is suitable for application in Li-ion batteries.[105]

3.2.3 One-pot synthesis method. The one-pot synthesis method, also known as one-step synthesis, is another exciting *in situ* advance technique used for the fabrication of 2D/2D-based heterostructures. This process is more advantageous over the two abovementioned methods, *i.e.*, *ex situ* and *in situ* synthesis methods, which proceed through two or more than two complicated processes. Thus, the involvement of these complicated steps limits the industrial utilization of the resulting hybrids. In contrast, the main advantage of the one-pot technique is its time-saving behavior. In the one-pot method, the precursor salt solutions of both 2D materials are combined in one step, *i.e.*, the individual salt precursors are treated in one step, resulting in the formation of 2D/2D products.[65,107] Zhang and coworkers reported the synthesis of an $MoS_2/CdIn_2S_4$ 2D/2D flower-like heterojunction *via* a cost-effective one-pot self-assembly hydrothermal method. The intimate contact between MoS_2 and $CdIn_2S_4$ nanosheets mainly originates from the electrostatic attraction developed between the negatively charged MoS_2 surface with Cd and In ions in $CdIn_2S_4$ during the one-pot reaction.[108] Further, Fu and coworkers reported a unique method to achieve strong interfacial coupling between MoS_2 and g-C_3N_4 ultrathin van der Waals layers, involving self-assembly followed by thermal treatment. The reaction mechanism is illustrated in Fig. 7a. In this case, initially, the molybdenum (Na_2MoO_4) and g-C_3N_4 (dicyandiamide) precursors undergo a self-assembly process in acid solution, resulting a layer-by-layer structure, which is then softly ground with sodium sulphate solution to obtain a ground mixture. Consequently, the layered complex is uniformly coated on the Na_2SO_4 crystal, which is subjected to thermal processing, resulting in the formation of an ultrathin MoS_2/g-C_3N_4 van der Waals layer heterostructure. Briefly, the MoS_2 sheet originates from the reaction of MoO_3 with S *via* the thermal reaction of either the surface sulphate radical, which releases S or H_2S, or the precursors of g-C_3N_4, whereas the g-C_3N_4 ultrathin layer is developed on MoS_2 due to the polymerization of dicyandiamide. The DFT study revealed that through the abovementioned synthetic method, strong electronic coupling is created between Mo of MoS_2 and the N atom in g-C_3N_4 in MoS_2/g-C_3N_4 which is highly beneficial for its electrocatalytic performance.[109] Similarly, Dong and coworkers constructed an S-doped g-C_3N_4/MoS_2 2D/2D face-to-face heterojunction through the hydrothermal-polymerization method, as depicted in Fig. 7b.[110]

To date, the exploration of the one-pot CVD process for the controlled synthesis of 2D/2D hybrid materials has rarely been discussed although this method is very scalable, versatile and time-saving. In the literature, only a few works have been reported on the one-pot CVD method towards the synthesis of hybrid materials. Yu and co-workers proposed a one-pot CVD strategy for the successful fabrication of MoS_2 microflowers on VS_2 microflakes by using suitable precursors on macroporous carbon fiber paper as the substrate under atmospheric pressure, and the reaction was performed in a one-temperature-zone furnace.[111] The procedure for the fabrication of the MoS_2/VS_2 hybrid is schematically illustrated in Fig. 7c. Typically, the metal precursors are positioned side-by-side, whereas the S element is placed at an upstream position in the quartz boat together with CFP in the middle of the furnace. The uniform growth of the MoS_2/VS_2 hybrids on the CFP was achieved by increasing the temperature to 800 °C under the flow of a gas mixture. The SEM images of the MoS_2/VS_2 hybrid at different magnifications (Fig. 7d–f) demonstrated the uniform distribution and full coverage of MoS_2 on the VS_2 microflakes. By modulating the temperature from low to high, they predicted that the VS_2 nanoflakes are derived initially at a lower temperature, and later with an increase in the reaction temperature (high temperature), MoS_2 microflowers grow on

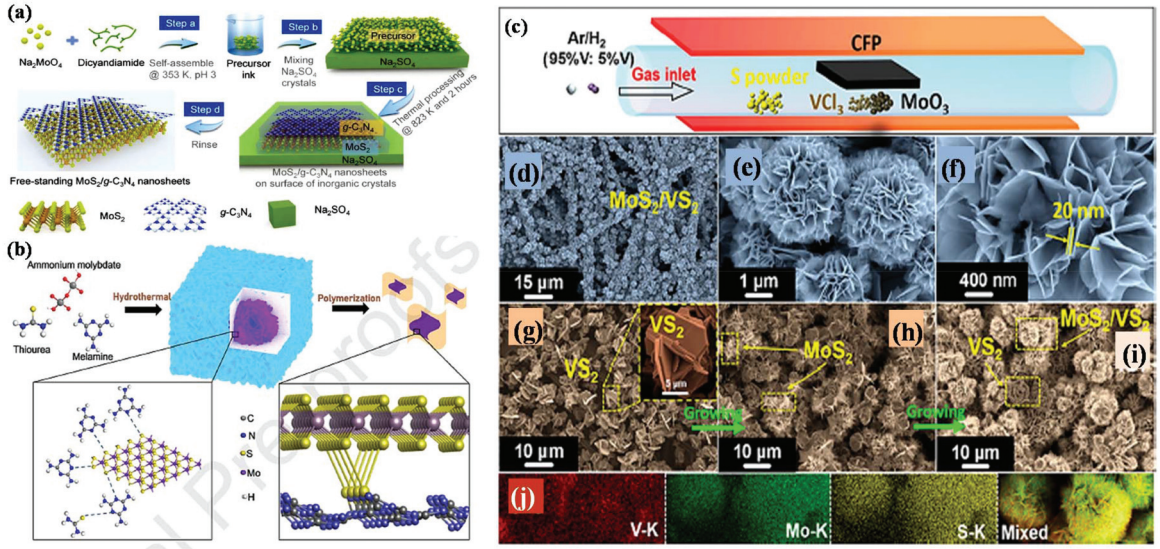

Fig. 7 (a) Schematic illustration of the synthetic strategy for free-standing $MoS_2/g\text{-}C_3N_4$ vdW layers. Reproduced with permission.[109] (b) Schematic representation of the synthesis of MCN nanocomposites *via* the hydrothermal-polymerization method. Reproduced with permission.[110] (c) Schematic diagram representing the one-pot CVD process for the preparation of the MoS_2/VS_2 hybrid, (d–f) SEM images at different magnifications observed for MoS_2/VS_2 hybrid, (g–i) TEM images of the MoS_2/VS_2 hybrid at different temperatures and (j) EDX colour elemental mapping of the MoS_2/VS_2 hybrid. Reproduced with permission.[111]

VS_2. Fig. 7g–i illustrate the morphological evolution of the MoS_2/VS_2 hybrid at different temperatures. Depending on the temperature, four primary chemical reactions occur, as illustrated by eqn (1)–(4). The successful synthesis and the near-surface elemental distribution of the VS_2/MoS_2 hybrid can be clearly observed in Fig. 7j.

$$8H_{2(g)} + S_{8(g)} \rightarrow 8H_2S_{(g)}, \quad T = \sim 150\,^{\circ}C - 180\,^{\circ}C \tag{1}$$

$$2VCl_{3(s)} \rightarrow VCl_{4(g)} + VCl_{2(s)}, \quad T = \sim 270\,^{\circ}C - 300\,^{\circ}C \tag{2}$$

$$2H_2S_{(g)} + VCl_{4(g)} \rightarrow VS_{2(s)} + 4HCl_{(g)}, \quad T = \sim 270\,^{\circ}C - 300\,^{\circ}C \tag{3}$$

$$MoO_{3(s)} + 3H_2S_{(g)} \rightarrow MoS_{2(s)} + S_{(s)} + 3H_2O, \quad T = 700\,^{\circ}C - 750\,^{\circ}C \tag{4}$$

In addition to the abovementioned report, Woods *et al.* synthesized an MoS_2/WS_2-based 2D/2D van der Waals heterostructure *via* one-pot CVD followed by metallic seed layer growth under sulfurization treatment.[112] It should be noted that the transition between the vertical and horizontal structure can be controlled by controlling the thickness of the seed-layer, and the horizontal orientation in the 2D/2D hybrid can be derived by using a metallic seed layer thinner than 3 nm. The authors demonstrated a horizontally oriented MoS_2/WS_2 stacked layered heterostructure by selecting a goldilocks metallic seed layer with a thickness of 1 nm. The growth procedure of MoS_2/WS_2 involves the sequential magnetron sputtering of W and Mo on an Si/SiO_2 substrate followed by sulfurization. The completion of sulfurization was confirmed by the change in colour from blue to light green, which completely fulfils the defined patterning of the MoS_2/WS_2 film.

4. Emerging photo/electrocatalytic applications of 2D-MoS_2 and MoS_2-based 2D/2D heterostructures

Considering the demand for nanomaterials towards energy and environmental applications, 2D-MoS_2 serves as an excellent material with important roles in the field of electrocatalysis and photocatalysis and contributes to energy production such as hydrogen evolution, ammonia generation, and CO_2 reduction. In terms of photocatalysis, on going from bulk 3D structured MoS_2 to 2D MoS_2, the band gap increases as it changes from indirect to direct, thus decreasing the possibility of electron hole recombination. In contrast, in the field of electrocatalysis, to achieve a superior electrocatalytic performance, the interfacial structure of 2D-MoS_2 plays the pivotal role. Again, studies have suggested that the photo/electro-activity of 2D-MoS_2 is mainly attributed to its high stability, broad absorption capacity, number of layers and presence of exposed active sites originating from the unsaturated coordinated S atoms (dangling S bond) and Mo edges.[7,32,45,113–120] However, although it is considered as one of the strategic materials in the field of photo/electrocatalysis, its low electrical conductivity, small surface area and restacking issues based on the number of layers limit its catalytic application as a single material.[32,45,51,121] Hence, different approaches such as exfoliation, doping, and formation of hybrid heterostructures and composites have been developed to minimize the drawbacks

associated with MoS_2. Among the different approaches, the development of hybrid structures regarding MoS_2-based 2D/2D composite materials is one of the latest research trends. Here, in the application part, we present a brief overview of the energy and environmental applications of the recently reported 2D MoS_2 and MoS_2-based 2D/2D heterostructures.

4.1 Hydrogen evolution

To achieve a post-fossil fuel regime, molecular hydrogen is considered as environmentally friendly clean energy and also regarded as a promising alternative for future energy sustainability. In the recent literature, the production of hydrogen through very promising and convenient methods such as H_2O splitting catalyzed by various catalysts is considered a novel approach.[3,5,6,73,76,122–126] Moreover, H_2O can be split into hydrogen over 2D-MoS_2 both photocatalytically and electrocatalytically, as summarized in the following section.

4.1.1 Electrocatalytic H_2 evolution. The electrochemical water splitting reaction is regarded as another promising and efficient approach that can produce hydrogen fuel in high purity by utilizing electrical energy and water. The electrochemical hydrogen evolution reaction (HER) is an environmentally benign and cost-effective method that mainly occurs in different electrode-electrolytic systems. Currently, MoS_2 is regarded as the most promising electrocatalyst and widely investigated for the HER process.[116,127,128] Generally, the HER can be studied under both acidic and alkaline reaction conditions, and in both cases, it involves three reaction steps, which are governed by two mechanistic pathways, *i.e.*, the Volmer–Heyrovsky and Volmer–Tafel mechanisms. The first step is the Volmer or discharge step, which involves the adsorption of a hydrogen ion (H_{ads}) on the electrode surface, resulting from the coupling reaction between the electrons with a proton (in acidic condition) and a water molecule (in alkaline medium). After the adsorption of the hydrogen ion, the Volmer step is followed either by the Heyrovsky reaction or the Tafel reaction step for the evolution of molecular hydrogen depending on the experimental reaction conditions. When the two adsorbed hydrogen atoms followed by one electron are combined at the electrode surface, then it follows the Tafel reaction step, and when H_2 gas is generated from the coupling of one adsorbed hydrogen atom with one proton by up taking one electron, then the mechanistic pathway is known as the Heyrovsky step.[116,127] All the reaction steps in both acidic and alkaline conditions are illustrated in eqn (5)–(10) as follows:

Acidic medium: $2H_{(aq)}^{+} + 2e^- \rightarrow H_{2(g)}$

$$H_3O^+ + e^- \rightarrow H_{ads} + H_2O \text{ (Volmer)} \quad (5)$$

$$2H_{ads} \rightarrow H_2 \text{ (Tafel)} \quad (6)$$

$$H_3O^+ + H_{ads} + e^- \rightarrow H_2 + H_2O \text{ (Heyrovsky)} \quad (7)$$

Alkaline Medium: $2H_2O + 2e^- \rightarrow H_{2(g)} + 2OH_{(aq)}^-$

$$2H_2O + 2e^- \rightarrow 2H_{ads} + 2OH^- \text{(Volmer)} \quad (8)$$

$$2H_{ads} \rightarrow H_2 \text{ (Tafel)} \quad (9)$$

$$H_{ads} + H_2O + e^- \rightarrow H_2 + OH^- \text{(Heyrovsky)} \quad (10)$$

Moreover, the overall HER reaction mechanism greatly depends on the Gibb's free energy of the adsorbed hydrogen atom (ΔG_{H^*}) due to the involvement of H_{ads} in both the Volmer–Heyrovsky and Volmer–Tafel steps, and hence the rate-limiting step is the adsorption of a hydrogen atom.[127] According to DFT analysis, it has been deduced that the weak and strong adsorption process of H atoms on the active sites of the surface of the electrode greatly affects the effective adsorption (Volmer step) of a hydrogen atom and desorption (Tafel or Heyrovsky steps) of the hydrogen molecule, respectively. Thus, the HER process mainly prefers a catalyst possessing a moderate hydrogen binding capacity with a ΔG_{H^*} value close to zero. By using DFT calculation, the Gibb's free energy[36,73,130] for the chemisorbed hydrogen can be calculated by combining the binding energy with the thermal calculations using eqn (11).

$$\Delta G_{H*} = \Delta E_{H*} + \Delta E_{ZPE} - T\Delta S_H \quad (11)$$

where ΔE_{H^*} is the differential chemisorption energy/binding energy of hydrogen, and ΔE_{ZPE} and ΔS_H are the difference in zero-point energy and difference in entropy between the adsorbed state and the gas phase, respectively.

The volcano plot, as shown in Fig. 8, predicts the ΔG_{H^*} of some metals together with MoS_2, where it can be found that MoS_2 has similar properties to the well-known Pt noble metal.[129,131] Hence, in recent decades, the low-cost MoS_2 has opened an exciting area of research for the HER. Studies revealed that bulk MoS_2 with an inert basal plane has very poor catalytic activity, which is attributed to its limited active sites and low conductivity. In the study by Peng *et al.*, the ΔG_{H^*} on 2H-MoS_2 was calculated to be 2.18 eV, which is a slight deviation from its optimal value, *i.e.*, ΔG_{H^*} = 0,

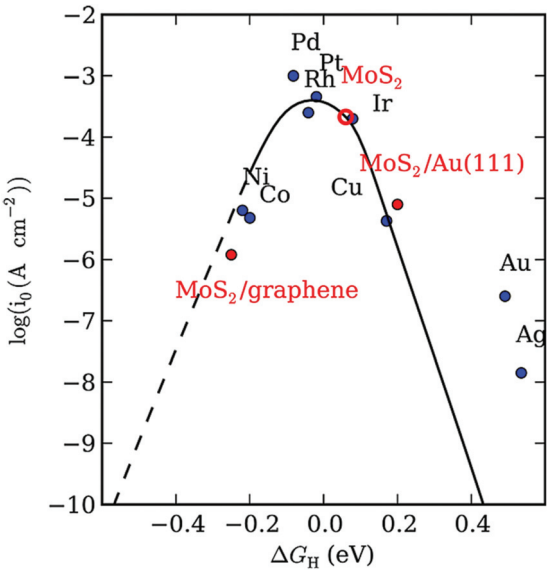

Fig. 8 Volcano plot of various elements with respect to ΔG_{H^*}. Reproduce from ref. 129.

suggesting that the basal plane of bulk MoS_2 is slightly inactive towards the HER.[130] In contrast, single and few-layer 2D MoS_2 with abundant unsaturated S active sites exhibit superior electrocatalytic activity.

The hydrogen coverage (ratio of hydrogen to sulfur atoms) on the top surface of the S-layers of MoS_2 was found to be 1/16. Moreover, the ΔE_{H^*} of the H-atom on the surface of MoS_2 can be defined by eqn (12).

$$\Delta E_{H^*} = E(MoS_2 + H) - E(MoS_2) - \frac{1}{2}EH_2 \quad (12)$$

where $E(MoS_2 + H)$, $E(MoS_2)$ and EH_2 represent the total energy corresponding to MoS_2 with one adsorbed H-atom on its surface, pure MoS_2 and molecular gaseous hydrogen, respectively.[130]

In 2005, Hinnemann and co-workers performed seminal work on MoS_2 towards the HER and reported that the edge of Mo $(10\bar{1}0)$ in MoS_2 is very active for the HER due to its low ΔG_{H^*} value. DFT studies predicted that the binding energy towards H^+ for MoS_2 is +0.08 eV, which is close to that of noble metals such as Pt, at only its edge site. However, its catalytic activity is somehow limited given that the basal plane being relatively inert because it is less conducting although the exposed S edges are the active sites for electron transfer.[132] Specifically, the defected S-edges play an important role in the HER for MoS_2. Typically, the HER activity of MoS_2 mainly depends on its size, edge active sites and number of layers. Thus, it is necessary to engineering MoS_2 with efficiently exposed unsaturated S-sites to obtain electrocatalysts with high HER activity.

Interestingly, Kong and his group introduced more freshly exposed active sites on 2D MoS_2 by engineering nanosized MoS_2.[133] The additional active sites are beneficial towards the intermediate adsorption of H, dramatically boosting the HER performance of 2D-MoS_2 in both acidic and alkaline electrolytic solution. As illustrated in Fig. 9a–d, by employing a simple annealing method, the old molybdenum and sulfur atoms (marked area) present in 2D-MoS_2 underwent a vaporization treatment and were replaced with fresh inner active edges with no alteration in the 2D structure of MoS_2. Consequently, the new 2D-MoS_2 possessed a greater density of under-coordinated S sites, exhibiting an enhanced ECSA and mass-normalized activity together with superior durability, and thus significantly improved HER activity. Upon heat treatment, the current density of the engineered 2D-MoS_2 reached up to 440 mA cm^{-2} at a more positive onset potential compared that required for pristine MoS_2. Besides engineering the edges of MoS_2 through annealing treatment, designing defect-rich MoS_2 through hydrothermal treatment on a substrate is another strategy for establishing highly exposed edge sites. Xie *et al.* constructed defect-engineered MoS_2 catalysts with a controllable thickness, in which ultrathin nanosheets of MoS_2 were vertically aligned to construct a nanowall structure.[134] This MoS_2 nanowall catalyst exhibited a high current density of 310 mA cm^{-2} at η = 300 mV with a low onset over potential of 85 mV. Its superior catalytic performance is attributed to its freestanding vertical channels, which are beneficial for ion penetration, and the presence of a rough surface together with highly exposed active edges. Nevertheless, it is still a challenge to design 2D-MoS_2 with rational and controllable active sites. Accordingly, various strategies such as surface modification, morphological variation, phase and structure control, and fabrication of hybrid materials have been employed to increase the intrinsic activity and electrical conductivity of MoS_2, thus increasing its active sites. Among

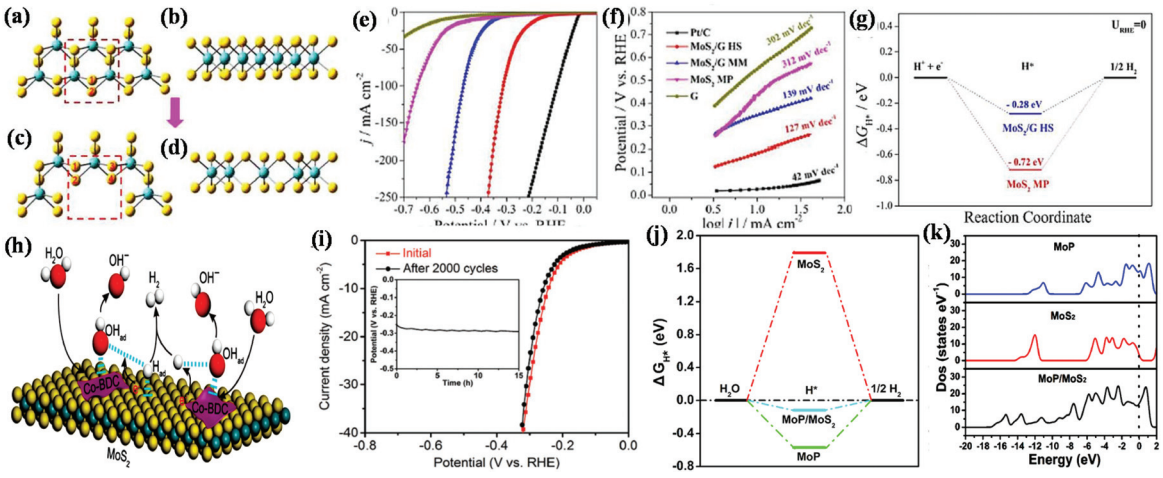

Fig. 9 Structural representation of the edge of pristine MoS_2 nanosheets in (a) top and (b) side views, and structural model of annealed MoS_2 nanosheets in (c) top and (d) side views (Mo and S atoms are represented by blue and yellow balls, respectively). Reproduced with permission.[133] (e) Polarization graph and (f) corresponding Tafel slope of various catalysts together with commercial Pt/C electrode in 1.0 M KOH and (g) hydrogen adsorption free energy plot for neat MoS_2 MP and MoS_2/GHS. Reproduced with permission.[73] (h) Illustration of the catalysis mechanistic pathway for alkaline-mediated HER over Co-BDC/MoS_2 hybrid, (i) polarization curves and chronopotentiometric response (inset) of Co-BDC/MoS_2. Reproduced with permission.[134] (j) Free-energy diagram for the HER and (k) calculated total electronic density of states for MoP, MoS_2 and MoP/MoS_2 heterostructures. Reproduced with permission.[106]

the various achievements, here we only focus on the use of hybrid materials through hierarchical structures based on 2D/2D heterostructures. To date, a large number of HER studies has been reported on 2D MoS_2-based 2D/2D heterostructures and few these studies of are detailed here.

Yu and co-workers established an MoS_2/graphene 2D/2D hetero-layered electrocatalyst towards electrocatalytic HER using both acidic (0.5 M H_2SO_4) and alkaline (1.0 M KOH) electrolytic solution and observed better HER activity in the former.[73] According to the LSV data, it was deduced that a current density of 10 mA is achieved for the MoS_2/graphene heterostructure at an overpotential of only 180 mV in acidic condition and 183 mV in alkaline solution (Fig. 9e), which is much lower than that obtained for neat MoS_2, *i.e.*, overpotential of 383 mV in acidic solution and 436 mV in alkaline solution, respectively. Furthermore, the catalytic performance toward the HER was evaluated through the Tafel slope, which was found to be 79 mV dec^{-1} and 127 mV dec^{-1} for the MoS_2/graphene heterostructure in acidic and alkaline condition (Fig. 9f), and the corresponding Tafel slope value obtained for the neat MoS_2 was about at 219 mV dec^{-1} and 312 mV dec^{-1}, respectively. The superior HER performance of 2D/2D MoS_2/G HS was due to the formation of an intimate face-to-face contact through the alternating layer-by-layer arrangement between 2D-MoS_2 nanosheets and 2D-graphene, which led to more unsaturated atomic edge active sites contacting with the electrolyte and abundant defects between the 2D/2D interface of MoS_2 and graphene. This layer-by-layer arrangement also has a great influence on the electronic state, which favoured the transfer and separation of charges, thus improving the electronic conductivity at the coupled interface. The increase in the number of edge active sites arose from the expanded interplanar distance (1.104 nm) for MoS_2/graphene compared to that of MoS_2 (0.615 nm), which is beneficial for the adsorption and desorption of hydrogen at the electrode electrolyte interface. The experimental study revealed that the 2D/2D MoS_2/graphene HS exhibited superior wettability upon exposure to the electrolyte, which is beneficial for the availability and participation of more active sites in the HER. The smaller contact angle between MoS_2 and graphene in the 2D/2D heterostructure than MoS_2 improved the electronic conductivity at the coupled interface, facilitating the easy transfer and separation of charges at the interface. The high HER performance was also predicted by DFT studies through the three-state diagram (Fig. 9g) for the non-expanded pristine MoS_2 and interlayer-expanded 2D/2D MoS_2/G heterostructures. According to DFT, the ΔG_{H^*} (a powerful parameter for evaluating the adsorption and desorption process) was −0.72 eV for MoS_2 and −0.28 eV for the 2D/2D heterostructure, where the lower potential suggests a lower energy barrier for the fast release and adsorption of hydrogen in the heterostructure, thus improving the rate of the HER.

Inspired by some theories, Zhu and co-workers introduced a 2D-MOF (Co-BDC)/MoS_2 interface for alkaline HER (1 M KOH solution), in which Co-BDC with the optimum binding strength to H_2O and hydroxyl promoted the sluggish water dissociation rate, while MoS_2 enhanced the production and adsorption of hydrogen atoms at the hybrid interface.[135] Importantly, the introduction of Co-BDC (acts as an electron donor) in MoS_2 not only improved the alkaline HER, but also induced a partial phase transfer from 2H to 1T, which lowered the additional energy barrier. Fig. 9h illustrates the overall mechanism for the alkaline HER, which proceeds through the adsorption of hydroxyl, H_2O and H* followed by the dissociation and desorption of H_2O and H_2 molecules, respectively, on the 2D-MOF (Co-BDC)/MoS_2 hybrid nanosheets. The aforementioned electrocatalyst achieved an excellent current density at a very low overpotential. In addition, the long-term durability of the 2D-MOF (Co-BDC)/MoS_2 hybrid was assessed to verify its stability in alkaline solution. Both the cyclic voltammetry and chronoamperometry curves (Fig. 9i) substantiating the excellent stability of the Co-BDC/$MoS_2$2D/2D hybrid nanosheet sample, even after 2000 cycles.

However, in some cases, the HER process is performed in neutral medium to avoid the problems arising in formidable strong acidic and alkaline environments, which also mitigates the environmental-related pollution. Wu *et al.* developed a 2D/2D MoP/MoS_2 heterostructure that fulfils all the requirements needed for the HER process in a neutral environment, *i.e.*, it possesses good conductivity for electron transfer, which is beneficial to decrease the Ohm resistance, plentiful active sites on the heterointerface present between 2D-MoP and 2D-MoS_2 for H_2O activation, and a porous environment on the surface for easy mass transfer, thus weakening the diffusion resistance.[106] The neutral medium was balanced using 0.5 M H_2SO_4 with 1 M phosphate buffered solution and 1 M KOH. The MoP/MoS_2 heterostructure exhibited an impressive current density at a low overpotential in neutral medium, which was much higher than that obtained for the bare MoS_2 and for the reaction occurring in acidic and basic conditions. Furthermore, the MoP/MoS_2 heterostructure also exhibited a good reaction kinetic mechanism with a low Tafel slope value (48 mV dec^{-1}), which follows the Volmer–Heyrovsky reaction pathway. Considering that the neutral medium is governed through the adsorption of H_2O molecules on the surface of the catalyst, the relative free energy of the hydrogen atom and H_2O molecule was evaluated through DFT calculations, as shown in Fig. 9j. The calculated ΔG_{H^*} for hydrogen adsorption indicates that the MoP/MoS_2 2D/2D heterostructure (−0.12 eV) is more favourable for the HER than bare MoS_2 (1.79 eV). Furthermore, the higher H_2O adsorption energy obtained for MoP/MoS_2 (−1.38 eV) than its neat counterpart suggests that H_2O can be easily adsorbed on the catalyst surface and is beneficial due to 2D/2D heterostructure. Furthermore, according to the density of state near the Fermi level, as shown in Fig. 9k, the fast electron transport in the HER process for MoS_2/MoP was evaluated. Conversely, Liang *et al.* demonstrated that MoS_2/black phosphorous exhibited superior activity in both acidic and basic medium.[136]

4.1.2 Photocatalytic H_2 evolution. Overall water splitting under light illumination is a redox reaction and is mainly divided into two key reactions, which are water oxidation and

water reduction [eqn (13)–(16)] and have been extensively considered since the pioneering work by Fujishima and Honda.

$$\text{Photocatalyst} \xrightarrow{h\vartheta} e^- + h^+ \quad (13)$$

$$\text{Reduction}: \ 2H^+ + 2e^- \rightarrow H_2 \quad (14)$$

$$\text{Oxidation}: \ H_2O + 2h^+ \rightarrow 2H^+ + \frac{1}{2}O_2 \quad (15)$$

$$\text{Overall}: \ H_2O \rightarrow H_2 + \frac{1}{2}O_2 \quad (16)$$

Generally, for the production of hydrogen and oxygen, the photocatalytic system mainly requires efficient photocatalysts and a light supply, which can be either a visible or UV-visible source. Under the action of photons, photogenerated charge carriers are generated and transferred to their respective band edge, *i.e.*, electron jumps from the VB to CB edge, leaving a hole in the VB position. The electron in the CB of the photocatalyst is responsible for the reduction of water to produce hydrogen gas, while the hole in the VB facilitates the water oxidation reaction. This mechanism will happen when the CB position is located at a potential that is more negative than the potential required for the reduction of water, *i.e.*, H^+/H_2 = 0 V *vs.* NHE at pH = 0 and −0.41 V *vs.* NHE at pH = 7, whereas the top level of the VB must be more positive than the redox potential of H_2O/O_2, *i.e.*, 1.23 V at pH = 0 and 0.82 at pH = 7. In addition, the band gap must be higher than 1.5 V and not exceed 3.2 V.[3,5,6] However, the utilization of noble metals or alloys is hindered by their high cost. Therefore, currently, it is urgent for researchers to develop competitive alternatives to noble metals. Despite the numerous photocatalytic materials, the unique candidate 2D-MoS_2 plays an important role not only as a co-catalyst but also an excellent visible-light semiconductor with high hydrogen evolution activity due to its high surface to volume ratio, low cost, high catalytic activity, good stability and abundant active sites.[45,46,137]

The studies in the literature revealed that generally pure MoS_2 as a photocatalyst exhibits no or negligible hydrogen evolution activity under visible light illumination. However, the photocatalytic hydrogen evolution activity of 2D-MoS_2 is regulated by the number of layers of MoS_2. With a decrease in the number of layers, the photocatalytic H_2 evolution activity increases, which is maximum for a single layer of MoS_2. This layer-dependent activity mainly originates from the exposed edges of MoS_2 containing a large number of unsaturated dangling sulphur atoms (active sites for hydrogen generation), which bind the H^+ ion very strongly.[32] In addition, the band gap structure of 2D-MoS_2 also plays a role in its photocatalytic H_2 evolution performance. The wide band gap resulting from the quantum confinement effect of MoS_2 (1.8–1.9 eV) and its low conduction band (CB) potential (0 to −0.12 eV) satisfy the conditions for the water reduction reaction (0 eV, at pH = 0 *vs.* RHE). To date, numerous works have been reported regarding the water reduction reaction using neat ultrathin MoS_2. For example, Peng *et al.* fabricated a single-layer multiphasic MoS_2 nanosheet keeping the optimum ratio between the 2H semiconducting phase and quasi metallic 1T' phase and employed it directly as an efficient hydrogen evolution photocatalyst.[130] According to the DFT study, they revealed that the in phase heterojunction between the 2H and 1T' phase is responsible efficient charge transfer and separation, which are essential for photoactivity. Moreover, the suitable band gap of the 2H semiconducting phase is responsible for light absorption and charge generation, and the basal and edge sites at the 1T' phase are the most favourable for hydrogen evolution. Further, considering the limited H_2 production by pure MoS_2, Wan and co-workers employed a novel approach for the synthesis of few-layer MoS_2 nanosheets from an MoS_2 stack with high yield through the facile solvothermal method followed by liquid exfoliation treatment.[138] This synthetic procedure is beneficial for electronic and structural modification, which provides a large surface area together with additional exposed active edge sites, promoting the separation and transformation of photogenerated charge pairs to a greater extent. The solid monodispersed few-layer MoS_2 nanosheets exhibited an excellent photocatalytic hydrogen evolution performance of 1241.3 μmol g^{-1} h^{-1}. As described in Fig. 10a and b, the high photocatalytic effect is mainly attributed to the (i) formation of isolated nanosheets with a high surface area and exposed active sites for H^+ adsorption and hydrogen evolution reaction, (ii) creation of lattice cracks on the inert basal plane due to the ultrasonication effect, followed by heat treatment, which added extra active sites, (iii) decrease in the number of layers of MoS_2 nanosheets, which is beneficial for efficient charge separation and migration together with the creation of a direct band gap, (iv) structure change in which the MoS_2 nanosheets possess a more negative CB potential for superior HER activity. Furthermore, the solid nature together with excellent stability and dispersibility in solution make the MoS_2 nanosheets a great potential candidate for application in many fields. In addition, the as-obtained MoS_2 nanosheets exhibited enhanced photoelectrochemical properties such as high transient photocurrent density, suggesting its superior photoelectric response, and the impedance measurement showed they possess good conductivity for promoting the transfer of photoinduced charge pairs in the photocatalytic reaction. Another few-layer MoS_2 material towards photocatalytic hydrogen evolution was reported by Wang *et al.*[139] They prepared few-layer (1–4 layer) MoS_2 through a facile liquid-phase exfoliation strategy using a salt and organic electrolyte solution. It was found that the sodium tartrate-treated MoS_2 exhibited a superior photocatalytic hydrogen evolution rate, *i.e.*, 0.5 mmol g^{-1} h^{-1} compared to that of bulk MoS_2.

Besides few-layer neat MoS_2, the compositing of ultrathin neat MoS_2 as a photocatalyst and co-catalyst with various UV- and visible-driven materials such as metal oxides, metal sulphides and carbonaceous materials has been studied recently. Here, we summarize a few recent reports on 2D/2D MoS_2-based heterostructures towards photocatalytic hydrogen evolution. For example, Yuan *et al.* developed a 2D/2D black phosphorous/MoS_2 heterostructure photocatalyst towards hydrogen evolution under visible light irradiation.[103] The 2D/2D BP/

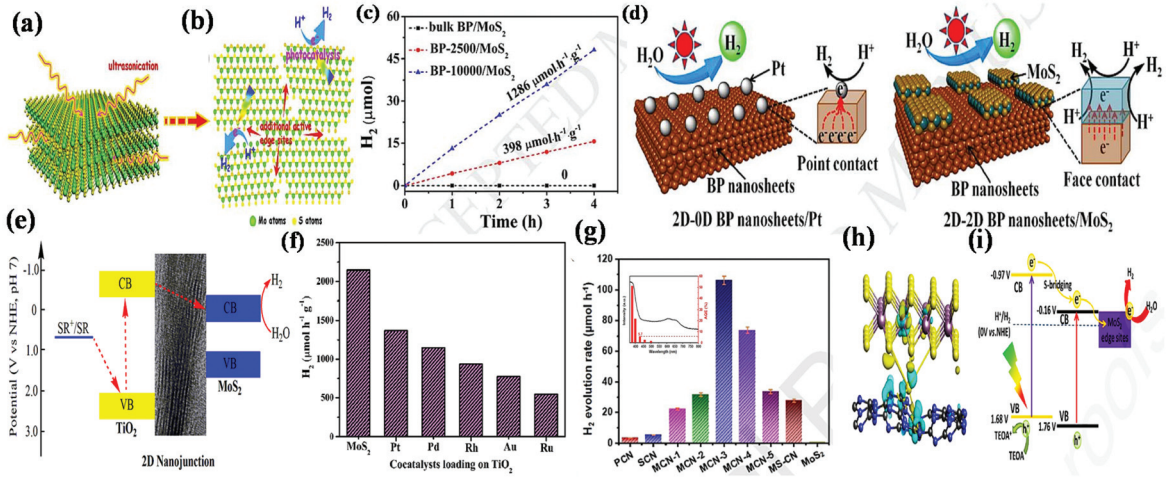

Fig. 10 (a) Schematic illustration of the liquid exfoliation strategy for MoS_2 by ultrasonication treatment and (b) disordered structure of few-layer MoS_2 nanosheets. Reproduced with permission.[138] (c) Production of H_2 through the photoreduction of various BP/MoS_2 samples and (d) schematic illustration of the charge transfer process in 2D–0D BP-10000/Pt and 2D–2D BP-10000/MoS_2 photocatalyst. Reproduced with permission.[103] (e) Energy diagram illustration of the photocatalytic mechanism over the 2D–2D MoS_2/TiO_2 photocatalyst and (f) H_2 production yield on 0.50 wt% of different co-catalyst-loaded TiO_2. Reproduced with permission.[140] (g) Comparison of H_2 production rates of MS-CN, SCN and MCN samples, [inset figure: representation of AQE for H_2 evolution], (h) side-view illustration of MCN heterostructure with differential charge density (net electron accumulation and depletion are depicted by the yellow and navy regions, respectively) and (i) proposed mechanistic pathway diagram for photocatalytic H_2 production reaction under visible light illumination. Reproduced with permission.[110]

MoS_2 heterostructure exhibited a high current density (3.14 mA cm^{-2}) together with high H_2 evolution efficiency (1286 μmol h^{-1} g^{-1}), as shown in Fig. 10c, and an apparent quantum yield of 1.2% in comparison with MoS_2 nanosheets and bare BP sheets. In this study, the high photocatalytic activity is due to the unique 2D/2D interface (face contact) and was compared to a typical 0D/2D structure (point contact) by taking Pt as a 0D cocatalyst. According to the point of charge migration and charge pair separation, as given in Fig. 10d, it is obvious that the smart 2D/2D photocatalyst exhibits a much great contact nanointerface than 0D/2D, which provides a longer diffusion path length for the charge transfer and separation of photogenerated charge pairs, thus resulting in higher photocatalytic H_2 evolution. Moreover, the driving force is another crucial factor in modulating the photocatalytic H_2 production performance, and here the combination of quantum-sized BP (10 000 rpm) with MoS_2 provides a greater driving force, which lowers the CB to a more negative potential to achieve a high photocatalytic hydrogen evolution rate. In addition, Yuan *et al.* also applied a similar type of phenomenon to a 2D/2D binary (MoS_2/CdS, MoS_2/g-C_3N_4) system and 2D/2D/2D ternary system (g-C_3N_4/graphene/MoS_2) through face-to-face contact and observed excellent photocatalytic activity compared to other photocatalysts.[141–143] Compared to the 2D/2D MoS_2-based heterostructure, we employ a 2D MoS_2-based 2D/OD heterostructure to gain more insight into the structure–activity relationship. In this case, Chai *et al.* monitored the photocatalytic hydrogen evolution experiment using an MoS_2/CdS composite in which MoS_2 nanosheets were uniformly distributed on CdS nanospheres.[144] The as-fabricated composite with only 5% MoS_2 exhibited a hydrogen evolution rate of about 372 μmol h^{-1} with an apparent quantum yield of 7.31% under 300 W Xenon lamp illumination. The photocatalytic activity is attributed to the easy migration and separation of photogenerated charge carriers in the composite photocatalysts. Moreover, it should be noted that in comparison to binary 2D heterostructures, ternary 2D heterostructures provide a larger and more intimate 2D junction, which can effectively enhance the charge transfer rate, resulting in high photocatalytic activity.

Yuan *et al.* employed facile hydrothermal method for developing an MoS_2/TiO_2 (001) 2D/2D nanosheet heterojunction.[140] The constructed typical 2D/2D heterojunction possessed a large and intimate interface between MoS_2 and TiO_2 and also boosted the separation and transportation efficiency of photogenerated charge pairs, which is attributed to the synergistic effect of MoS_2 and TiO_2. The energy diagram for the charge transfer process between MoS_2 and TiO_2 is illustrated in Fig. 10e. The 2D/2D interfacial structure provides a large contact area with abundant exposed active sites, which accelerate the rate of hydrogen evolution, achieving 2145 μmol h^{-1} g^{-1}, a value 36.4-fold that of TiO_2 nanosheets with an apparent quantum yield of 6.4% (360 nm). According to the data shown in Fig. 10f, it is also obvious that the MoS_2/TiO_2 (001) 2D/2D heterojunction is more active towards H_2 production than noble metals such as Pt, Pd, Au, Rh and Ru-loaded TiO_2 (001) nanosheets. Hence, it was proven that MoS_2 acts as a better co-catalyst in 2D–2D systems than noble metals for hydrogen evolution activity.

Recently Dong *et al.* developed an S-doped g-C_3N_4/MoS_2 2D/2D face-to-face heterojunction photocatalyst and observed its superior photocatalytic activity.[110] The hydrogen evolution per-

formance was investigated under visible light irradiation together with TEOA as a sacrificial agent. As shown in Fig. 10, the 2D/2D g-C_3N_4/MoS_2 heterojunction achieved a high H_2 production rate, *i.e.*, 2120 μmol h^{-1} g^{-1} (Fig. 10g) together with a notable quantum yield of 5.7% (inset image) The high photocatalytic performance is attributed to the fast transportation of photogenerated charge carriers and efficient charge separation through the interface contact produced due to the face-to-face heterojunction between the two 2D components, which was also supported by the high photocurrent response. Moreover, first principle calculations of the differential charge density have become a crucial parameter to get an in-depth understanding about the charge separation efficiency based on photocatalytic activity. In this regard, Fig. 10h shows the charge redistribution at the face-to-face interface between 2D-S-g-C_3N_4 and 2D-MoS_2, which clearly represents the accumulation and depletion of electrons in the MoS_2 region, while the holes remain in the SCN region. The high efficiency is mainly due to the presence of S atoms, as seen in polarized field in the figure, facilitating the charge distribution at the interface region, which not only improves the light absorption capacity, but also allows efficient charge transfer. The possible H_2 evolution mechanism proposed in Fig. 10i together with the energy band structure shows that the rapid channelization of photoexcited electron occurs from SCN to MoS_2 through the face-to-face interface and the final H_2 gas is evolved over the unsaturated S atoms at the MoS_2 exposed edges. Thus, the above studies deduced that 2D/2D engineering between two 2D materials through face-to-face contact is one of the feasible ways to achieve charge separation for superior photocatalytic hydrogen production. The face-to-face 2D/2D interface structure for photocatalytic application has been widely employed by many researchers, and prior to this, more insight was gained by comparison with point contact.

4.2 Nitrogen reduction reaction

Similar to hydrogen, ammonia is an expectant "green fuel" candidate towards environmental sustainability, which is required to minimize the current issue based on the scarcity of fossil fuels.[145,146] Due to its low liquefying pressure and high hydrogen density, ammonia also plays a vital role as an easy transportable promising carbon-neutral energy carrier with zero-balance greenhouse gases such as CO_2 emission.[147,148] However, the conversion of NH_3 from N_2 through the N_2 fixation reaction *via* natural (nitrogenase enzymatic process) and artificial (*i.e.*, industrialized Haber–Bosch process) processes is a practical problem nowadays due to the involvement of series of biochemical steps, which delay the reaction rate, increase the cost-effective, and reduce the safety.[7,149] Thus, now it is of great significance to develop cost-effective, green and sustainable techniques for the production of NH_3. Although a mimicking methodology has been investigated, *i.e.*, traditional heterogeneous catalysis, electrocatalysis and photocatalysis-based NRR involving stable and noble-metal free catalysts at room temperature and atmospheric pressure is becoming a highly desirable and profitable artificial technique towards the reduction of N_2 to NH_3.[7,75,146,148,150–153] For instance, the electrochemical NRR process involves the use of electrolytic cells together with different electrodes and electrolytes, which are powered by solar cells, wind turbines, *etc.*, whereas in terms of photocatalytic NRR, the reaction is directly governed by sunlight or visible light. Although Mo-based catalysts exhibit a great performance towards the NRR as both photocatalytically and electrocatalytically active, to date, only a few studies have been reported, which are summarized in the following section. In the case of the photocatalytic and electrocatalytic NRR processes, both follow a number of mechanistic pathways, which can be determined through DFT analysis, to give the product.

To design a potential catalyst with a low limiting potential (U_L) towards superior photo/electrocatalytic N_2 reduction, theoretical calculations based on machine learning are considered. According to DFT calculations, it has been predicted that the NRR performance is directly correlated with the five adsorbates (H, N_2, N_2H, NH, and NH_2), whose binding energies are over 8 eV.[154] The limiting potential that determines the minimum applied voltage to the exergonic NRR process follows one of two protonation steps, *i.e.*, $*N_2 \rightarrow *N_2H$ and $*NH \rightarrow *NH_2$. Based on the DFT-computed free energy study, the U_L can be represented as follows:

$$U_L = \frac{\Delta G_{N_2H} - \Delta G_{N_2}}{e} \text{ or } U_L = \frac{\Delta G_{NH_2} - \Delta G_{NH}}{e}$$

It has been determined from machine learning work that the catalytic surface, which fulfils the 4 to 6 d orbital occupation, can potentially lower the U_L for the NRR reaction.[154]

4.2.1 Electrocatalytic NRR. In electrochemical NRR, the first step is the generation of an H^+ ion at the electrode/electrolyte interface, which then migrates through the electrolytic solution towards the catalytic surface, and finally, on the surface of catalytic site present on the cathode, the adsorbed N_2 reacts with H^+ and is converted to NH_3 with the capture of an electron. Thus, the crucial step in the electrocatalytic NRR is the binding capacity of N to the catalytic surface, which indicates that the working electrode (catalyst) should have an optimized nitrogen binding capacity. The NRR follows three mechanistic pathways to give product. The mechanistic pathway is governed by the proton-coupled electron (H^+/e^-) transfer process, which converts N_2 to NH_3 under ambient reaction conditions. In detail, in the first step, the N_2 molecule is adsorbed on the surface of the catalyst ($*N{\equiv}N$) and then captures one proton (H^+) and one electron from the catalyst surface to give an adsorbed intermediate chemical species, *i.e.*, $*N{=}NH$, which is converted to the final NH_3 product following the transfer of H^+/e^- pairs through the associative mechanism followed by the formation of different intermediate by-products such as N_2H_4 and N_2H_2.[146,155,156] From a theoretical point of view, it has been elucidated that some metals such as Fe, Mo, Ru, Rh, Pt and Ir exhibit relatively optimized nitrogen binding capacity.[155] Kim *et al.* investigated the distal mechanistic pathway through machine learning over several transition metals and found that the Mo

surface with (110) plane exhibits the lowest U_L value among them, *i.e.* about −0.92 V. Together with the low limiting potential over the Mo (110) surface, the binding energy difference, which estimates the adsorption competition of N_2 and H components, is also more negative, *i.e.*, −0.18 eV, which suggests a higher faradaic efficiency.[154]

Based on the demands regarding optimized N_2 binding catalysts, Mo-based materials have been widely investigated as NRR electrocatalysts. Among them, 2D-MoS_2 acts as an ideal catalyst for the NRR. Similar to the HER on MoS_2, the edge sites of MoS_2 are also more preferable towards the electrocatalytic NRR under ambient conditions. It has been considered that the elements Mo and S, which are the key elements of the nitrogenase-mediated reaction, play a vital role in the nitrogen fixation reaction. Accordingly, proof-of-concept regarding electrocatalytic NRR over MoS_2 was investigated on accordance with DFT calculations, which mapped out the electronic environment of MoS_2 through various energy profile diagramd.[117,157] In this regard, in 2018, Zhang and co-workers reported their study based on the electrocatalytic NRR activity of 2D-MoS_2 from a theoretical and experimental point of view to show whether the edge-site MoS_2 are electrocatalytically active.[117] According to the DFT studies, the isosurface of the deformation charge density of MoS_2 was calculated to be a positively charged environment, *i.e.* $+0.963|e|$, around the edges of the Mo ion, which plays a significant role in the activation and polarization of N_2 molecules. Also, the N_2 molecules are generally activated and polarized at the positively charged centre, and thus based on DFT, they further deduced a free energy profile, as shown in Fig. 11a, from which the potential determining step (PDS) was studied. The PDS explains the reductive protonation of adsorbed N_2 on the Mo edge surface with a lower limiting barrier of about 0.68 eV without applying any external potential, which is much higher in the case of some common metal surfaces, ranging from 1 to 1.5 eV. The relatively low barrier predicted by PDS for the Mo edge suggests the significant elongation of the N–N bond length, *i.e.*, from $*N_2$ (1.129 Å) to *NNH (1.221 Å), as shown in Fig. 11b, which accelerates the NRR. Consequently, the N≡N triple bond is easily weakened by the transformation of the charge from N_2 to positively charged Mo-edge, resulting in N–Mo bond formation. This is clearly illustrated by the deformation charge density of *NNH supplied in Fig. 11c. Fig. 11d shows the NH_3 yield together with the corresponding faradaic efficiencies (FEs) under the application of different potentials. An appreciable NH_3 yield of 8.08×10^{-11} mol s^{-1} cm^{-2} with a faradaic efficiency of 1.17% was achieved. The highest NH_3 yield and faradaic efficiency were achieved at an optimum potential of −0.5 V, after which, the value markedly decreased, suggesting the competence adsorption nature of both hydrogen and nitrogen on the electrode surface. In addition, the MoS_2/CC electrode possessed high stability given that there was no obvious change in NH_3 yield after ten successive recycling tests. This relatively low barrier in terms of PDS on the Mo-edge further strengthens the claim that MoS_2 is a potential catalyst for the NRR. Based on the abovementioned studies, although the MoS_2 edge site is predicted to give an appreciable NH_3 yield, some improvement is still needed regarding NRR selectivity due to its HER competence. Hence, Liu *et al.* prepared an ultrathin S-rich MoS_2 nanosheet through Li intercalation and tested its performance towards the NRR in an acidic environment.[158] The Li ion interacts with the S edge site of MoS_2, which facilitates the adsorption of N_2, and hence enhances the nitrogen reduction. According to the DFT study, it was found that Li–S interaction increases the N_2 adsorption free energy from −0.32 to −0.70 eV and decreases the activation energy barrier of the reaction control

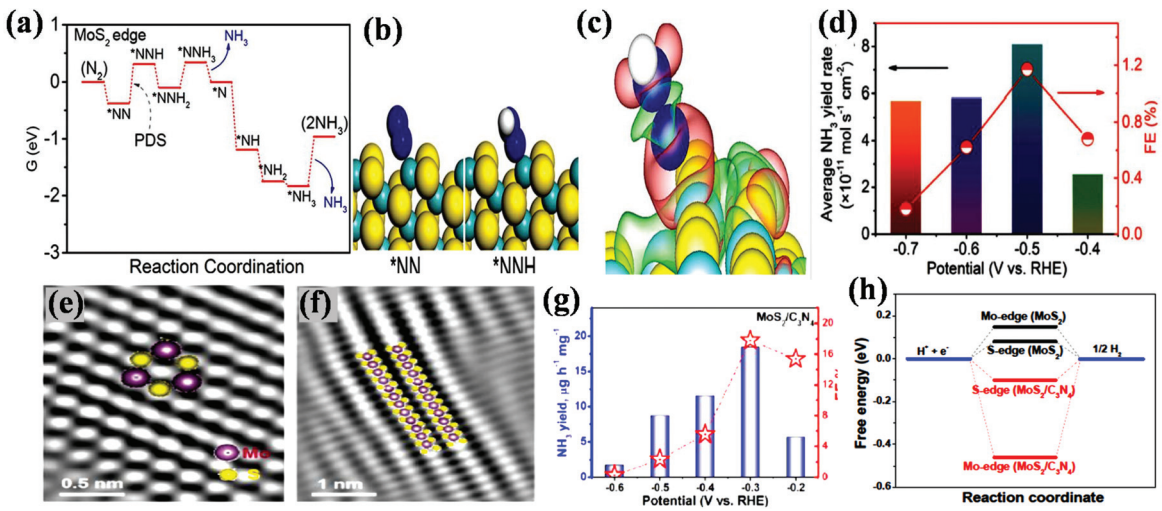

Fig. 11 (a) Free-energy profile diagram at MoS_2 edge site for the NRR, (b) structural representation of the key intermediates of the PDS, (c) deformation charge density diagram of *NNH, and (d) average NH_3 yield and faradaic efficiency graph for MoS_2/CC at different potentials. Reproduced with permission.[117] (e) and (f) IFFT images of MoS_2/C_3N_4, (g) NH_3 concentration and faradaic efficiency plot for MoS_2/C_3N_4 and (h) free energy diagrams of *H (ΔG*H) of MoS_2 and MoS_2/C_3N_4 on Mo-edge and S-edge sites. Reproduced with permission.[159]

step from 0.84 to 0.42 eV, and simultaneously, it also reduces the hydrogen adsorption free energy. The designed catalyst exhibited an NH_3 yield rate of 43.4 μg h^{-1} mg^{-1} with the highest faradaic efficiency of 9.81%, while suppressing the HER yield.

Nevertheless, the electrocatalytic NRR activity of neat MoS_2 nanosheets is still not satisfactory, and hence interfacial engineering *via* 2D/2D MoS_2-based heterostructures is a powerful technique to meet the requirements for the NRR. Chu *et al.* designed a 2D/2D MoS_2/g-C_3N_4 heterostructure for the NRR through a simple *in situ* hydrothermal method.[159] According to the DFT analysis, the effective NRR performance is due to the face-to-face coupling interaction of MoS_2/g-C_3N_4, which facilitates the stimulation of Mo edge sites towards the NRR and protects the NRR-active Mo-edge sites against the competing HER. However, the noise-filtered inverse fast-Fourier transform (IFFT) study, as shown in Fig. 11e and f, for MoS_2/C_3N_4 revealed that over the hexagonal symmetry basal plane of 2D-MoS_2, orderly stacked MoS_2 layers are present together with exposed abundant Mo edge-terminating sites, which are believed to be the NRR active sites. Thus, to prove this hypothesis, the NRR performance over MoS_2/C_3N_4 was evaluated in 0.1 M $LiClO_4$ solution under ambient conditions. The best NH_3 yield and the faradaic efficiency of the given electrocatalyst, as depicted in Fig. 11g, were obtained to be 18.5 μg h^{-1} mg^{-1} and 17.8%, respectively, at only −0.3 V of applied potential. However, beyond the potential of −0.3, the rate of NH_3 together with the faradaic efficiency significantly decreased (*e.g.*, at −0.2 V), which is ascribed to the competing HER on the surface of the electrode. During the course of the reaction, Chu *et al.* also depicted that the MoS_2/C_3N_4 heterostructure electrocatalyst resulted in an excellent ammonia yield with good selectivity towards the NRR compared to neat C_3N_4 and MoS_2 given that no N_2H_4 was detected. The reduction mechanism was thoroughly investigated through a DFT study (distal pathway). The free energy calculation followed by the potential limiting steps of all the intermediates suggested that MoS_2/C_3N_4 exhibits a relatively low energy barrier for the reaction-controlling step, *i.e.*, up to 0.55 eV for $*N_2$ to $*N_2H$, which changes to 0.62 eV for the pathway of $*NNH_2$ to *N. The PDS value for MoS_2/C_3N_4 is much more lower than that of neat MoS_2, which suggests that the face-to-face interfacial contact created between 2D-MoS_2 and 2D-C_3N_4 effectively stimulates the NRR activity by stabilizing $*N_2H$. Furthermore, the protection of the NRR-active Mo-edge sites from the competing HER was also proven through the free energy study, as shown in Fig. 11h. Based on the calculated free energy data, ΔG^*H was 0.08 and 0.15 eV for Mo and S-edge in pristine MoS_2, respectively, whereas it was −0.46 eV for Mo edge and −0.12 eV for S-edge in the MoS_2/C_3N_4 heterostructure. However, the great change in ΔG^*H at the Mo-edge suggests the protection of the Mo-edge rather than the S-edge sites (favourable ΔG^*H), which is unfavourable for the HER, hindering the formation H_2 while allowing the NRR.

In addition, Li *et al.* developed a highly active and durable MoS_2/RGO hybrid towards electrocatalytic NRR and found that it exhibited excellent selectivity for N_2 conversion to NH_3 under ambient conditions.[160] The MoS_2/RGO 2D/2D electrocatalyst achieved a high NH_3 yield, *i.e.*, 24.82 μg h^{-1} mg^{-1}, with the corresponding faradaic efficiency of 4.56% at a potential of −0.45 eV. According to the DFT study, the authors suggested that the N_2 adsorption on MoS_2/RGO is more favourable than that on separate MoS_2, which originated from the enhanced electron transfer. Further the PDS of the electron–proton coupling transferring process of $*NHNH_2$ to $*NH_2NH_2$ with an energy barrier of 0.49 eV suggests the feasible generation of ammonia.

4.2.2 Photocatalytic NRR. The photocatalytic nitrogen fixation strategy is regarded as energy efficient and environmentally benign because the reaction proceeds under ambient conditions, benefiting from clean and renewable resources such as solar energy, and the product is achieved directly from nitrogen and water.[149,155] The photocatalytic NRR process involves three steps as follows: (i) generation of photoexcited charge carriers under light energy irradiation, (ii) separation and migration of charge carriers to the catalytic surface, and (iii) participation of photoexcited electrons and holes in the redox process of NRR modulated by H^+ and electrons. Thus, for an efficient NRR, the CB of the catalyst should lie at a more negative potential than the theoretical reduction potential required for N_2 hydrogenation and the VB should be at a more positive than the water reduction potential value.[7] The photofixation mechanism is not only governed by the suitable heterogeneous catalytic centre, but also a multi-electron reduction process to minimize the thermodynamic barrier, which can also prevent the formation of high energetic intermediates, as already discussed in the electrochemical NRR section. To date, a number of photocatalytic semiconductors such as CeO_2, TiO_2, WO_3, and Bi_2MoO_6 besides MoS_2 have been reported to reduced N_2 to NH_3 under UV and visible light illumination, but the obtained concentration of NH_3 is not satisfactory to meet the practical demand.[152,161–163] MoS_2 plays a vital role in this field and also acts as an electron-rich semiconductor that facilitates the multi-electron reduction reaction essential for the NRR. Reviewing the literature regarding photocatalytic N_2 fixation, it was deduced that a few works have been carried out on the design of MoS_2. According to these works, some examples such as Sun *et al.* in 2017 developed sonicated ultrathin MoS_2 for photocatalytic N_2 reduction to NH_3 under simulated solar light and achieved a concentration of 0.14 mg L^{-1} NH_3 in DI water in 10 h.[50] The production of a high concentration of NH_3 mainly depends on its ultrathin structure, providing a platform to produce more charged excitons, which behave as an electron-rich species (Fig. 12a). Considering that the NRR is regulated by a multi-electron–proton-based pathway, the participation of protons was studied by considering the photocatalytic NRR in an acidic solution with different pH, as shown in Fig. 12b. The result suggests that the ammonia concentration is high (0.83 mg L^{-1}) when the pH of the solution is 3.5, which may be attributed to the production of an excess proton from the acid water environment, and this reduces the kinetic barrier for the N_2 reduction reaction. In addition, to

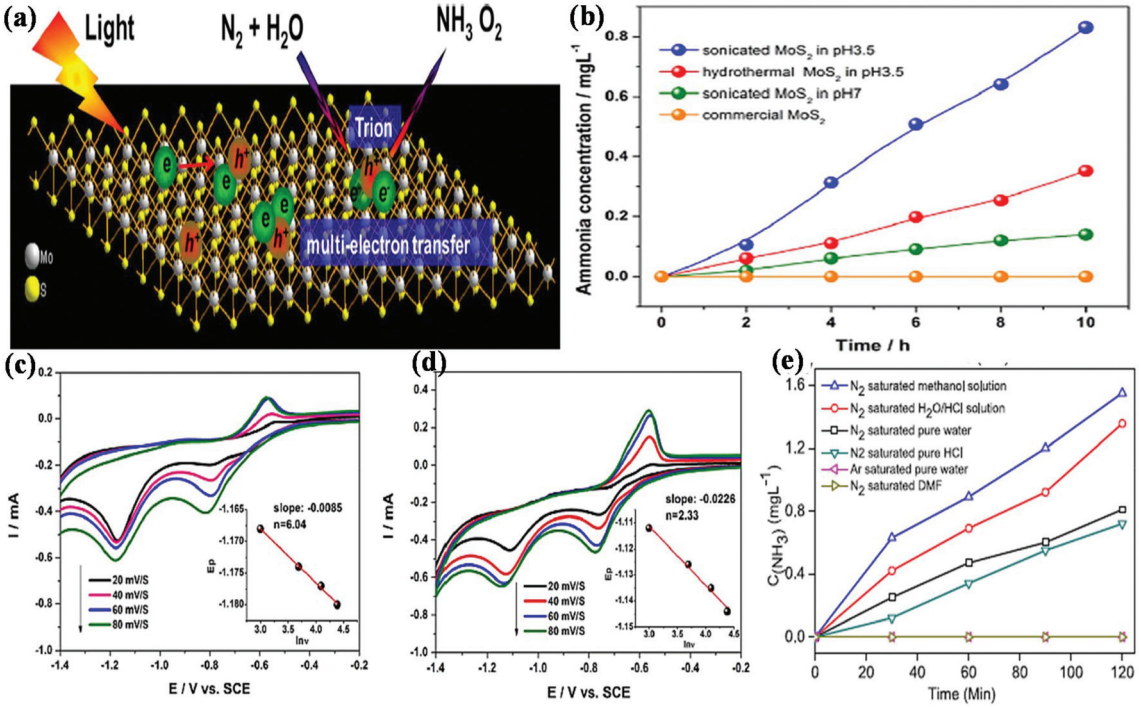

Fig. 12 (a) Schematic representation of multi-electron N_2 photoreduction process and (b) rate of ammonia concentration over various MoS_2 samples mediated by different conditions. Cyclic voltammograms in N_2-saturated 0.5 M Na_2SO_4 (pH = 3.5) at different scan rates for (c) sonicated ultrathin MoS_2 electrode and (d) commercial MoS_2 electrode. Reproduced with permission.[50] (e) Yield of photoreduction of N_2 fixation on 5% MoS_2/$MgIn_2S_4$ heterojunction photocatalyst under various solvent conditions. Reproduced with permission.[90]

verify the multi-electron reduction process, the electron transfer number for the N_2 reduction reaction was calculated according to the Laviron equation. The slope of the curve, as depicted in Fig. 12c and d, suggested a 2.33- and 6.04-electron transfer process for bulk/commercial MoS_2 and ultrathin MoS_2, respectively, which make MoS_2 energetically qualified for the N_2 photoreduction reaction. The electron transfer number of 6.04 is sufficient to decrease the thermodynamic barrier under ambient conditions.

However, the N_2 reduction efficiency obtained for pristine MoS_2 is quite low compared to other photocatalysts, but from an experimental view, it has been seen that after compositing it with other 2D photocatalysts, its N_2 reduction efficiency significantly increases. In this regard, our group designed a 2D/2D MoS_2/$MgIn_2S_4$ heterojunction photocatalyst and tested its activity under visible light irradiation (250 W Hg lamps).[90] The controlled photocatalytic N_2 fixation experiment as illustrated in Fig. 12e, where the as-fabricated sample was tested under different reaction conditions using various scavenging units at the optimum pH. The investigated 2D/2D heterojunction photocatalyst achieved the highest concentration of NH_4^+ (1.54 mg L^{-1}) with 10 vol% methanol–water system compared to that for distilled water (0.81 mg L^{-1}) and DMF (no ammonia) due to the quick oxidation of methanol by h^+, which produces $CO_2{}^{*-}$ to facilitate the reaction easily. In contrast, by regulating the pH of the reaction, it was deduced that under a very high acidic environment (0.1 M HCl), the concentration of NH_3 is quite low (0.72 mg L^{-1}), whereas it increases with an increase in pH. It was observed for the HCl/H_2O system with the optimum pH (pH = 3.6) that the ammonia concentration reached a high value (1.35 mg L^{-1}). However, it was believed that in a highly acidic medium, the HER is dominant over the corresponding NRR, and in a moderate acidic medium, the generation of excess protons reduces the kinetic barrier for the NRR. Moreover, the given 2D/2D heterojunction photocatalyst possessed high selectivity towards the N_2 reduction reaction with a 4.8-electron transfer process given that the peak for the bi-product (N_2H_4) was absent. The 2D/2D MoS_2/$MgIn_2S_4$ photocatalyst achieved an excellent NRR performance and long-term stability was also observed for its photocurrent density. However, the overall photocatalytic performance depends on the 2D/2D combination through petals of the flower (2D-$MgIn_2S_4$) and a sheet (MoS_2), which are attached *via* a face-to-face and face-to-edge fashion and the p–n heterojunction mechanism, favouring efficient charge migration and separation at the interface.

4.3 Carbon dioxide reduction reaction

As already discussed in the previous section, the excessive consumption of fossil fuels greatly increases the atmospheric carbon dioxide (CO_2) level, and hence is regarded as the main culprit responsible for global climate change. The increase in CO_2 level also disturbs the carbon cycle, leading to a severe

greenhouse effect on the Earth's surface.[1,2,4,164,165] Thus, nowadays, the foremost challenge faced by society is to conserve the environment for the future generation in the aspect of depletion of renewable energy sources with a reduction in the CO_2 level in the atmosphere. In this scenario, the key issue is to design novel technologies that can relieve environmental problems by mitigating the CO_2 concentration in the environment together with the production of sustainable energy using a clean and abundant strategies. Thus, to realize this fascinating blueprint, converting CO_2 through the reduction process into renewable fuels together with value-added clean carbon-based nontoxic chemicals such as carbon monoxide (CO), hydrocarbons, alcohols, syngas, and formic acid has emerged as the most compelling pathway to build a sustainable recycling system by fulfilling the global energy demands.[164–167] Nevertheless, CO_2 is a stable, linear and chemically inert molecule bearing a huge energy gap of around 13.7 eV between its LUMO and HOMO, and hence the transformation of CO_2 is a thermodynamically uphill reaction, demanding a significant energy input for the dissociation of the C=O bond, which is around 750 kJ mol^{-1}.

The process of CO_2 reduction involves the adsorption and activation of a CO_2 molecule on the surface of catalyst followed by a number of different reaction steps regulated through a 2, 4, 6, 8, 12 or more electron transfer pathway, which is kinetically very unfavourable.[4] However, the photo/electro reduction of CO_2 using efficient catalysts is becoming an economical and practical approach to solve the associated thermodynamic and kinetic hurdles. It has been concluded that both photocatalytic and electrocatalytic CO_2RR are surface phenomena regulated through both protons and electrons.[165,166]

Besides water splitting, 2D-MoS_2 has also emerged as an excellent candidate for the reduction of CO_2 both photocatalytically and electrocatalytically. The superior catalytic efficiency of MoS_2 in the CO_2 RR has mainly emerged from its Mo and S-terminated edges and low work function value, which promote the efficiency of MoS_2. By observing the periodic strip model, it was reported that in MoS_2 there are two distinct types of edges, *i.e.*, $\bar{1}010$ and $10\bar{1}0$ edges, which are attributed to the S and Mo edges, respectively, and highly active towards the CO_2 reduction reaction.[168] In addition, it has been seen that in 2D-MoS_2, the presence of active Mo-terminated edge sites stabilizes the intermediate products such as CH_xO_y produced during the CO_2 reduction reaction.[168–170]

The CO_2 reduction activity can be analysed *via* the binding energies of the CO_2 reduction intermediates through computational analysis. For the CO_2 reduction reaction, the computational hydrogen electrode model has received much attention to determine the mechanism of catalytic reactions and free energy profiles of the reaction intermediates proceeding through proton–electron (H^+/e^-) pair transfer by considering the effect of the electrode potential value on the reaction free energy.[171,172] In addition, for each elementary step, the theoretical limiting potential (U_L) is necessary, which determines the lowest external potential at which the reaction steps become exergonic together with the theoretical onset potential for the CO_2 reduction reaction and is calculated as follows:

$$U_L = -\frac{\Delta G_{U=0}}{e}$$

where $\Delta G_{U=0}$ represents the change in free energy of the reaction at 0 V *vs.* RHE.

Accordingly, the most negative limiting potential is taken as the onset potential of the reaction. Chan *et al.* reported that product formation by the CO_2 reduction reaction to CO follows the lowest free energy reaction path for MoS_2 compared to other transition metals such as Au. From their study, at a specific surface coverage, MoS_2 with Mo edges and S edges exhibited a U_L value of −0.61 V and −0.15 V, respectively, which are smaller than that for Au (−0.78 V) at 0 V *vs.* RHE.[168]

However, the sluggish reduction potential needed for the conversion of CO_2 into products with low gas adsorption ability limits its stability as a catalyst in its pure form. Additionally, the fast radiative recombination and low gas adsorption also affect the conversion efficiency of neat MoS_2.[173,174] Nevertheless, the practical applicability of MoS_2 towards the CO_2 reduction reaction can be improved by contributing to the role of exposed active sites on edge, defects and the terrace of the MoS_2. The formation of heterostructures with other 2D materials can also be an effective way for the efficient CO_2 reduction reaction. However, to date, there are only a few reports regarding the catalytic activity of MoS_2 as a photocatalyst towards the CO_2RR.

4.3.1 Electrochemical CO_2 reduction. Currently, the CO_2 reduction reaction through electrocatalysis is employed as the most efficient and long-term solution, which is clean, environmentally compatible and cost effective and is termed the electrochemical CO_2 reduction reaction (CO_2RR). For the electrochemical CO_2 RR, electrons are provided by the directly used electrical energy and the reduction abilities of electrons based on the applied voltage.[166] This process starts with the activation of an adsorbed CO_2 molecule upon electric energy treatment *via* the one-electron transfer pathway, producing the $CO_2^{\bullet-}$ intermediate. However, this step proceeds with a negative formal redox potential (−1.9 V *vs.* NHE), and hence is highly unfavourable and emerged as the rate-limiting step for the reduction reaction of CO_2. An alternative strategy to the one-electron process was established with a lower energetic cost to bypass the formation of the $CO_2^{\bullet-}$ intermediate, which is the so-called proton-assisted multiple-electron (H^+/e^-) transfer method, bearing a more positive thermodynamic value (E° = −0.20 V and −0.60 V). The overall CO_2 RR is governed through the formation of two primary reduction products such as CO and formate due to the reduction of CO_2 *via* the protonation of the oxygen atom and C atom of CO_2, respectively. The reduction of CO_2 to value-added hydrocarbon products is the fission and coupling of the C–O and C–C bond, respectively. Based on the number of protons and electrons transferred, the reduction of CO_2 results in different carbon-based products with different redox potentials. eqn (17)–(22) represent the various intermediates and products formed due to

the activation and reduction of CO_2 together with corresponding redox potential values at NHE.[4,166,175,176]

$$CO_2 + e^- \rightarrow CO_2^- \quad E^{\circ}_{Redox} = -1.9\,V \tag{17}$$

$$CO_2 + 2H^+ + 2e^- \rightarrow HCOOH \quad E^{\circ}_{Redox} = -0.61\,V \tag{18}$$

$$CO_2 + 2H^+ + 2e^- \rightarrow CO + H_2O \quad E^{\circ}_{Redox} = -0.53\,V \tag{19}$$

$$CO_2 + 4H^+ + 4e^- \rightarrow HCHO + H_2O \quad E^{\circ}_{Redox} = -0.48\,V \tag{20}$$

$$CO_2 + 6H^+ + 6e^- \rightarrow CH_3OH + H_2O \quad E^{\circ}_{Redox} = -0.38\,V \tag{21}$$

$$CO_2 + 8H^+ + 8e^- \rightarrow CH_4 + 2H_2O \quad E^{\circ}_{Redox} = -0.24\,V \tag{22}$$

In comparison to the traditionally used noble metals, MoS_2 acts as a promising cost-effective substitute for a superior CO_2 electrochemical reduction performance. The high current density and low overpotential associated with the CO_2RR are mainly due to the molybdenum-terminated edges and the catalytic performance is due to the high d-electron density and metallic character of MoS_2.[177]

Lv *et al.* exfoliated bulk MoS_2 into the nanosheet form by ball-milling followed by CVD and observed that the latter showed greater CO_2 reduction activity. The exfoliated few-layer MoS_2 nanosheets reduced CO_2 to CO with a current density of 61 mA cm^{-2} at 1.1 V together with a faradaic efficiency of up to 41.2% at −0.9 V. The lower onset potential of ultrathin MoS_2 (−0.43 V) in comparison to bulk MoS_2 (−0.30 V) indicates a lower overpotential requirement for the reduction over the exfoliated form. They observed that the percentage of 1T-phase in the exfoliated MoS_2 was much larger than its bulk form. Hence, decreasing the thickness of MoS_2 can significantly increase its reduction ability. The mechanism behind the production of CO followed by the desorption of CO* on the surface of MoS_2 is clearly shown in Fig. 13a and b, respectively. According to this figure, it was deduced that the catalytic site of MoS_2 is the highly active Mo atoms on which CO_2 is easily adsorbed after combining with H^+/e^-. Conversely, MoS_2 possessing ΔG = 0.72 eV facilitates the easy desorption of CO* from its surface, resulting in the formation of products.[178] The production of liquid hydrocarbon-containing products such as 1-propanol from CO_2RR regulated through a high proton–electron process, *i.e.*, 18 H^+ and 18 e^-, is kinetically challenging as the formation of two C–C bond is achieved. In addition, experimental studies revealed that during the electrochemical CO_2 RR, water reduction to H_2 evolution dominates over the CO_2 reduction process given that water is present at a higher concentration compared to dissolved CO_2 with a relatively low concentration. Accordingly, Francis and his group derived single-crystal MoS_2, which yielded 1-propanol from CO_2 in an aqueous electrolytic environment. Simultaneously, together with CO_2 reduction, hydrogen was also produced by the reduction of water as the dominant electrolysis product. To gain insight into the selective production of 1-propanol over hydrogen evolution for a single-crystal MoS_2 terrace, Fig. 13c provides the current density value *via* LSV measurement in both a CO_2 environment (CO_2 saturated electrolyte) and N_2 environment (N_2-purged phosphate buffer). The results indi-

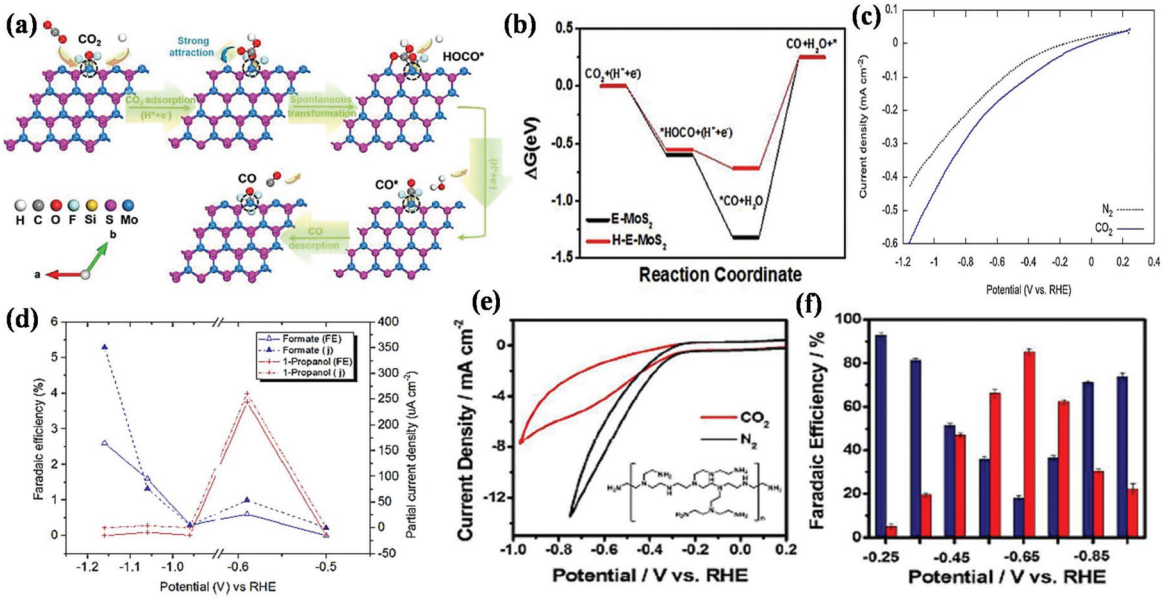

Fig. 13 (a) Schematic illustration of mechanism for the formation of CO over H-E-MoS_2 monolayers (Mo atoms are the catalytic sites represented by a dashed circle) and (b) free energy graph calculation for CO_2 electroreduction to CO. Reproduced with permission.[178] (c) Comparison of LSV data for an MoS_2 single crystal in an N_2 or CO_2 environment and (d) potential-regulated partial current densities (dashed lines) and faradaic efficiencies (solid lines) of the CO_2R products. Reproduced with permission.[179] (e) CV plot over rGO-PEI-MoS_x-modified GCE in CO_2-saturated (red curve) N_2-saturated (black curve), with a scan rate of 50 mV s^{-1} and (f) faradaic efficiency graph of CO (red bars) and H_2 (blue bars). Reproduced with permission.[180]

cate that the cathodic current obtained under the CO_2 atmosphere is larger than that observed under the N_2 atmosphere, which suggests that the reduction of CO_2 is dominant over H_2O reduction on the MoS_2 single-crystal terrace. However, the production of 1-propanol was found to be larger for both the single MoS_2 crystal and MoS_2 thin film with low edge densities rather than that for the thin film containing high edge site densities. Thus, it was concluded that for the reduction of CO_2 to 1-propanol, the MoS_2 surface terrace is responsible not the edges of the thin-film MoS_2. Experimentally, the MoS_2 single crystal terrace displayed a faradaic efficiency of 3.5% at an applied potential of −0.59 V (*vs.* RHE) for the conversion of CO_2 to 1-propanol, and that obtained for the MoS_2 thin film with low edge site densities was around 1%. The experiment also revealed that together with 1-propanol as the major product, other minor products such as formate, ethylene glycol, and t-butanol are produced. The faradaic efficiency and the current density of major product, *i.e.*, 1-propanol, together with formate are illustrated in Fig. 13d. Based on the experimental condition, it was concluded that production of 1-propanol involves the disulfidization of MoS_2 followed by the coupling of intermediate species on the surface of the MoS_2 single-crystal terrace.[179]

Li *et al.* fabricated amorphous 2D-molybdenum sulfide (MoS_X) on a polyethyleneimine (PEI)-modified rGO substrate and tested its CO_2 reduction ability in aqueous $NaHCO_3$ medium with high efficiency and selectivity. As revealed in Fig. 13e and f, the as obtained 2D/2D material selectively reduced CO_2 to CO with a very low overpotential of 140 mV, while the maximum faradaic efficiency of 85.1% for the product was obtained at −0.65 V (RHE) with a TOF value of 2.4 s^{-1}. They found that the PEI layer plays a major role in enhancing the catalytic activity of MoSx by suppressing the HER and stabilizing the CO_2 intermediate during CO_2 reduction.[180]

4.3.2 Photocatalytic CO_2 reduction reaction. The photocatalytic CO_2 reduction process is mainly governed through 5 sequential steps: (i) production of electrons and holes under the absorption of a photon by a semiconductor possessing a suitable band structure to dynamically and favorably reduce and oxidize CO_2 and H_2O, respectively. From the experimental interpretation, the estimated bandgap is considered to be 1.8–2.0 eV. In addition, it is also noted that the VB edge of the semiconductor photocatalyst should be more positive than the redox potential required for the water oxidation reaction, and similarly, the potential edge of the CB should be more negative than the redox potential for the CO_2 reduction. Thus, in the case of the photocatalytic CO_2 RR, the electrons are mainly generated by light excitation and the reduction abilities of the electrons rely on the potential of the conduction band. (ii) The second step involves the inhibition of the recombination process by separating photogenerated electron–hole pairs. (iii) In this step, the adsorption of a CO_2 molecule on the surface of the photocatalyst takes place followed by the transfer of an electron from the catalytic surface to the CO_2 molecule for the reduction process. For the adsorption of more CO_2, the photocatalyst should possess a high surface area and abundant active sites. (iv) The process involves the surface redox reaction originating from two different half reactions driven by the photogenerated electrons and holes. In this step, the holes oxidize water to molecular oxygen and electrons reduce CO_2 to various hydrocarbons such as CH_4, CO, CH_3OH, and HCOOH, as described in the earlier equations. This step is purely interconnected between photocatalysis and electrocatalysis and (v) the last step is the desorption of products within a particular time, and if the product is not released in time from the surface of the catalyst, then the catalyst becomes poisoned.[4,181]

Due to the insufficient reduction potential required for converting CO_2 into hydrocarbons, the MoS_2 photocatalyst exhibits negligible activity towards CO_2 reduction. Indeed, Geioushy and co-workers developed a 2D structured MoS_2 sheet by employing a hydrothermal method followed by annealing. The photoreduction of CO_2 proceeded under UV light irradiation and the formation of product, *i.e.*, methanol and acetaldehyde, with hydrocarbon selectivity was controlled by choosing a different aqueous solution such as 0.5 M $NaHCO_3$, NaOH and NaCl. The as-fabricated 2D MoS_2 with a stacked-layer exhibited superior CO_2 photoreduction conversion to different hydrocarbons such as methanol of 109.5 μmol g^{-1} (in 0.5 M $NaHCO_3$ aqueous solution) and acetaldehyde of 19.2 μmol g^{-1} (in 0.5 M NaCl aqueous solution), as shown in Fig. 14a. The

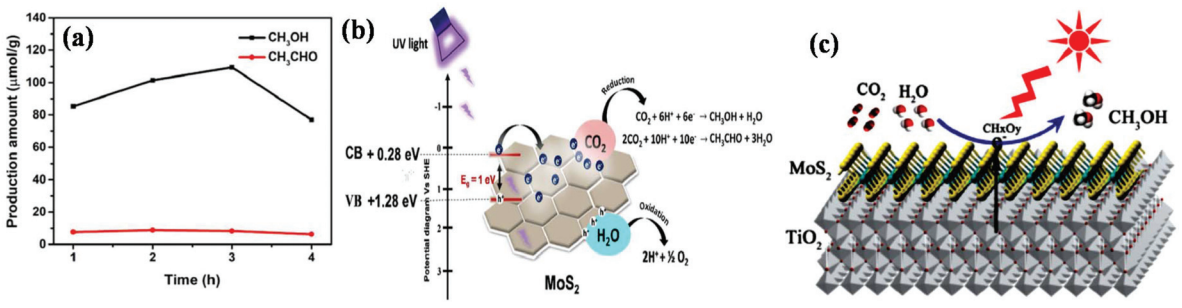

Fig. 14 (a) Rate of CO_2 reduction by MoS_2 sheets in 0.5 M $NaHCO_3$ and (b) schematic representation of the mechanistic pathway for photocatalytic CO_2 reduction over MoS_2 sheets. Reproduced with permission.[173] (c) Schematic illustration of the photoreduction of CO_2 to CH_3OH in the MoS_2/TiO_2 heterostructure. Reproduced with permission.[170]

variation in the different hydrocarbon products was mainly governed through the effect of the various solvents used as the scavenging unit. The selectivity of the product depends on the anion effect of the solvent, which delays the charge carrier recombination. It was observed that the use of 0.5 M $NaHCO_3$ solution resulted in the selectivity of CO_2 photoreduction towards the production of CH_3OH, accelerated through a 6-electron process. The selectivity for the production of CH_3OH is attributed to the formation of HCO_3^- ions, which inhibit the charge pair recombination and also initiate multiple reaction pathways originating from the production of various intermediates such as formate ions followed by formyl anion. Alternatively, the production of methanol can also proceed *via* a 10-electron process, which can be due to the dimerization of the intermediates. The overall CO_2RR reaction mechanism together with the reduction potential and multi-electron participation over the undecorated 2D MoS_2 sheet is depicted in Fig. 14b. It was also observed that with a change in the solvent from $NaHCO_3$ to NaOH and NaCl, the production of methanol somewhat decreased followed by an increase in acetaldehyde upon CO_2 photoreduction. The anion, *i.e.*, OH^- and Cl^-, present in the respective solvent behaves as a hole scavenger and efficiently separates the photogenerated electron–hole pairs by accumulating more electrons on the MoS_2 surface for the dimerization of two carbon species, resulting in the formation of CH_3CHO. The high photocatalytic performance is attributed to the 2D structure morphology of MoS_2, which boosts the transportation of electrons throughout the MoS_2 sheet and also facilitates the reduction of adsorbed CO_2 molecules.[173]

Further, Tu *et al.* designed a 2D MoS_2/TiO_2 hybrid nanojunction, in which 2D-MoS_2 nanosheets were grown on a TiO_2 nanosheet *via* an *in situ* method. The as-fabricated 2D nanojunction exhibited enhanced and selective CO_2 photoreduction, resulting in CH_3OH as the product in an aqueous $NaHCO_3$ solution. The photocatalytic performance was tested under UV-visible light with CO_2-saturated 1 M $NaHCO_3$ aqueous solution as the scavenger. The MoS_2/TiO_2 hybrid nanosheets with an MoS_2 content of 0.5 wt% selectively produced 10.6 μmol g^{-1} h^{-1} of CH_3OH, which is 2.9 times greater than that for TiO_2. The high photocatalytic efficiency is due to the unique coupling of MoS_2 and TiO_2 and the presence of Mo-terminated edges, which make it somewhat metallic, and also due to the presence of a high d-electron density, stabilizing the CHxOy intermediate during the CO_2RR under UV-Vis light illumination *via* electrostatic attraction. This type of 2D/2D hybrid nanojunction creates a compact contact, which is beneficial for the quick transfer of photogenerated electrons from TiO_2 to the Mo sites of MoS_2 with a high d-electron density to enhance the lifetime of the charge carriers and reduction efficiency. The mechanism for photoreduction involves the binding of negatively charged intermediate species such as $HCOO^-$ and CHO^- with the positively charged Mo cations through electrostatic attraction. The CO_2 reduction performance was also compared with the novel metal-loaded TiO_2 nanosheets, but the rate of reduction of CO_2 to the main product was lower than that for MoS_2-loaded TiO_2. The overall CO_2 reduction mechanism is schematically illustrated in Fig. 14c.[170]

To achieve an ideal bandgap and exposed active sites towards superior photocatalytic CO_2 reduction to value-added hydrocarbons, interfacial engineering between two 2D layered materials has emerged as a productive strategy. Qiu and co-workers employed electrostatic self-assembly as a cost-effective strategy for developing a series of 2D layered LDH-MoS_2 heterostructured nanocomposites, providing a novel route to produce syngas with tunable a H_2:CO proportion *via* CO_2 photoreduction under visible light irradiation. The electrostatic interaction is created throughout the reaction by the combination of positively charged LDH with the negatively charged surface of MoS_2, which provides a large interface for the CO_2RR, and by controlling the interface-rich heterostructure catalyst concentration, the production of the syngas (H_2:CO) proportion can be tuned. The experiment revealed that both LDH and MoS_2 individually were unable to produce syngas with a modulated H_2 : CO proportion; however, with a change in the loading percentage of MoS_2 from 0.1 to 0.3 in the LDH/MoS_2 heterostructure, the H_2:CO proportion was modulated, and with 0.30%, the proportion changed from 1 : 1 to 9 : 1. The origin of CO production from CO_2 was traced *via* a $^{13}CO_2$ isotopic experiment and analyzed through GC-MS spectrometry based on the signal obtained at m/z = 29, which is attributed to ^{13}CO. In addition, the overall experiment was conducted in the presence of a photosensitizer (H_2O/acetonitrile with $[Ru(bpy)_3]Cl_2 \cdot 6H_2O$) and sacrificial agent (TEOA), which accelerate the CO_2 photoreduction mechanism. Theoretical calculation of the binding energy and DFT calculation were employed to determine the charge transfer between the heterojunction and structure–activity relationship during the CO_2 photoreduction. The lower work function value of LDH (3.946 eV) than that of MoS_2 (5.92 eV) suggests that the flow of electron occurs from LDH to MoS_2 through the Mo–O–S chemical bond to maintain the equilibration of the Fermi level. A new type of charge distribution suggested electron accumulation near the LDH surface and predicted the flow of electrons from MoS_2 to the LDH surface. Moreover, the narrower bandgap energy observed *via* DOS calculation for the MoS_2/LDH heterojunction indicates the strong interaction between LDH and MoS_2. Prior to light illumination, firstly, photogenerated electrons are excited from the HOMO to LUMO of the Ru complex and then transferred to the CB of the LDH and MoS_2 *via* the interface and selectively reduce CO_2 to CO at the LDH surface and H_2 at both the LDH and MoS_2 surface by coupling with active hydrogen species.[182] Besides, Kumar *et al.* designed an advanced functionalized nanomaterial, *i.e.*, pyrrole-promoted RGO-MoS_2 nanocomposite, for the efficient photoreduction of CO_2 into solar fuels and observed superior photocatalytic CO_2 reduction.[183] In comparison, Xu *et al.* fabricated a 1D/2D TiO_2/MoS_2 hybrid nanostructure in which a 2D-MoS_2 sheet vertically and uniformly

covered 1D-TiO_2 electrospun fibres, which exhibited superior activity for CO_2 reduction to CH_3OH and CH_4 under UV-visible light irradiation. The developed 1D/2D nanohybrid achieved the production rate of 2.6 and 2.55 μmol g^{-1} h^{-1}, corresponding to CH_4 and CH_3OH, respectively, together with an apparent quantum yield of 0.16%. The photocatalytic activity is attributed to the presence of 2D-MoS_2, which enhances the light-harvesting properties of TiO_2 by increasing its absorption range.[184] In addition, other 2D–3D (MoS_2/SiC[185] and MoS_2/TiO_2[186]) have also been investigated for their CO_2 reduction activity; however, 2D–2D MoS_2-based materials for CO_2 reduction not been researched on a large scale.

4.3 Other applications of 2D MoS_2 and MoS_2-based 2D/2D heterostructures

In addition to energy conversion, other practical applications over MoS_2 have also been reported. To date, 2D-MoS_2 has been extensively applied for the photodegradation of various pollutants, antibiotics and dyes due to its absorption properties in a wide range of light, strong absorptivity properties, non-toxicity, stability against corrosion and environmentally friendly nature.[47] Ji and co-workers constructed a 2D/2D MoS_2/CeO_2 heterojunction photocatalyst,[102] which exhibited stronger degradation ability (88.5% in 120 min) than its neat counterpart with a huge reduction in the intensity of the peak in the UV-Vis spectrum with time, which shifted from 277 nm to 260 nm. In addition, the high surface to volume ratio, rapid response with improved sensitivity and low power consumption behaviour of 2D-MoS_2 materials have stimulated substantial research for different sensing applications such as biosensors, chemical sensors, electrochemical sensors, and gas sensors.[187] Hwang and co-workers developed a vertically aligned 2D-MoS_2 nanofilm with highly exposed Mo and S dangling bonds through the CVD method and tested it for the detection of heavy metals (Pb^{2+}) in tap water.[188] The material exhibited superior detection sensitivity with a limit of detection of 0.3 ppb at 180 s deposition time with a relative standard deviation of 3.1%. Again, various gas molecules such as NO, H_2, and NH_3 can be easily adsorbed on the surface of MoS_2. Additionally, 2D-MoS_2-based heterostructures have also been explored for the detection of different biomolecules and analytes in the environment. More importantly, in dye-sensitized solar cells (DSSCs), 2D-MoS_2 has exhibited superior performances due to its high electrocatalytic activity and high conductivity. Vikraman *et al.* fabricated a highly efficient layered MoS_2 counter electrode, which acts as a low-cost alternative to Pt-based DSSCs. Under 100 mW cm^{-2} (AM 1.5) stimulated solar irradiation, a high power conversion efficiency of 7.14% was achieved, which is nearly equal to that of 8.73% observed for the Pt/FTO counter electrode through the reduction of triiodide to iodide.[189]

Furthermore, 2D-MoS_2 has been extensively investigated for its application in electronic devices as a channel material mainly due to its atomically thin structure, which exhibits exceptional electronic properties including variable band gap and suitable charge carrier mobility.[190,191] Due to the presence of a band gap in 2D-MoS_2 compared to bulk MoS_2, its conductivity can be modulated, which is feasible for the electrostatic control of this material and make it a suitable candidate for application in the field of electronic devices, especially field-effect transistors (FETs) and low-power electronic devices.[192] It has been demonstrated that 2D-MoS_2 as an FET at room temperature exhibited an on/off drain current ratio of 10^8 with an enhancement in mobility of up to 200 cm^2 $(V\ s)^{-1}$.[193] Inspired by its direct band gap (~1.9 eV) with semiconducting behaviour and excellent mechanical properties such as flexibility and stretchability, 2D-MoS_2 is attracting great attention in the area of optoelectronic devices such as light sensing photodetectors, LEDs, and solar cells.[194,195] Zhai *et al.* designed an $NiTe_2$/MoS_2 2D/2D vertical heterostructure towards the study of a back-gated FET and photodetector as an electronic and optoelectronic device, respectively. The as-obtained stack layered materials resulting from the van der Waals epitaxial heterostructure provided enhanced electronic contact at the heterointerface, which enhanced the optoelectronic responses by 5 times and the electronic behaviour compared to that of neat MoS_2.[98] Besides, 2D-MoS_2 is widely used in the field of energy storage devices especially in supercapacitor applications due to its tunable interlayer distance and long cycle durability. The presence of a stacked-lamellar sheet-like structure together with suitable oxidation states over Mo, *i.e.*, +2 and +6, 2D-MoS_2 exhibits electrical double layer capacitance behavior. Considering that the van der Waals attraction present between the stacked layers is weak, the various guest components such as ions/electrons can be easily intercalated throughout the layer, thus increasing the charge discharge behaviour of the material together with its capacitance.[196,197] A novel intercalated nanostructured fibre electrode was developed by Wang *et al. via* the combination of MoS_2 sheets, which exhibited a high pseudocapacitance value, with graphene with high electrical conductivity. The aforementioned graphene/MoS_2 fibre electrode with an intercalated nanostructure possessed a high ion-accessible surface area, resulting a high specific capacitance of 368 F cm^{-3} at a current density of 0.1 A cm^{-3} when the MoS_2 content was up to 33.98%. In addition, the fibre electrode exhibited cycle stability of 80% for 8000 cycles with a current density of 12.8 mW h cm^{-3}.[198] Moreover, recently, Kirubasankar and co-workers constructed a 2D MoS_2/MXene nanohybrid interlayer structure, which restricted the electrostatic attraction and prevented the self-stacking of individual layers, thus providing high mass transfer between the electrolyte-electrode interface. The MoS_2/MXene nanohybrid presented a superior specific capacitance about 583 F g^{-1} with a rate capability of 2.5% at 1 A g^{-1} and 96.5% cycle stability up to 5000 cycles at 5 A g^{-1}.[199] The various photocatalytic and electrocatalytic applications towards energy conversion using 2D-MoS_2 and its 2D/2D heterostructures are presented in Table 1.

Table 1 Summary of the various applications of 2D-MoS_2 and MoS_2-based 2D/2D heterostructures

Photocatalyst	Synthesis method	Amount of photocatalyst and volume of sacrificial agent	Irradiation light source	Rate of hydrogen evolution	Apparent quantum yield/ Efficiency (AQY/AQE)	Ref.
(i) Photocatalytic hydrogen evolution reaction						
Few-layer MoS_2 nanosheets	Facile solvothermal treatment coupled with the liquid exfoliation strategy	50 mg in 100 mL of aqueous solution containing 0.35 M Na_2S and 0.25 M Na_2SO_3	300 W Xe	1241.3 mmol g^{-1} h^{-1}	—	138
Few-layer MoS_2 nanosheets	Liquid-phase exfoliation strategy	3 mg in 15% TEOA aqueous solution	300 W Xenon lamp	0.5 mmolg^{-1} h^{-1}	—	139
In-plane multiphasic 2D MoS_2 nanosheets	Chemical intercalation method	40 mg in 40 mL of deionized water with 0.01 M lactic acid	200 W Hg lamp	1.5 mmol h^{-1} g^{-1}	AQY = 12.90%	130
MoS_2/CdS	*Ex situ* adsorption-calcination	10 mg in 20 mL H_2O + 5 mL lactic acid	300 W Xenon lamp ($\lambda \geq 420$ nm)	18.43 mmol h^{-1} g^{-1}	AQE = 3.4%	92
MoS_2/g-C_3N_4	*Ex situ*	50 mg in 200 mL of 10 vol% glycerol solution	500 W Xenon lamp	10 000 μmol h^{-1} g^{-1}	—	200
MoS_2/g-C_3N_4	*Ex situ* ultrasonic assisted strategy	20 mg in 20 mL water/methanol (4 : 1 v/v) solution	300 W Xenon lamp	1497 μmol h^{-1} g^{-1}	AQY = 3.3%	121
$ZnIn_2S_4$/MoS_2	*Ex situ* electrostatic self-assembly process	Lactic acid	Visible light	4.974 mmol g^{-1} h^{-1}	—	95
Black phosphorous/ MoS_2	*In situ* solvothermal method	10 mg in 250 mL of 0.1 M Na_2S and 0.1 M Na_2SO_3 aq. solution	300 W Xenon lamp	1286 μmol h^{-1} g^{-1}	AQY = 1.2%	103
MoS_2/Ti_3C_2	*In situ* hydrothermal method	30 mg in 50 mL of methanol solution	300 W Xenon lamp	6144.7 mmol g^{-1} h^{-1}	—	201
MoS_2/CdS	*In situ* hydrothermal method	50 mg in 250 mL 0.4 M Na_2S and 0.4 M Na_2SO_3 solution	300 W Xenon lamp	26.32 mmol h^{-1} g^{-1}	AQY = 46.65%	141
MoS_2/g-C_3N_4	*In situ* probe sonication-assisted liquid exfoliation	50 mg in 250 mL of 0.1 M TEOA aqueous solution	300 W Xenon lamp	1155 μmol h^{-1} g^{-1}	AQY = 6.8%	142
MoS_2/$SnNb_2O_6$	*In situ* Hydrothermal method	50 mg in 50 mL of 20 vol% methanol.	300 W Xenon arc lamp	12.9 μmol h^{-1}	—	202
$CoMoS_2$/rGO/C_3N_4	*In situ* solvothermal method	100 mg in a mixed solution of TEOA and H_2O (volume ratio equal to 1/5)	300 W Xenon lamp	684 μmol g^{-1} h^{-1}	—	203
g-C_3N_4/graphene/MoS_2	*In situ* hydrothermal method	50 mg in 250 mL of 0.1 M TEOA solution	300 W Xenon lamp	317 μmol g^{-1} h^{-1}	AQY = 3.4%	143
Ti_3C_2 MXene/MoS_2/TiO_2	*In situ* two-step hydrothermal	10 mg in aqueous acetone with dissolved sacrificial reagent (TEOA)	300 W Xenon lamp	6425.297 μmol h^{-1} g^{-1}	AQY = 4.61%	204
S-Doped polymeric carbon nitride/MoS_2	One-pot hydrothermal-polymerization method	50 mg in 10 vol% TEOA aq. solution	300 W Xenon lamp	2120 μmol h^{-1} g^{-1}	AQE = 5.7%	110
N-Doped MoS_2/S-doped g-C_3N_4	One-step thermal polycondensation method	50 mg in 100 mL 10 vol% TEOA	300 W Xenon lamp	658.5 μmol g^{-1} h^{-1}	—	205
MoS_2/CeO_2	*In situ* hydrothermal	20 mg in 20 mL of 10 vol% methanol	150 W xenon lamp	508.44 μmol h^{-1}	—	89
MoS_2/$CaIn_2S_4$	*In situ* hydrothermal	20 mg in 20 mL of 0.025 M Na_2S and 0.025 M Na_2SO_3 aq. solution	150 W xenon arc lamp	602.35 μmol h^{-1}	Apparent Conversion Efficiency = 9.71%	76
MoS_2/$ZnIn_2S_4$	One-pot hydrothermal	20 mg in 20 mL of 0.25 M Na_2SO_3 and 0.35 M Na_2S aq. solution	150 W xenon arc lamp	379.1 μmol h^{-1}	Apparent Conversion Efficiency = 6.07%	115
MoS_2/NiFe LDH	*In situ* electrostatic self-assembled chemistry	30 mg in 30 mL of 10 vol% CH_3OH aq. solution	125 W medium pressure Hg lamps	550.9 μmol h^{-1}	—	104
MoS_2/$MgIn_2S_4$	*In situ* hydrothermal method	20 mg in 20 mL of 0.25 M Na_2SO_3 and 0.35 M Na_2S aq. solution	150 W Xenon arc lamp	570.8 μmol h^{-1}	—	90
UiO-66-NH_2 MOF/MoS_2	*In situ* hydrothermal method	20 mg in 20 mL of 10% methanol solution	300 W Xe arc lamp	512.9 μmol h^{-1}	Apparent Conversion Efficiency = 3.84%	113
P-MoS_2/CdS	*In situ* hydrothermal	10 mg in 100 mL of 0.35 M Na_2S and 0.25 M Na_2SO_3	300 W Xe lamp	58.9 μmol h^{-1}	AQE = 19.0%	206
MoS_2/Co–Al LDH	*In situ* hydrothermal	50 mg in 80 mL methanol solution	300 W Xe lamp	17.1 μmol g^{-1} h^{-1}	—	207

Table 1 *(Contd.)*

Photocatalyst	Synthesis method	Amount of photocatalyst and volume of sacrificial agent	Irradiation light source	Rate of hydrogen evolution	Apparent quantum yield/ Efficiency (AQY/AQE)	Ref.
MoS_2/g-C_3N_4	*In situ* solvothermal	5 mg in 40 mL of 10% TEOA solution	300 W Xenon arc lamp	1787 μmol h^{-1} g^{-1}	—	208

Catalyst	Synthesis process	Electrolyte	Current Density (mA cm^{-2})	Over-potential (mV)	Tafel slope (mV dec^{-1})	Ref.
(ii) Electrocatalytic hydrogen evolution reaction						
Defect-rich MoS_2 nanowall	Hydrothermal	0.5 M H_2SO_4	10	95	78	135
Fractal-shaped single-layer MoS_2	CVD method	0.5 M H_2SO_4	10	185	45	84
Single-atom metal-doped MoS_2	One-pot hydrothermal method	0.1 M H_2SO_4	10	60	96	209
MoS_2 nanosheets	Hydrothermal followed by annealing process	0.5 M H_2SO_4 and 1 M KOH	10 mA mg^{-1}	(i) Acidic = 171 (ii) alkaline = 162	(i) Acidic = 54 (ii) alkaline = 68	133
Surfactant-exfoliated 2D molybdenum disulphide	Liquid-phase exfoliation	0.5 M H_2SO_4	−4.96	420	94	210
2D MoS_2 nanosheets	Hydrothermal method	0.5 M H_2SO_4	25	280	90	88
2D MoS_2 Thin Films	CVD	0.5 M H_2SO_4	60	640	90	85
$FePS_3$/MoS_2	*In situ* Hydrothermal method	1 M KOH solution and 0.5 M H_2SO_4 solution	10	(i) 1 M KOH = 175 (ii) 0.5 M H_2SO_4 = 168	(i) 1 M KOH = 127 (ii) 0.5 M H_2SO_4 = 107	211
Co-BDC/MoS_2	*In situ* sonication-assisted solution strategy	1 M KOH solution	−10	248	86	134
MoP/MoS_2	*In situ* Phosphorization	0.5 M H_2SO_4, 1 M phosphate buffered solutions (PBS) and 1 M KOH	10	(i) Neutral = 96 (ii) alkaline = 54 (iii) acidic = 69	(i) Neutral = 48 (ii) alkaline = 58 (iii) acidic = 61	106
MoS_2/black phosphorus	*In situ*	0.5 M H_2SO_4, 1 M KOH and 1 M PBS	10	(i) Neutral = 258 (ii) alkaline = 237 (iii) acidic = 126	(i) Neutral = 154 (ii) alkaline = 99 (iii) acidic = 68	136
MoS_2/N-doped graphdiyne	*In situ* solvothermal method	0.5 M H_2SO_4	10	186	63	212
MoS_2/graphene	*In situ* self-assembly method *via* electrostatic attraction	0.5 M H_2SO_4 and 1.0 M KOH	10	(i) Acidic = 180 (ii) alkaline = 183	(i) Acidic = 79 (ii) alkaline = 127	73
MoS_2/graphene	*Ex situ* two-step sonication method	6 M KOH	25	125	41	213
RGO/MoS_2	One-step hydrothermal method	0.5 M H_2SO_4 solution	100	150	52.5	214
MoS_2/graphene	One-step *in situ* solvothermal	0.5 M H_2SO_4	10	94.2	140	215
MoS_2/g-C_3N_4	One-pot method	0.5 M H_2SO_4	10	140	45	109
MoS_2/carbon nitride	*In situ* hydrothermal	0.1 M KOH	10	153	43	61

Photocatalyst	Synthesis method	Amount of photocatalyst and volume of sacrificial agent	Irradiation light source	Rate of NH_3 synthesis	Ref.
(iii) Photocatalytic nitrogen reduction reaction					
Ultrathin MoS_2	Hydrothermal followed by ultra-sonication	15 mg in 200 mL DI water + HCl solution (pH = 3.5)	500 W Xenon lamp	325 μmol h^{-1} g^{-1}	50
MoS_2/biochar	*In situ*	20 mg in 100 mL of DI water	300 W Xenon lamp	37.878 μmol g^{-1} h^{-1}	216
MoS_2/$MgIn_2S_4$	*In situ* two-step hydrothermal method	15 mg in 50 mL distilled water + HCl solution (pH = 3.6)	250 W Hg lamp	2509.2 μmol h^{-1} g^{-1}	90

Catalyst	Synthesis method	Electrolyte	Rate of NH_3 evolved	Faradic efficiency (%)	Potential (V)	Ref.
(iv) Electrocatalytic nitrogen reduction reaction						
2D-MoS_2	Hydrothermal followed by annealing method	10 mg in 0.1 M Li_2SO_4 solution (pH = 3.0)	43.4 μg h^{-1} mg^{-1}	9.81	-0.2	158
MoS_2	Hydrothermal method	0.1 M Na_2SO_4.	8.08×10^{-11} $mols^{-1}$ cm^{-1}	1.17	−0.5	117

Table 1 *(Contd.)*

Catalyst	Synthesis method	Electrolyte	Rate of NH_3 evolved	Faradic efficiency (%)	Potential (V)	Ref.
MoS_2/C_3N_4	*In situ*	0.1 M Na_2SO_4	19.86 μg h^{-1} mg^{-1}	6.87	−0.5	75
MoS_2/RGO	*In situ* hydrothermal	0.1 M $LiClO_4$	24.82 μg h^{-1} mg^{-1}	4.58	−0.45	160
MoS_2/C_3N_4	*In situ* hydrothermal	0.1 M $LiClO_4$ solution	18.5 μg h^{-1} mg^{-1}	17.8	−0.3	159

Photocatalyst	Synthesis method	Amount of photocatalyst and volume of sacrificial agent	Light source	Main product	Yield	AQY/ AQE	Ref.
(v) Photocatalytic carbon dioxide reduction							
2D-MoS_2 sheets	Hydrothermal followed by annealing method	0.1 g in 50 mL 0.5 M (i) $NaHCO_3$, (ii) NaOH and (iii) NaCl aqueous solution	150 W medium pressure mercury vapour lamp	(i) Methanol in 0.5 M $NaHCO_3$ (ii) Acetaldehyde in 0.5 M NaCl	(i) 109.5 μmol g^{-1} (ii) 19.2 μmol g^{-1}	—	173
Polypyrrole/ rGO-MoS_2	*In situ* wet chemical synthesis	50 mg in 20 mL of 0.5 M $NaHCO_3$	300 W Xenon lamp	(i) CO, (ii) CH_4 (iii) H_2	(i) 3.95 μmol g^{-1} h^{-1} (ii) 1.50 μmol g^{-1} h^{-1} (iii) 4.19 μmol g^{-1} h^{-1}	AQE = 0.30%	183
MoS_2/g-C_3N_4	*Ex situ* hydrothermal deposition method	50 mg in 100 mL deionized water	300 W Xenon lamp	CO	58.59 μmol g^{-1} for 7 h	AQY = 0.255%	217
MoS_2/TiO_2	*In situ* hydrothermal	0.1 g in 200 mL of 1 M $NaHCO_3$ solution (pH = 8)	300 W xenon arc lamp	CH_3OH	10.6 μmol h^{-1} g^{-1}	—	170
LDH/MoS_2	*Ex situ* electrostatic self-assembly	Photocatalyst (0.3 mg mL^{-1}) and $[Ru(bpy)_3]Cl_2 \times 6H_2O$ (3.3 mg) were suspended in 10 mL aqueous solution containing H_2O : CH_3CN : TEOA = 1 : 3 : 1 (V/V/V)	300 W Xe lamp	(i) CO (ii) H_2	(i) 3617 μmol h^{-1} g^{-1} (ii) 6187 μmol h^{-1} g^{-1}	—	182

Catalyst	Synthesis method	Electrolyte	Main product	Current density (mA cm^{-2})	Faradic efficiency	Potential	Ref.
(vi) Electrocatalytic carbon dioxide reduction							
Hydrophobic exfoliated MoS_2 nanosheets	Ball-milling followed by CVD	1-Ethyl-3-methylimidazolium tetrafluoroborate (EMIM-BF4) aqueous solution	CO	61	81.2% at −0.9 V	−1.1 V	178
MoS_2 thin film	Mechanical exfoliation followed by CVD method	0.10 M potassium phosphate buffer or 0.10 M sodium carbonate that was acidified to pH 6.8	1-Propanol	−0.1	3.5%	−0.59 V	179
rGO–PEI–MoSx	*In situ* electrodeposition method	0.5 M aqueous $NaHCO_3$	CO	55	85.1%	540 mV	180

5. Conclusion and future perspectives

Over the past decade, the development of MoS_2-based materials and their chemistry have attracted significant interest for the photo/electro catalytic generation of energy from water, N_2 and CO_2. According to the recent reports, we found that in comparison to bulk MoS_2, ultra-thin two-dimensional MoS_2 with abundant active edge sites possesses extraordinary optical and electrochemical properties. Interestingly, for an efficient catalytic reaction, the two most common phases, *i.e.*, 1T and 2H, of MoS_2 are mainly responsible. The semiconducting 2H phase of 2D-MoS_2 with its nanostructured condition possesses a lower amount of catalytic active sites due to its inert basal plane, whereas the 1T phase exhibits more active sites. Thus, the crystal-phase engineering of 2D-MoS_2 from 2H to 1T through precise control of the transformation has achieved great results towards energy conversion applications such as water reduction reaction, nitrogen reduction reaction and CO_2 reduction reaction. In some cases, it was seen that phase engineering is responsible for the activation of the basal plane of MoS_2, which facilitates the adsorption of H_2, N_2 and CO_2 on its surface and is beneficial for achieving superior photo/electro catalytic activity. Although the metallic 1T phase possesses interesting properties, which are beneficial towards energy conversion reactions, its low stability at high temperature somewhat limits its activity. Due to the stability issue of the 1T phase of MoS_2, the coexistence of both 1T and 2H phases in one component through phase engineering has been developed in the catalysis field, but very little work has been reported on this to date. Currently, the maximum studies on 2D-MoS_2 are based on its most stable semiconducting phase, which makes it a good candidate in the field of both photo and electrocatalysis. However, among the many aspects of improving the catalytic activity of neat 2D-MoS_2, the formation of heterostructure of 2D-MoS_2 with other 2D-semiconductors/catalysts has attracted significant research interest. Therefore, in this review, we especially focused on the design of semiconducting 2D-MoS_2 with other 2D materials using various synthetic routes especially *ex situ*, *in situ* and one-pot strategies. Further, the photo and electrochemical activity towards energy production through water splitting, CO_2 reduction and N_2 fixation over 2D-MoS_2-based materials were discussed elaborately. The photocatalytic and electrocatalytic activity of the resulting 2D/2D heterostructure depend on the coupling interaction of semiconducting 2D-MoS_2 with other 2D materials. The powerful combination of two 2D materials is mainly governed through vertical and lateral interactions, forming a 2D/2D heterostructure. In contrast to 1D/2D- and 3D/2D-based structures, the 2D/2D combination-based heterostructure furnishes the largest degree of contact in the face-to-face fashion, which results in superior charge mobility throughout the interface.

- Challenges and opportunities

Although 2D-MoS_2-based 2D/2D heterostructured materials have achieved very encouraging progress in a wide range of fields from photocatalysis to electrocatalysis, some challenges remain, which demand an urgent solution. The various challenges and opportunities over MoS_2-based 2D/2D heterostructures are elaborately discussed in the following section. (i) Although many synthetic strategies have been developed for the synthesis of high quality, large surface area ultrathin MoS_2 nanosheet, the controlled synthesis of the desired layer with high charge carrier mobility of MoS_2 still needs further research attention. Furthermore, theoretical and practical research is needed for designing efficient lateral or vertical 2D/2D heterostructures with intimate contact and efficient interfacial coupling. (ii) Also, 2D-MoS_2-based heterostructures need low-cost synthetic methods for the large-scale production of 2D/2D catalysts. (iii) A thorough experimental and theoretical review regarding the activity improvement of 2D/2D-MoS_2-based materials has been presented. However, some fundamental aspects still need to be addressed to achieve the highest activity result in the target reaction. (iv) Although 2D-MoS_2 possesses edge-active sulfur sites, inert basal planes and high conductivity, MoS_2 nanosheet-based materials do not achieve the desired performance for electrocatalytic H_2 evolution. In addition, MoS_2 nanosheets generally show excellent hydrogen evolution activity in acidic medium, but the lack of expected performance in alkaline and neutral media restricts it as a versatile catalyst. Thus, more efforts and research are required for its further development. (v) The overall solar energy conversion efficiency of natural photosynthesis is much lower than 1%; however artificial photosynthesis can provide a great efficiency for solar energy conversion to fuel. Nevertheless, the selection of a photocatalytic system with long-term use and durability is very challenging. Hence, a conversion efficiency 10% or higher must be achieved for the process to be commercialized. MoS_2 provides a wide photon absorption range and generates multiple excitons, and thus can be an ideal candidate as a photocatalytic system for future use. 2D-MoS_2- and 2D/2D MoS_2-based materials have widely reported for photocatalysis, but the role of MoS_2 as a co-catalyst and primary catalyst has yet to be fully understood. In the case of the photocatalytic mechanism over 2D/2D heterostructures, although various charge transport and separation mechanisms across the 2D–2D junction have been proposed, some are still under debate due to the lack of solid theoretical evidence for the fundamental understanding of the mechanistic pathway. Thus, the importance of DFT studies regarding rational theoretical calculations should also emphasized in the photocatalytic reaction field. (vi) 2D-MoS_2-based materials have received eye-catching progress in the field of the nitrogen reduction reaction. Both the theoretical investigation and practical application suggest a good result in ammonia synthesis; however, product selectivity is still a major concern, given that hydrazine and other nitrogen oxide products compete with ammonia. Thus, a detailed theoretical analysis should be carried out to determine the reaction mechanism of nitrogen reduction over MoS_2-based materials. Considering the theoretical aspects, MoS_2 nanosheets and 2D–2D-coupled heterostructures should be designed with optimized parameters such as defect-rich MoS_2 or highly edge active Mo ions. (vii)

Although 2D-MoS_2 possesses interesting properties for the N_2 reduction reaction, its exploration in the photocatalytic nitrogen reduction field is limited. Thus, combining theoretical aspects with photocatalytic experiments needs more work this field. (viii) Although recent reports suggest the enhanced CO_2 reduction activity over MoS_2-based materials, very little work has been done in the field of photo and electrochemical CO_2 reduction. MoS_2 with active basal plane reaction sites for the CO_2RR and its coupling with other suitable CO_2 reduction catalysts may be a rising trend in this field. Hence, DFT studies should be firstly utilized to demonstrate the basic guidelines for designing of 2D-MoS_2-based materials with maximum catalytic sites for selective CO_2 reduction.

Finally, the scope of practical applications over MoS_2-based 2D/2D heterostructured materials can be further expanded to other field.

Conflicts of interest

There are no conflicts of interest to declare.

Acknowledgements

Authors are very much thankful to S'O'A management for their constant support and encouragement.

References

1 P. Nejat, F. Jomehzadeh, M. M. Taheri, M. Gohari and M. Z. Muhd, *Renewable Sustainable Energy Rev.*, 2015, **43**, 843–862.
2 L. Suganthi and A. A. Samuel, *Renewable Sustainable Energy Rev.*, 2012, **16**, 1223–1240.
3 X. Li, J. Yu, J. Low, Y. Fang, J. Xiao and X. Chen, *J. Mater. Chem. A*, 2015, **3**, 2485–2534.
4 J. Wu, Y. Huang, W. Ye and Y. Li, *Adv. Sci.*, 2017, **4**, 1–29.
5 T. Hisatomi, J. Kubota and K. Domen, *Chem. Soc. Rev.*, 2014, **43**, 7520–7535.
6 Z. Wang, C. Li and K. Domen, *Chem. Soc. Rev.*, 2019, **48**, 2109–2125.
7 X. Chen, N. Li, Z. Kong, W. J. Ong and X. Zhao, *Mater. Horiz.*, 2018, **5**, 9–27.
8 J. Luo, S. Zhang, M. Sun, L. Yang, S. Luo and J. C. Crittenden, *ACS Nano*, 2019, **13**, 9811–9840.
9 J. Xiong, J. Di and H. Li, *Adv. Sci.*, 2018, **5**, 1800244.
10 J. Sun, F. Tian, F. Yu, Z. Yang, B. Yu, S. Chen, Z. Ren and H. Zhou, *ACS Catal.*, 2020, **10**, 1511–1519.
11 X. Yang and D. Wang, *ACS Appl. Energy Mater.*, 2018, **1**, 6657–6693.
12 S. Ikram, *Nano Res.*, 2016, **2**, 10.
13 M. Darwish and A. Mohammadi, *Nanotechnology in Environmental Science*, 2018, pp. 315–350.
14 R. Xu, L. Du, D. Adekoya, G. Zhang, S. Zhang, S. Sun and Y. Lei, *Adv. Energy Mater.*, 2020, 2001537.
15 W. Xu, Y. Bai and Y. Yin, *Adv. Mater.*, 2018, **30**, 1–7.
16 B. Dubertret, T. Heine and M. Terrones, *Acc. Chem. Res.*, 2015, **48**, 1–2.
17 J. Low, S. Cao, J. Yu and S. Wageh, *Chem. Commun.*, 2014, **50**, 10768–10777.
18 Z. Li, X. Zhang, H. Cheng, J. Liu, M. Shao, M. Wei, D. G. Evans, H. Zhang and X. Duan, *Adv. Energy Mater.*, 2020, **10**, 1–17.
19 Z. Hua, *ACS Nano*, 2015, **9**, 9451–9469.
20 B. Luo, G. Liu and L. Wang, *Nanoscale*, 2016, **8**, 6904–6920.
21 K. S. Novoselov, A. K. Geim, S. V. Morozov, D. Jiang, Y. Zhang, S. V. Dubonos, I. V. Grigorieva and A. A. Firsov, *Science*, 2004, **306**, 666–669.
22 R. Mas-Ballesté, C. Gómez-Navarro, J. Gómez-Herrero and F. Zamora, *Nanoscale*, 2011, **3**, 20–30.
23 S. Das, J. A. Robinson, M. Dubey, H. Terrones and M. Terrones, *Annu. Rev. Mater. Res.*, 2015, **45**, 1–27.
24 J. Di, C. Yan, A. D. Handoko, Z. W. Seh, H. Li and Z. Liu, *Mater. Today*, 2018, **21**, 749–770.
25 C. N. R. Rao, K. Gopalakrishnan and U. Maitra, *ACS Appl. Mater. Interfaces*, 2015, **7**, 7809–7832.
26 R. Lv, J. A. Robinson, R. E. Schaak, D. Sun, Y. Sun, T. E. Mallouk and M. Terrones, *Acc. Chem. Res.*, 2015, **48**, 56–64.
27 J. Theerthagiri, R. A. Senthil, B. Senthilkumar, A. Reddy Polu, J. Madhavan and M. Ashokkumar, *J. Solid State Chem.*, 2017, **252**, 43–71.
28 K. F. Mak, C. Lee, J. Hone, J. Shan and T. F. Heinz, *Phys. Rev. Lett.*, 2010, **105**, 2–5.
29 O. V. Yazyev and A. Kis, *Mater. Today*, 2015, **18**, 20–30.
30 M. Pumera, Z. Sofer and A. Ambrosi, *J. Mater. Chem. A*, 2014, **2**, 8981–8987.
31 Q. H. Wang, K. Kalantar-Zadeh, A. Kis, J. N. Coleman and M. S. Strano, *Nat. Nanotechnol.*, 2012, **7**, 699–712.
32 J. Huo, R. Ge, Y. Liu, J. Guo, L. Lu, W. Chen, C. Liu, H. Gao and H. Liu, *Sustainable Mater. Technol.*, 2020, **24**, e00161.
33 D. K. Nandi, U. K. Sen, D. Choudhury, S. Mitra and S. K. Sarkar, *Electrochim. Acta*, 2014, **146**, 706–713.
34 I. Song, C. Park and H. C. Choi, *RSC Adv.*, 2015, **5**, 7495–7514.
35 Y. Yu, G. H. Nam, Q. He, X. J. Wu, K. Zhang, Z. Yang, J. Chen, *et al.*, *Nat. Chem.*, 2018, **10**, 638–643.
36 Q. Ding, B. Song, P. Xu and S. Jin, *Chem*, 2016, **1**, 699–726.
37 H. Wang, C. Li, P. Fang, Z. Zhang and J. Z. Zhang, *Chem. Soc. Rev.*, 2018, **47**, 6101–6127.
38 X. Huang, Z. Zeng and H. Zhang, *Chem. Soc. Rev.*, 2013, **42**, 1934–1946.
39 U. Krishnan, M. Kaur, K. Singh, M. Kumar and A. Kumar, *Superlattices Microstruct.*, 2019, **128**, 274–297.
40 D. Wang, X. Zhang, S. Bao, Z. Zhang, H. Fei and Z. Wu, *J. Mater. Chem. A*, 2017, **5**, 2681–2688.
41 R. Ganatra and Q. Zhang, *ACS Nano*, 2014, **8**, 4074–4099.
42 T. A. Shifa, F. Wang, Y. Liu and J. He, *Adv. Mater.*, 2019, **31**, 1804828.

43 J. Kibsgaard, Z. Chen, B. N. Reinecke and T. F. Jaramillo, *Nat. Mater.*, 2012, **11**, 963–969.
44 A. B. Laursen, S. Kegnæs, S. Dahl and I. Chorkendorff, *Energy Environ. Sci.*, 2012, **5**, 5577–5591.
45 Z. Li, X. Meng and Z. Zhang, *J. Photochem. Photobiol., C*, 2018, **35**, 39–55.
46 C. Wu, J. Zhang, X. Tong, P. Yu, J. Y. Xu, J. Wu, Z. M. Wang, J. Lou and Y. L. Chueh, *Small*, 2019, **15**, 1–25.
47 Z. Wang and B. Mi, *Environ. Sci. Technol.*, 2017, **51**, 8229–8244.
48 Y. Liu, D. Huang, M. Cheng, Z. Liu, C. Lai, C. Zhang, C. Zhou, W. Xiong, L. Qin, B. Shao and Q. Liang, *Coord. Chem. Rev.*, 2020, **409**, 213220.
49 T. R. Thurston and J. P. Wilcoxon, *J. Phys. Chem. B*, 1999, **103**, 11–17.
50 S. Sun, X. Li, W. Wang, L. Zhang and X. Sun, *Appl. Catal., B*, 2017, **200**, 323–329.
51 F. Meng, J. Li, S. K. Cushing, M. Zhi and N. Wu, *J. Am. Chem. Soc.*, 2013, **135**, 10286–10289.
52 C. K. Sumesh and S. C. Peter, *Dalton Trans.*, 2019, **48**, 12772–12802.
53 J. Su, G. D. Li, X. H. Li and J. S. Chen, *Adv. Sci.*, 2019, **6**, 1–19.
54 P. Solís-Fernández, M. Bissett and H. Ago, *Chem. Soc. Rev.*, 2017, **46**, 4572–4613.
55 X. Zhang, X. Yuan, L. Jiang, J. Zhang, H. Yu, H. Wang and G. Zeng, *Chem. Eng. J.*, 2020, **390**, 124475.
56 Y. Li, C. Gao, R. Long and Y. Xiong, *Mater. Today Chem.*, 2019, **11**, 197–216.
57 X. Liu, Q. Zhang and D. Ma, *Sol. RRL*, 2021, **5**, 2000397.
58 T. Su, Z. Qin, H. Ji and Z. Wu, *Nanotechnology*, 2019, **30**, 502002.
59 M. M. Ayyub, R. Singh and C. N. R. Rao, *Sol. RRL*, 2020, **4**, 2000050.
60 S. Cao, B. Shen, T. Tong, J. Fu and J. Yu, *Adv. Funct. Mater.*, 2018, **28**, 1–11.
61 X. Qian, J. Ding, J. Zhang, Y. Zhang, Y. Wang, E. Kan, X. Wang and J. Zhu, *Nanoscale*, 2018, **10**, 1766–1773.
62 W. J. Ong and K. P. Y. Shak, *Sol. RRL*, 2020, **4**, 2000132.
63 W. J. Ong, *Front. Mater.*, 2017, **4**, 11.
64 H. Qi, L. Wang, J. Sun, Y. Long, P. Hu, F. Liu and X. He, *Crystals*, 2018, **8**, 35.
65 H. Hou, X. Zeng and X. Zhang, *Sci. China Mater.*, 2020, **2119**, 1–34.
66 T. Su, Q. Shao, Z. Qin, Z. Guo and Z. Wu, *ACS Catal.*, 2018, **8**, 2253–2276.
67 A. Pant, Z. Mutlu, D. Wickramaratne, H. Cai, R. K. Lake, C. Ozkan and S. Tongay, *Nanoscale*, 2016, **8**, 3870–3887.
68 S. Wang, X. Wang, J. H. Warner and W. E. T. Al, *ACS Nano*, 2015, **9**, 5246–5254.
69 A. Behranginia, P. Yasaei, A. K. Majee, V. K. Sangwan, F. Long, C. J. Foss, T. Foroozan, S. Fuladi, M. R. Hantehzadeh, R. Shahbazian-Yassar, M. C. Hersam, Z. Aksamija and A. Salehi-Khojin, *Small*, 2017, **13**, 1–11.
70 Y. Yoo, Z. P. Degregorio and J. E. Johns, *J. Am. Chem. Soc.*, 2015, **137**, 14281–14287.
71 P. Das, Q. Fu, X. Bao and Z. S. Wu, *J. Mater. Chem. A*, 2018, **6**, 21747–21784.
72 Q. Yu, Y. Luo, A. Mahmood, B. Liu and H.-M. Cheng, *Electrochem. Energy Rev.*, 2019, **2**, 373–394.
73 X. Yu, G. Zhao, S. Gong, C. Liu, C. Wu, P. Lyu, G. Maurin and N. Zhang, *ACS Appl. Mater. Interfaces*, 2020, **12**, 24777–24785.
74 L. Shi, W. Ding, S. Yang, Z. He and S. Liu, *J. Hazard. Mater.*, 2018, **347**, 431–441.
75 Z. Zhao, S. Luo, P. Ma, Y. Luo, W. Wu, Y. Long and J. Ma, *ACS Sustainable Chem. Eng.*, 2020, **8**, 8814–8822.
76 G. Swain, S. Sultana, J. Moma and K. Parida, *Inorg. Chem.*, 2018, **57**, 10059–10071.
77 J. Wan, Y. Zhang, R. Wang, L. Liu, E. Liu, J. Fan and F. Fu, *J. Hazard. Mater.*, 2020, **384**, 121484.
78 W. Li, Y. Zhang, X. Long, J. Cao, X. Xin, X. Guan, J. Peng and X. Zheng, *Sensors*, 2019, **19**, 1–12.
79 K. Krishnamoorthy, P. Pazhamalai, G. K. Veerasubramani and S. J. Kim, *J. Power Sources*, 2016, **321**, 112–119.
80 K. Gacem, M. Boukhicha, Z. Chen and A. Shukla, *Nanotechnology*, 2012, **23**, 23–28.
81 D. Sahoo, B. Kumar, J. Sinha, S. Ghosh, S. S. Roy and B. Kaviraj, *Sci. Rep.*, 2020, **10**, 1–12.
82 A. Gupta, V. Arunachalam and S. Vasudevan, *J. Phys. Chem. Lett.*, 2016, **7**, 4884–4890.
83 H. Wang, D. Tran, J. Qian, F. Ding and D. Losic, *Adv. Mater. Interfaces*, 2019, **6**, 1900915.
84 Y. Wan, Z. Zhang, X. Xu, Z. Zhang, P. Li, X. Fang, K. Zhang, K. Yuan, K. Liu, G. Ran, Y. Li, Y. Ye and L. Dai, *Nano Energy*, 2018, **51**, 786–792.
85 S. Li, S. Wang, M. M. Salamone, A. W. Robertson, S. Nayak, H. Kim, S. C. E. Tsang, M. Pasta and J. H. Warner, *ACS Catal.*, 2017, **7**, 877–886.
86 P. Gnanasekar, D. Periyanagounder, A. Nallathambi, S. Subramani, M. Palanisamy and J. Kulandaivel, *CrystEngComm*, 2018, **20**, 4249–4257.
87 F. Wang, T. A. Shifa, X. Zhan, Y. Huang, K. Liu, Z. Cheng, C. Jiang and J. He, *Nanoscale*, 2015, **7**, 19764–19788.
88 S. Muralikrishna, K. Manjunath, D. Samrat, V. Reddy, T. Ramakrishnappa and D. H. Nagaraju, *RSC Adv.*, 2015, **5**, 89389–89396.
89 G. Swain, S. Sultana, B. Naik and K. Parida, *ACS Omega*, 2017, **2**, 3745–3753.
90 G. Swain, S. Sultana and K. Parida, *ACS Sustainable Chem. Eng.*, 2020, **8**, 4848–4862.
91 L. Li, Z. Qin, L. Ries, S. Hong, T. Michel, J. Yang, C. Salameh, M. Bechelany, P. Miele, D. Kaplan, M. Chhowalla and D. Voiry, *ACS Nano*, 2019, **13**, 6824–6834.
92 M. Xiong, J. Yan, B. Chai, G. Fan and G. Song, *J. Mater. Sci. Technol.*, 2020, **56**, 179–188.
93 R. H. Jeong, J. W. Lee, D. I. Kim, J. W. Yang, S. Park and J.-H. Boo, *Nanotechnology*, 2020, **31**, 155704.
94 W. Li, L. Wang, Q. Zhang, Z. Chen, X. Deng, C. Feng, L. Xu and M. Sun, *J. Alloys Compd.*, 2019, **808**, 151681.

95 L. Huang, B. Han, X. Huang, S. Liang, Z. Deng, W. Chen, M. Peng and H. Deng, *J. Alloys Compd.*, 2019, **798**, 553–559.
96 Z. Hennighausen, C. Lane, A. Benabbas, K. Mendez, M. Eggenberger, P. M. Champion, J. T. Robinson, A. Bansil and S. Kar, *ACS Appl. Mater. Interfaces*, 2019, **11**, 15913–15921.
97 R. K. Biroju, S. Pal, R. Sharma, P. K. Giri and T. N. Narayanan, *Nanotechnology*, 2017, **28**, 085101.
98 X. Zhai, X. Zhai, X. Xu, J. Peng, J. Peng, F. Jing, F. Jing, Q. Zhang, H. Liu, H. Liu, H. Liu, Z. Hu and Z. Hu, *ACS Appl. Mater. Interfaces*, 2020, **12**, 24093–24101.
99 J. Zhang, J. H. Wang, P. Chen, Y. Sun, S. Wu, Z. Y. Jia, X. B. Lu, H. Yu, W. Chen, J. Q. Zhu, G. B. Xie, R. Yang, D. X. Shi, X. L. Xu, J. Y. Xiang, K. H. Liu and G. Y. Zhang, *Adv. Mater.*, 2016, **28**, 1950–1956.
100 J. Shi, R. Tong, X. Zhou, Y. Gong, Z. Zhang, Q. Ji, Y. Zhang, Q. Fang, L. Gu, X. Wang, Z. Liu and Y. Zhang, *Adv. Mater.*, 2016, **28**, 10664–10672.
101 E. Lee, S. G. Lee, W. H. Lee, H. C. Lee, N. N. Nguyen, M. S. Yoo and K. Cho, *Chem. Mater.*, 2020, **32**, 4544–4552.
102 R. Ji, Z. Zhu, W. Ma, X. Tang, Y. Liu and P. Huo, *Catal. Sci. Technol.*, 2020, **10**, 788–800.
103 Y. J. Yuan, P. Wang, Z. Li, Y. Wu, W. Bai, Y. Su, J. Guan, S. Wu, J. Zhong, Z. T. Yu and Z. Zou, *Appl. Catal., B*, 2019, **242**, 1–8.
104 S. Nayak, G. Swain and K. Parida, *ACS Appl. Mater. Interfaces*, 2019, **11**, 20923–20942.
105 C. Chen, X. Xie, B. Anasori, A. Sarycheva, T. Makaryan, M. Zhao, P. Urbankowski, L. Miao, J. Jiang and Y. Gogotsi, *Angew. Chem., Int. Ed.*, 2018, **57**, 1846–1850.
106 A. Wu, Y. Gu, Y. Xie, C. Tian, H. Yan, D. Wang, X. Zhang, Z. Cai and H. Fu, *ACS Appl. Mater. Interfaces*, 2019, **11**, 25986–25995.
107 S. Zhang, H. Yang, H. Gao, R. Cao, J. Huang and X. Xu, *ACS Appl. Mater. Interfaces*, 2017, **9**, 23635–23646.
108 B. Zhang, H. Shi, X. Hu, Y. Wang, E. Liu and J. Fan, *J. Phys. D: Appl. Phys.*, 2020, **53**, 205101.
109 W. Fu, H. He, Z. Zhang, C. Wu, X. Wang, H. Wang, Q. Zeng, L. Sun, X. Wang, J. Zhou, Q. Fu, P. Yu, Z. Shen, C. Jin, B. I. Yakobson and Z. Liu, *Nano Energy*, 2016, **27**, 44–50.
110 G. Dong, P. Qiu, F. Meng, Y. Wang, B. He, Y. Yu, X. Liu and Z. Li, *Chem. Eng. J.*, 2020, **384**, 123330.
111 S. H. Yu, Z. Tang, Y. Shao, H. Dai, H. Y. Wang, J. Yan, H. Pan and D. H. C. Chua, *ACS Appl. Energy Mater.*, 2019, **2**, 5799–5808.
112 J. M. Woods, Y. Jung, Y. Xie, W. Liu, Y. Liu, H. Wang and J. J. Cha, *ACS Nano*, 2016, **10**, 2004–2009.
113 S. Subudhi, G. Swain, S. P. Tripathy and K. Parida, *Inorg. Chem.*, 2020, **59**, 9824–9837.
114 S. Acharya, G. Swain and K. M. Parida, *Int. J. Hydrogen Energy*, 2020, **45**, 11502–11511.
115 G. Swain, S. Sultana and K. Parida, *Inorg. Chem.*, 2019, **58**, 9941–9955.
116 S. Jayabal, G. Saranya, J. Wu, Y. Liu, D. Geng and X. Meng, *J. Mater. Chem. A*, 2017, **5**, 24540–24563.
117 L. Zhang, X. Ji, X. Ren, Y. Ma, X. Shi, Z. Tian, A. M. Asiri, L. Chen, B. Tang and X. Sun, *Adv. Mater.*, 2018, **30**, 2–7.
118 H. Liu, Y. Zhu, J. Ma, Z. Zhang and W. Hu, *Adv. Funct. Mater.*, 2020, **30**, 1–21.
119 J. Xiong, J. Di, J. Xia, W. Zhu and H. Li, *Adv. Funct. Mater.*, 2018, **28**, 1801983.
120 J. Xiong, J. Di and H. Li, *J. Mater. Chem. A*, 2020, **8**, 12928–12950.
121 E. D. Koutsouroubi, I. Vamvasakis, I. T. Papadas, C. Drivas, S. A. Choulis, S. Kennou and G. S. Armatas, *ChemPlusChem*, 2020, **85**, 1379–1388.
122 D. P. Sahoo, S. Patnaik and K. Parida, *ACS Omega*, 2019, **4**, 14721–14741.
123 A. Behera, D. Kandi, S. Sahoo and K. Parida, *J. Phys. Chem. C*, 2019, **123**, 17112–17126.
124 S. Subudhi, S. Mansingh, G. Swain, A. Behera, D. Rath and K. Parida, *Inorg. Chem.*, 2019, **58**, 4921–4934.
125 L. Paramanik, K. H. Reddy, S. Sultana and K. Parida, *Inorg. Chem.*, 2018, **57**, 15133–15148.
126 S. Nayak, A. C. Pradhan and K. M. Parida, *Inorg. Chem.*, 2018, **57**, 8646–8661.
127 Q. Zhu, Y. Qu, D. Liu, K. W. Ng and H. Pan, *ACS Appl. Nano Mater.*, 2020, **3**, 6270–6296.
128 S. J. Rowley-Neale, D. A. C. Brownson, G. C. Smith, D. A. G. Sawtell, P. J. Kelly and C. E. Banks, *Nanoscale*, 2015, **7**, 18152–18168.
129 C. Tsai, F. A. Pedersen and J. K. Nørskov, *Nano Lett.*, 2014, **14**, 1381–1387.
130 R. Peng, L. Liang, Z. D. Hood, A. Boulesbaa, A. Puretzky, A. V. Ievlev, J. Come, O. S. Ovchinnikova, H. Wang, C. Ma, M. Chi, B. G. Sumpter and Z. Wu, *ACS Catal.*, 2016, **6**, 6723–6729.
131 T. F. Jaramillo, K. P. Jørgensen, J. Bonde, J. H. Nielsen, S. Horch and I. Chorkendorff, *Science*, 2007, **317**, 100–102.
132 B. Hinnemann, P. G. Moses, J. Bonde, K. P. Jørgensen, J. H. Nielsen, S. Horch, I. Chorkendorff and J. K. Nørskov, *J. Am. Chem. Soc.*, 2005, **127**, 5308–5309.
133 X. Kong, X. Shen, C. Zhang, S. N. Oliaee and Z. Peng, *Inorg. Chem. Front.*, 2016, **3**, 1376–1380.
134 J. Xie, H. Qu, J. Xin, X. Zhang, G. Cui, X. Zhang, J. Bao, B. Tang and Y. Xie, *Nano Res.*, 2017, **10**, 1178–1188.
135 D. Zhu, J. Liu, Y. Zhao, Y. Zheng and S. Z. Qiao, *Small*, 2019, **15**, 1–8.
136 T. Liang, Y. Liu, Y. Cheng, F. Ma and Z. Dai, *ChemCatChem*, 2020, **12**, 2840–2848.
137 U. Gupta and C. N. R. Rao, *Nano Energy*, 2017, **41**, 49–65.
138 J. Wan, R. Wang, L. Liu, J. Fan, E. Liu, X. Gao and F. Fu, *Int. J. Hydrogen Energy*, 2019, **44**, 16639–16647.
139 H. Wang, S. Li, Q. Wan, X. Su, T. Song, X. Wang and J. Wang, *J. Colloid Interface Sci.*, 2020, **577**, 38–47.
140 Y. J. Yuan, Z. J. Ye, H. W. Lu, B. Hu, Y. H. Li, D. Q. Chen, J. S. Zhong, Z. T. Yu and Z. G. Zou, *ACS Catal.*, 2016, **6**, 532–541.
141 Y. J. Yuan, Z. Li, S. Wu, D. Chen, L. X. Yang, D. Cao, W. G. Tu, Z. T. Yu and Z. G. Zou, *Chem. Eng. J.*, 2018, **350**, 335–343.

142 Y. J. Yuan, Z. Shen, S. Wu, Y. Su, L. Pei, Z. Ji, M. Ding, W. Bai, Y. Chen, Z. T. Yu and Z. Zou, *Appl. Catal., B*, 2019, **246**, 120–128.
143 Y. J. Yuan, Y. Yang, Z. Li, D. Chen, S. Wu, G. Fang, W. Bai, M. Ding, L. X. Yang, D. P. Cao, Z. T. Yu and Z. G. Zou, *ACS Appl. Energy Mater.*, 2018, **1**, 1400–1407.
144 B. Chai, M. Xu, J. Yan and Z. Ren, *Appl. Surf. Sci.*, 2018, **430**, 523–530.
145 L. M. Azofra, N. Li, D. R. Macfarlane and C. Sun, *Energy Environ. Sci.*, 2016, **9**, 2545–2549.
146 X. Cui, C. Tang and Q. Zhang, *Adv. Energy Mater.*, 2018, **8**, 1–25.
147 A. Chen and B. Y. Xia, *J. Mater. Chem. A*, 2019, **7**, 23416–23431.
148 Q. Liu, X. Zhang, B. Zhang, Y. Luo, G. Cui, F. Xie and X. Sun, *Nanoscale*, 2018, **10**, 14386–14389.
149 H. Li, C. Mao, H. Shang, Z. Yang, Z. Ai and L. Zhang, *Nanoscale*, 2018, **10**, 15429–15435.
150 S. Mansingh, S. Sultana, R. Acharya, M. K. Ghosh and K. M. Parida, *Inorg. Chem.*, 2020, **59**, 6646–6646.
151 S. Mansingh, K. K. Das, A. Behera, S. Subudhi, S. Sultana and K. Parida, *Nanoscale Adv.*, 2020, **2**, 2004–2017.
152 S. Sultana, S. Mansingh and K. M. Parida, *J. Mater. Chem. A*, 2019, **7**, 9145–9153.
153 C. Yang, Y. Zhu, J. Liu, Y. Qin, H. Wang, H. Liu, Y. Chen, Z. Zhang and W. Hu, *Nano Energy*, 2020, **77**, 105126.
154 M. Kim, B. C. Yeo, Y. Park, H. M. Lee, S. S. Han and D. Kim, *Chem. Mater.*, 2019, **32**, 709–720.
155 C. Guo, J. Ran, A. Vasileff and S. Z. Qiao, *Energy Environ. Sci.*, 2018, **11**, 45–56.
156 R. Manjunatha, A. Karajić, M. Liu, Z. Zhai, L. Dong, W. Yan, D. P. Wilkinson and J. Zhang, *Electrochem. Energy Rev.*, 2020, **3**, 506–540.
157 B. H. R. Suryanto, D. Wang, L. M. Azofra, M. Harb, L. Cavallo, R. Jalili, D. R. G. Mitchell, M. Chatti and D. R. MacFarlane, *ACS Energy Lett.*, 2019, **4**, 430–435.
158 Y. Liu, M. Han, Q. Xiong, S. Zhang, C. Zhao, W. Gong, G. Wang, H. Zhang and H. Zhao, *Adv. Energy Mater.*, 2019, **9**, 1–9.
159 K. Chu, Y. P. Liu, Y. B. Li, Y. L. Guo and Y. Tian, *ACS Appl. Mater. Interfaces*, 2020, **12**, 7081–7090.
160 X. Li, X. Ren, X. Liu, J. Zhao, X. Sun, Y. Zhang, X. Kuang, T. Yan, Q. Wei and D. Wu, *J. Mater. Chem. A*, 2019, **7**, 2524–2528.
161 H. Hirakawa, M. Hashimoto, Y. Shiraishi and T. Hirai, *J. Am. Chem. Soc.*, 2017, **139**, 10929–10936.
162 A. Shi, H. Li, S. Yin, Z. Hou, J. Rong, J. Zhang and Y. Wang, *Appl. Catal., B*, 2018, **235**, 197–206.
163 Y. Hao, X. Dong, S. Zhai, H. Ma, X. Wang and X. Zhang, *Chem. – Eur. J.*, 2016, **22**, 18722–18728.
164 K. Li, X. An, K. H. Park, M. Khraisheh and J. Tang, *Catal. Today*, 2014, **224**, 3–12.
165 S. Das, J. Pérez-Ramírez, J. Gong, N. Dewangan, K. Hidajat, B. C. Gates and S. Kawi, *Chem. Soc. Rev.*, 2020, **49**, 2937–3004.
166 E. V. Kondratenko, G. Mul, J. Baltrusaitis, G. O. Larrazábal and J. Pérez-Ramírez, *Energy Environ. Sci.*, 2013, **6**, 3112–3135.
167 A. U. Pawar, C. W. Kim, M. T. Nguyen-Le and Y. S. Kang, *ACS Sustainable Chem. Eng.*, 2019, **7**, 7431–7455.
168 K. Chan, C. Tsai, H. A. Hansen and J. K. Nørskov, *ChemCatChem*, 2014, **6**, 1899–1905.
169 Y. Xie, X. Li, Y. Wang, B. Li, L. Yang, N. Zhao, M. Liu, X. Wang, Y. Yu and J. M. Liu, *Appl. Surf. Sci.*, 2020, **499**, 143964.
170 W. Tu, Y. Li, L. Kuai, Y. Zhou, Q. Xu, H. Li, X. Wang, M. Xiao and Z. Zou, *Nanoscale*, 2017, **9**, 9065–9070.
171 X. Ma, Z. Li, L. E. K. Achenie and H. Xin, *J. Phys. Chem. Lett.*, 2015, **6**, 3528–3533.
172 A. Chen, X. Zhang, L. Chen, S. Yao and Z. Zhou, *J. Phys. Chem. C*, 2020, **124**, 22471–22478.
173 R. A. Geioushy, S. M. El-Sheikh, I. M. Hegazy, A. Shawky, S. El-Sherbiny and A. H. T. Kandil, *Mater. Res. Bull.*, 2019, **118**, 110499.
174 S. Yin, J. Li, L. Sun, X. Li, D. Shen, X. Song, P. Huo, H. Wang and Y. Yan, *Inorg. Chem.*, 2019, **58**, 15590–15601.
175 S. Garg, M. Li, A. Z. Weber, L. Ge, L. Li, V. Rudolph, G. Wang and T. E. Rufford, *J. Mater. Chem. A*, 2020, **8**, 1511–1544.
176 C. Yang, S. Li, Z. Zhang, H. Wang, H. Liu, F. Jiao, Z. Guo, X. Zhang and W. Hu, *Small*, 2020, **16**, 2001847.
177 M. Asadi, B. Kumar, A. Behranginia, B. A. Rosen, A. Baskin, N. Repnin, D. Pisasale, P. Phillips, W. Zhu, R. Haasch, R. F. Klie, P. Král, J. Abiade and A. Salehi-Khojin, *Nat. Commun.*, 2014, **5**, 1–8.
178 K. Lv, C. Teng, M. Shi, Y. Yuan, Y. Zhu, J. Wang, Z. Kong, X. Lu and Y. Zhu, *Adv. Funct. Mater.*, 2018, **28**, 1–10.
179 S. A. Francis, J. M. Velazquez, I. M. Ferrer, D. A. Torelli, D. Guevarra, M. T. McDowell, K. Sun, X. Zhou, F. H. Saadi, J. John, M. H. Richter, F. P. Hyler, K. M. Papadantonakis, B. S. Brunschwig and N. S. Lewis, *Chem. Mater.*, 2018, **30**, 4902–4908.
180 F. Li, S. F. Zhao, L. Chen, A. Khan, D. R. MacFarlane and J. Zhang, *Energy Environ. Sci.*, 2016, **9**, 216–223.
181 Y. Wang, Z. Zhang, L. Zhang, Z. Luo, J. Shen, H. Lin, J. Long, J. C. S. Wu, X. Fu, X. Wang and C. Li, *J. Am. Chem. Soc.*, 2018, **140**, 14595–14598.
182 C. Qiu, S. Bai, W. Cao, L. Tan, J. Liu, Y. Zhao and Y. F. Song, *Trans. Tianjin Univ.*, 2020, **26**, 352–361.
183 N. Kumar, S. S. Ray, S. Kumar, R. Gusain, N. Manyala and S. Eslava, *ACS Appl. Energy Mater.*, 2020, **3**, 9897–9909.
184 F. Xu, B. Zhu, B. Cheng, J. Yu and J. Xu, *Adv. Opt. Mater.*, 2018, **6**, 1800911.
185 Y. Wang, Z. Zhang, L. Zhang, Z. Luo, J. Shen, H. Lin, J. Long, J. C. S. Wu, X. Fu, X. Wang and C. Li, *J. Am. Chem. Soc.*, 2018, **140**, 14595–14598.
186 P. Y. Jia, R. T. Guo, W. G. Pan, C. Y. Huang, J. Y. Tang, X. Y. Liu, H. Qin and Q. Y. Xu, *Colloids Surf., A*, 2019, **570**, 306–316.
187 V. Yadav, S. Roy, P. Singh, Z. Khan and A. Jaiswal, *Small*, 2019, **15**, 1803706.

188 J. H. Hwang, M. A. Islam, H. Choi, T. J. Ko, K. L. Rodriguez, H. S. Chung, Y. Jung and W. H. Lee, *Anal. Chem.*, 2019, **91**, 11770–11777.
189 D. Vikraman, S. A. Patil, S. Hussain, N. Mengal, H. S. Kim, S. H. Jeong, J. Jung, H. S. Kim and H. J. Park, *Dyes Pigm.*, 2018, **151**, 7–14.
190 Y. Liu, S. Zhang, J. He, Z. M. Wang and Z. Liu, *Nano-Micro Lett.*, 2019, **11**, 1–24.
191 D. Lembke, S. Bertolazzi and A. Kis, *Acc. Chem. Res.*, 2015, **48**, 100–110.
192 Y. P. Venkata Subbaiah, K. J. Saji and A. Tiwari, *Adv. Funct. Mater.*, 2016, **26**, 2046–2069.
193 B. Radisavljevic, A. Radenovic, J. Brivio, V. Giacometti and A. Kis, *Nat. Nanotechnol.*, 2011, **6**, 147–150.
194 E. Singh, P. Singh, K. S. Kim, G. Y. Yeom and H. S. Nalwa, *ACS Appl. Mater. Interfaces*, 2019, **11**, 11061–11105.
195 T. Nawz, A. Safdar, M. Hussain, D. S. Lee and M. Siyar, *Crystals*, 2020, **10**, 902.
196 N. Joseph, P. M. Shafi and A. C. Bose, *Energy Fuels*, 2020, **34**, 6558–6597.
197 E. Pomerantseva and Y. Gogotsi, *Nat. Energy*, 2017, **2**, 1–6.
198 B. Wang, Q. Wu, H. Sun, J. Zhang, J. Ren, Y. Luo, M. Wang and H. Peng, *J. Mater. Chem. A*, 2017, **5**, 925–930.
199 B. Kirubasankar, M. Narayanasamy, J. Yang, M. Han, W. Zhu, Y. Su, S. Angaiah and C. Yan, *Appl. Surf. Sci.*, 2020, **534**, 147644.
200 M. W. Kadi, R. M. Mohamed and A. A. Ismail, *J. Nanopart. Res.*, 2020, **22**, 156.
201 J. Zhang, C. Xing and F. Shi, *Int. J. Hydrogen Energy*, 2020, **45**, 6291–6301.
202 D. Jiang, B. Wen, Y. Zhang, Y. Jin, D. Li and M. Chen, *J. Colloid Interface Sci.*, 2019, **536**, 1–8.
203 X. Xu, Z. Si, L. Liu, Z. Wang, Z. Chen, R. Ran, Y. He and D. Weng, *Appl. Surf. Sci.*, 2018, **435**, 1296–1306.
204 Y. Li, Z. Yin, G. Ji, Z. Liang, Y. Xue, Y. Guo, J. Tian, X. Wang and H. Cui, *Appl. Catal., B*, 2019, **246**, 12–20.
205 Y. Chen, F. Su, H. Xie, R. Wang, C. Ding, J. Huang, Y. Xu and L. Ye, *Chem. Eng. J.*, 2021, **404**, 126498.
206 J. Xu, X. Yan, Y. Qi, Y. Fu, C. Wang and L. Wang, *Chem. Eng. J.*, 2019, **375**, 122053.
207 J. Tao, X. Yu, Q. Liu, G. Liu and H. Tang, *J. Colloid Interface Sci.*, 2021, **585**, 470–479.
208 C. M. Nagaraja, M. Kaur and S. Dhingra, *Int. J. Hydrogen Energy*, 2020, **45**, 8497–8506.
209 J. Deng, H. Li, J. Xiao, Y. Tu, D. Deng, H. Yang, H. Tian, J. Li, P. Ren and X. Bao, *Energy Environ. Sci.*, 2015, **8**, 1594–1601.
210 G. B. De-Mello, L. Smith, S. J. Rowley-Neale, J. Gruber, S. J. Hutton and C. E. Banks, *RSC Adv.*, 2017, **7**, 36208–36213.
211 H. Huang, J. Song, D. Yu, Y. Hao, Y. Wang and S. Peng, *Appl. Surf. Sci.*, 2020, **525**, 146623.
212 H. Yu, Y. Xue, L. Hui, C. Zhang, Y. Zhao, Z. Li and Y. Li, *Adv. Funct. Mater.*, 2018, **28**, 1707564.
213 A. M. Abraham, G. Bharath, A. Hai and F. Banat, *J. Phys. D: Appl. Phys.*, 2019, **53**, 065501.
214 J. Lv, M. Yang, T. Liang, S. Ken and M. Hideo, *Chem. Phys. Lett.*, 2017, **678**, 212–215.
215 X. Zhang, M. Zhang, Y. Tian, J. You, C. Yang, J. Su, Y. Li, Y. Gao and H. Gu, *RSC Adv.*, 2018, **8**, 10698–10705.
216 B. Liu, J. Qin, H. Yang, X. Hu, W. Zhao and Z. Zhang, *ChemCatChem*, 2020, **12**, 5221–5228.
217 H. Qin, R. T. Guo, X. Y. Liu, W. G. Pan, Z. Y. Wang, X. Shi, J. Y. Tang and C. Y. Huang, *Dalton Trans.*, 2018, **47**, 15155–15163.